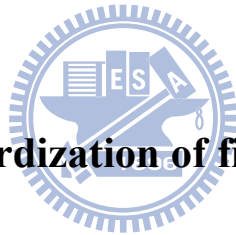


國立交通大學

土木工程學系

博士論文

多頻道表面波震測之施測與頻散分析標準化研究



**Towards the standardization of field testing and dispersion  
analysis of MASW method**

研究生：張宗盛

指導教授：林志平 教授

中華民國九十八年七月

**Towards the standardization of field testing and dispersion  
analysis of MASW method**

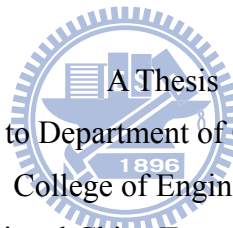
研究生：張宗盛

Student : Tzong-Sheng Chang

指導教授：林志平

Advisor : Chih-Ping Lin

國立交通大學  
土木工程學系  
博士論文



Submitted to Department of Civil Engineering  
College of Engineering

National Chiao Tung University

in partial Fulfillment of the Requirements

for the Degree of

Doctor of Philosophy

in

Civil Engineering

July 2009

HsinChu, Taiwan, Republic of China

中華民國九十八年七月

# 多頻道表面波震測之施測與頻散分析標準化研究

學生：張宗盛

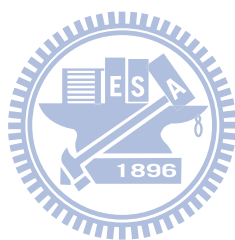
指導教授：林志平博士

國立交通大學土木工程學系

## 中文摘要

由於非破壞性的試驗方法及簡便操作等特性，將表面波震測運用於工址調查實務上愈來愈受歡迎。特別是多頻道表面波震測（Multi-station Analysis of Surface Wave, MASW）紀錄針對單一測線可提供較深探測深度及較多資料。但如欲得到品質良好且寬頻的頻散曲線，試驗施作時之施測參數即扮演一重要角色。選用施測參數時常因訊號分析、施測解析度及深度上的不同考量而陷入兩難。除此之外，MASW 試驗者亦常對前人提出之數種頻散分析演算法進行驗證比較。本文最主要的課題即為針對 MASW 中野外施測及頻散分析兩部分提出一標準步驟。針對野外施測，本文先行討論時間及空間施測參數對實驗的影響，包含時間與空間域上的映頻與資料遺漏、波場的遠近場效應、高次震態模組的影響及空間水平解析度等。之後針對各種影響加以探討分析並提出一創新施測方式及合成震測資料方法，藉以消彌各施測參數選用規則上的衝突並使 MASW 施測步驟標準化而有利一般工地實務應用。在頻散分析方面，本文提出一波場轉換之統一演算法。先將野外收錄之時間-空間域之二維波場轉換至頻率-空間域，並以線性迴歸之多頻道表面波頻譜分析（Multi-channel Spectral Analysis of Surface Wave, MSASW）進行初步頻散分析。透過頻率-空間域之複數頻譜及線性迴歸資料評估收錄訊號品質並消除不良訊號。再將頻率-空間域之複數頻譜以統一波場轉換方式同時得到頻率-波數

(wavenumber) 域、頻率-慢度 (slowness) 域、頻率-速度 (velocity) 域及頻率-波長 (wavelength) 域之頻散曲線。本文並提出一藉由使用離散空間傅立葉轉換 (discrete-space Fourier Transform) 之最佳化方法證明各域之頻散曲線皆為相同，並討論頻散曲線取樣時以等頻率及等波長進行之優劣。本文的各項結果可作為日後多頻道表面波震測實驗標準化之基礎。



# **Towards the standardization of field testing and dispersion analysis for MASW methods**

**Student : Tzong-Sheng Chang**

**Advisors : Dr. Chih-Ping Lin**

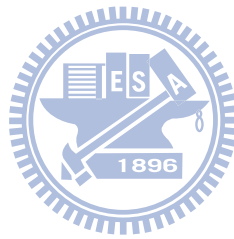
**Department of Civil Engineering**

**National Chiao Tung University**

## **ABSTRACT**

The surface wave method has gained popularity in engineering practice for determining S-wave velocity depth profiles. In particular, MASW (multi-station analysis of surface wave) method permits a single survey of a broad depth range and high levels of redundancy with a single field configuration. Despite its apparent advantage over the two-channel SASW (spectral analysis of surface wave) method, the testing configuration of the MASW method remains a crucial factor that may affect the test results. Tradeoffs are involved when selecting the testing parameters. In addition, several algorithms with different preferences in the literature exist for the dispersion analysis. The objectives of this study are to establish a standard procedure for field testing and dispersion analysis of MASW. In the field testing, the influences of temporal and spatial parameters were investigated, including aliasing and leakage in both time and space domain, far and near field effects, effect of higher modes, and horizontal resolution. The investigation leads to several rules for choosing testing parameters. An innovative testing procedure and the associated signal processing was proposed to resolve the dilemma of choosing testing parameters and standardize the testing procedure. In the dispersion analysis, a unified approach was proposed. The wavefield in time-space ( $t-x$ )

domain is transformed to frequency-space ( $f-x$ ) domain first, in which a preliminary dispersion analysis (a new method called multi-channel spectral analysis of surface wave, MSASW) was introduced and methods for assessing data quality and data screening were proposed. The  $f-x$  domain is further transformed to  $f-k$  (wavenumber),  $f-p$  (slowness),  $f-v$  (velocity), or  $f-\lambda$  (wavelength). The dispersion curves obtained by different transformation are shown to be identical by a newly-proposed optimization method based on the discrete-space Fourier Transform, which allows the transformed domain remain continuous for best resolution of dispersion analysis. A wavelength-controlled sampling approach was further proposed for the dispersion curve to avoid bias in depth sampling. The results of this study may lead to further standardization of the surface wave testing.



## 誌 謝

如果不是指導老師林志平博士的引見、啟發及教導，我絕對無法來到交大開始我的博士研究及完成本文。之於本文，林老師除了提供許多原創性的研究方向外，更在研究邏輯及方法上不斷給我指引。如果說，本文對相關課題有一點點的貢獻，那我只是站在林老師的肩膀上發現了這些結果。在此，我必須對他致上最高的謝意及敬意。

另外，在交大求學期間，我很榮幸地接受了許多老師指導。特別是潘以文教授及廖志中教授亦師亦友的教誨，除了給我開闊眼界的知識外，也端正了我的人生觀，在此致上由衷謝意。

論文口試期間，承蒙莊長賢教授、倪勝火教授、張文忠教授、余騰鐸教授、董家鈞教授、潘以文教授及廖志中教授撥空蒞臨指導並給予寶貴意見，使我獲益良多，在此亦致上敬意。

翔益營造的龔書潭及黃金煌兩位先生在這幾年給我極大的空間及時間，並讓我在經濟上無後顧之憂，無以回報的我僅能致上感謝。另外，來到交大後，許多學長姐及學弟妹都慷慨地提供協助。年近中年，還能交到許多真心相待的朋友，我想這是一個比學位更重要的收穫。

我的家人給我的支持與鼓勵一直是最有力的後盾。在交大的八年，我經歷了人生中許多重大的起伏轉折。工作的忙碌奔波、研究的無力枯燥與生活的煩瑣枝節交互壓迫下，常常讓我想要放棄研讀。然而，家人們、老師們、長官們及同學朋友們，你們持續從不間斷的鼓勵讓我能完整地畫下句點，而不以逃避作為收場。我想，這個過程賦予我人生的淬鍊、改變及意義遠遠大於博士學位所能帶來的小小虛榮。

謝謝你們!

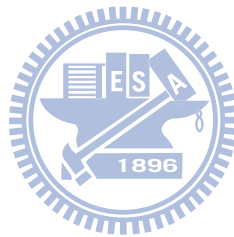
# Contents

|  |          |
|--|----------|
| 中文摘要.....  | I        |
| ABSTRACT .....   | III      |
| 誌 謝.....   | V        |
| Contents.....  | VI       |
| List of figures .....                                      | IX       |
| List of tables .....                                       | XII      |
| <b>1 Introduction .....</b>                                | <b>1</b> |
| 1.1 Motivation.....  | 1        |
| 1.2 Objectives .....                                       | 3        |
| 1.3 Dissertation outline .....                             | 4        |
| <b>2 Literature review .....</b>                           | <b>6</b> |
| 2.1 Dynamic properties of soil and testing methods.....    | 6        |
| 2.1.1 Dynamic properties of soil .....                     | 6        |
| 2.1.2 Testing methods .....                                | 10       |
| 2.2 Wave propagation and computation of surface wave ..... | 15       |
| 2.2.1 Basic theory of elastic wave propagation.....        | 16       |
| 2.2.2 Computation of theoretical dispersion curve.....     | 29       |
| 2.2.3 Computation of synthetic wavefield .....             | 33       |
| 2.3 Seismic tests using surface wave .....                 | 36       |
| 2.3.1 Overview of surface wave methods .....               | 36       |
| 2.3.2 Field testing procedure of MASW .....                | 43       |
| 2.3.3 Dispersion analysis of MASW.....                     | 44       |
| 2.3.4 Inversion for the stiffness profile .....            | 50       |



|          |   |           |
|----------|---|-----------|
| <b>3</b> | <b>Investigation of field parameters and standardization of field testing .....</b>         | <b>53</b> |
| 3.1      | <i>Temporal parameters of field testing .....</i>   | 54        |
| 3.1.1    | Aliasing due to time domain discretization: the sampling interval, $\Delta t$ .....         | 54        |
| 3.1.2    | Leakage due to time domain truncation: total sampling duration, $T$ .....                   | 54        |
| 3.2      | <i>Spatial parameters of field testing .....</i>  | 55        |
| 3.2.1    | Aliasing due to space domain discretization: the geophone spacing, $\Delta x$ .....         | 55        |
| 3.2.2    | Leakage due to space domain truncation and modal separation: the geophone spread, $L$ ..... | 57        |
| 3.2.3    | Near and far field effects: the minimum offset, $X_0$ and maximum offset, $(X_0+L)$ .....   | 60        |
| 3.2.4    | The dilemma .....   | 62        |
| 3.3      | <i>The countermeasure: Pseudo-section approach .....</i>                                    | 64        |
| 3.3.1    | The concept of Pseudo-section method.....   | 64        |
| 3.3.2    | Combining seismic records of the pseudo-section method .....                                | 66        |
| 3.3.3    | Observation on near and far field effects via pseudo-section method.....                    | 72        |
| 3.4      | <i>Seismic sources and receivers.....</i>   | 74        |
| 3.4.1    | Some improvement on the seismic source.....   | 74        |
| 3.4.2    | Some improvement on the receivers .....   | 82        |
| 3.5      | <i>The proposed standard field testing.....</i>   | 89        |
| <b>4</b> | <b>Unified dispersion analysis .....</b>  | <b>91</b> |
| 4.1      | <i>Analyses in the frequency-space (<math>f</math>-<math>x</math>) domain .....</i>         | 93        |
| 4.1.1    | Representation of surface waves in $f$ - $x$ domain.....                                    | 93        |
| 4.1.2    | Real part and energy spectrum of the $f$ - $x$ complex data .....                           | 95        |
| 4.1.3    | Phase Angles: Multi-station spectral analysis of surface wave (MSASW).....                  | 95        |
| 4.1.4    | Amendment for near and far field effect: Optimum offset range selection.....                | 101       |
| 4.2      | <i>Unified Wavefield Transformation (UWFT).....</i>   | 109       |
| 4.2.1    | Different transformations and presentations of space domain .....                           | 109       |
| 4.2.2    | Characteristics of wavefield transformation in different domains .....                      | 111       |
| 4.2.3    | Optimization of dispersion analysis .....   | 124       |
| 4.3      | <i>Data sampling of dispersion curve.....</i>   | 129       |

|          |  |            |
|----------|--|------------|
| 4.4      | <i>The proposed standard dispersion analysis</i> ..... | 132        |
| <b>5</b> | <b>Conclusion and suggestion</b> .....                 | <b>134</b> |
| 5.1      | <i>Conclusion</i> .....                                | 134        |
| 5.2      | <i>Suggestion</i> .....                                | 138        |
| <b>6</b> | <b>Reference</b> .....                                 | <b>139</b> |



## List of figures

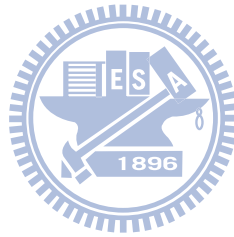
|  |    |
|--|----|
| Fig. 2-1 Cause-effect relationships in soil response to dynamic excitations.....   | 6  |
| Fig. 2-2 Dependence of threshold shear strains from plasticity index.....  | 8  |
| Fig. 2-3 Ranges of variability of cyclic shear strain amplitude in laboratory and in-situ tests.....   | 10 |
| Fig. 2-4 Stress notation of an element in an x-y-z Cartesian coordination .....  | 16 |
| Fig. 2-5 The ratio of Rayleigh wave velocity, $v_R$ , verse body wave velocities as a function of Poisson ratio, $\nu$<br>.....  | 25 |
| Fig. 2-6 Rayleigh wave particle motion in a homogeneous, isotropic half space; retrograde at the surface,<br>passing through purely vertical at about $\lambda/5$ then becoming prograde at depth..... | 25 |
| Fig. 2-7 Particle motions of Rayleigh wave over one wavelength along the surface and as a function of depth<br>.....   | 26 |
| Fig. 2-8 The model of a vertically heterogeneous halfspace .....   | 26 |
| Fig. 2-9 Rayleigh waves dispersion curves in vertically heterogeneous media.....   | 30 |
| Fig. 2-10 Rayleigh displacement eigenfunctions in vertically heterogeneous media.....  | 30 |
| Fig. 2-11 Typical dispersion curves of different type of strata.....   | 32 |
| Fig. 2-12 Steady State Rayleigh Wave (SSRW) method: field procedure .....  | 37 |
| Fig. 2-13 Simplified inversion process proposed for the SSRM.....  | 37 |
| Fig. 2-14 SASW method field configuration.....   | 38 |
| Fig. 2-15 Common receiver midpoint array with source position reversing .....  | 39 |
| Fig. 2-16 Common source array .....  | 39 |
| Fig. 2-17 SASW signal processing- $\Delta\phi$ vs Frequency .....  | 40 |
| Fig. 2-18 Scheme of MASW .....   | 42 |
| Fig. 2-19 Field test configuration of MASW .....   | 44 |
| Fig. 2-20 An example of $f-k$ transformation .....   | 46 |
| Fig. 2-21 Exemplification of the Slant-Stack transform concept.....  | 47 |
| Fig. 2-22 An example of $p-f$ transformation .....   | 47 |
| Fig. 2-23 An example of Phase shift method.....  | 49 |
| Fig. 2-24 Ratio $a$ that was used during construction of the initial $v_s$ profiles .....  | 51 |
| Fig. 3-1 Two different signal fitting the same set of samples.....   | 54 |

|  |     |
|--|-----|
| Fig. 3-2 An illustration of phase un-wrapping in the space domain for the multi-station spectral analysis of surface wave.....   | 55  |
| Fig. 3-3 The geophone spacing $\Delta x$ influence on aliasing problem .....   | 56  |
| Fig. 3-4 The geophone spread $L$ affects the modal separation.....   | 57  |
| Fig. 3-5 An example wavefield of a multi-mode surface wave .....   | 59  |
| Fig. 3-6 Effects of multiple modes on the phase angle as a function of the source-to-receiver offset. ....   | 59  |
| Fig. 3-7 Illustration of Pseudo-section method.....  | 64  |
| Fig. 3-8 Static errors in $\varphi-x$ domain .....   | 66  |
| Fig. 3-9 Scheme of signal process for correction of the static error when seaming seismic records for synthesis of pseudo-section .....  | 67  |
| Fig. 3-10 Dispersion curves from conventional and pseudo-section records analyzed by (a) Unified WaveField Transformation (UWFT) (b) Multi-channel Spectral Analysis of Surface Wave (MSASW) ..... | 70  |
| Fig. 3-11 Phase angle difference of conventional and pseudo-section records .....  | 71  |
| Fig. 3-12 Near and far field effects observed in $\varphi-x$ domain .....  | 73  |
| Fig. 3-13 Electrical operated seismic source ESS100SC.....   | 75  |
| Fig. 3-14 New developed weight-drop seismic source.....  | 76  |
| Fig. 3-15 The pseudo-section record by the source of the 12 lb sledgehammer (BH) .....   | 79  |
| Fig. 3-16 The pseudo-section record by the source of the spring accelerator (AF).....  | 80  |
| Fig. 3-17 The pseudo-section record by the source of the new developed weight-drop source (WD).....  | 81  |
| Fig. 3-18 The pedestals and receiver of the land streamer developed at NCTU.....   | 86  |
| Fig. 3-19 The land streamer developed at NCTU .....  | 86  |
| Fig. 3-20 The pseudo-section records collected by Land Streamer (left) and Spike Geophone Array (right) in $t-x$ , $f-x$ and $f-\nu$ domains (signals produced by the BH source) .....             | 87  |
| Fig. 3-21 The pseudo-section records collected by Land Streamer (left) and Spike Geophone Array (right) in $t-x$ , $f-x$ and $f-\nu$ domains (signals produced by the WD source) .....             | 88  |
| Fig. 3-22 (a) The proposed standard field testing configuration and (b) the corresponding pseudo-section. ....   | 89  |
| Fig. 4-1 The phase velocity and phase angle in $f-x$ domain .....  | 95  |
| Fig. 4-2 Results of the dispersion analysis of the short array (11.5 m) at the verification test site .....  | 100 |

|  |     |
|--|-----|
| Fig. 4-3 Results of the dispersion analysis of the short array (23 m) at the verification test site.....                       | 100 |
| Fig. 4-4 Near and far field effects in the real part of $f$ - $x$ complex data .....   | 104 |
| Fig. 4-5 Testing records in Bao-Shan second reservoir for “optimum offset range selection” .....                               | 105 |
| Fig. 4-6 The dispersion curves and $f$ - $\nu$ spectrum of tests in Bao-Shan second reservoir .....                            | 106 |
| Fig. 4-7 Testing records in Tai-Bao City for “optimum offset range selection” .....  | 107 |
| Fig. 4-8 The dispersion curves and $f$ - $\nu$ spectrum of tests in Tai-Bao City .....   | 108 |
| Fig. 4-9 The energy spectra of the wavefield of simple mode superposition ( $\Delta x = 1\text{m}, L=1024\text{m}$ ).....      | 116 |
| Fig. 4-10 The energy spectra of the wavefield of simple mode superposition ( $\Delta x = 16\text{m}, L=1024\text{m}$ ).....    | 116 |
| Fig. 4-11 The energy spectra of the wavefield of simple mode superposition ( $\Delta x = 1\text{m}, L=256\text{m}$ ).....      | 117 |
| Fig. 4-12 The energy spectra and dispersion curves (Normally dispersive case, $\Delta x = 1\text{m}, L=128\text{m}$ ) .....    | 118 |
| Fig. 4-13 The energy spectra and dispersion curves (Normally dispersive case, $\Delta x = 4\text{m}, L=128\text{m}$ ) .....    | 119 |
| Fig. 4-14 The energy spectra and dispersion curves (Normally dispersive case, $\Delta x = 1\text{m}, L=24\text{m}$ ) .....     | 120 |
| Fig. 4-15 The energy spectra and dispersion curves (Irregularly dispersive case (A), $\Delta x = 1\text{m}, L=128\text{m}$ ).. | 121 |
| Fig. 4-16 The energy spectra and dispersion curves (Irregularly dispersive case, $\Delta x = 4\text{m}, L=128\text{m}$ ) ..... | 122 |
| Fig. 4-17 The energy spectra and dispersion curves (Irregularly dispersive case, $\Delta x = 1\text{m}, L=24\text{m}$ ) .....  | 123 |
| Fig. 4-18 The $f$ - $k$ , $f$ - $\lambda$ , $f$ - $\nu$ , $f$ - $p$ spectrum and dispersion curves before Optima Picking ..... | 126 |
| Fig. 4-19 The dispersion curves in $\lambda$ - $\nu$ domain before and after Optima Picking .....                              | 126 |
| Fig. 4-20 The $f$ - $k$ , $f$ - $\lambda$ , $f$ - $\nu$ , $f$ - $p$ spectrum and dispersion curves after Optima Picking .....  | 127 |
| Fig. 4-21 Identical results from different transformations after optima picking in $\lambda$ - $\nu$ domain .....              | 127 |
| Fig. 4-22 Inherent limit on investigated wavelength of seismograms due to the length of survey line.....                       | 128 |
| Fig. 4-23 Dispersion curve by equal sampling in $f$ domain .....   | 129 |
| Fig. 4-24 Non equal-frequency sampling dispersion curves (2-layer model with $L=128\text{m}$ ) .....                           | 131 |
| Fig. 4-25 The flow chart of the proposed standard dispersion analysis .....  | 132 |

## List of tables

|   |     |
|---|-----|
| Table 2.1 Measurement of low-Strain dynamic properties of soils comparison between in-situ and laboratory techniques..... | 11  |
| Table 2.2 Laboratory tests for measuring dynamic properties of soil.....  | 12  |
| Table 2.3 Field tests for measuring dynamic properties of soil.....   | 14  |
| Table 3.1 Modes used to generate synthetic wavefields using modal superposition .....                                     | 56  |
| Table 4.1 Constants of the normally dispersive cases .....  | 113 |
| Table 4.2 Constants of the irregularly dispersive cases .....   | 114 |



# 1 Introduction

## 1.1 Motivation

The soil behavior under dynamic loading, especially the stiffness, is fundamental for most of geotechnical analyses. The shear-wave velocity profile of geomaterials in the shallow depth plays an important role in engineering applications including soil liquefaction assessment, earthquake site response, dynamic soil-structure interaction, appraisal of mechanical properties of geomaterials, etc. In 1997, the average S wave velocity of upper 30 meters of the strata,  $v_s^{30}$ , was accepted for the soil classification for the Uniform Building Code (UBC) of United States (Dobry et al, 2000). The near-surface S wave velocity of a construction site is also a fundamental parameter in the new provisions of Eurocode-8 (Sabetta et al, 2002).

For obtaining dynamic soil properties, both tests in laboratory and in-situ have their specific purposes and advantages. But concededly the less undisturbed states and wider volumes of testing geomaterials are the major two advantages of in-situ testing. The use of seismic methods to determine the underground stiffness is attractive since they are not affected by sample disturbance or insertion effects and are capable of sampling a representative volume of the ground even in difficult materials such as fractured rock or gravel deposit. One other main reasons why seismic tests are popular is the magnitude of strains. The soil parameters at very low strains can be acquired by conducting tests applying wave propagation.

In-situ seismic tests are categorized into two main kinds: invasive and non-invasive tests. Subsurface tests, such as cross-hole, down-hole, p-s logging and seismic cone methods, require bore holes or rod penetration that makes the tests expensive and time-consuming. At shallow depths, the surface tests, such as refraction and surface wave method, can determine

the stiffness-depth profile without the need of intrusive tasks. Among seismic waves, surface wave is most easily generated and contains the largest amplitude for in-situ measurements. Surface wave is primarily affected by the shear-wave velocity profile and does not have the theoretical limitations of seismic refraction method. Common in-situ non-invasive tests by using surface waves include Steady State Rayleigh Wave (SSRW), Spectral Analysis of Surface Waves (SASW) (Nazarian and Stoke, 1986; Nazarian et al, 1983; Nazarian and Stoke, 1985) and Multi-station Analysis of Surface Waves (MASW) (Gabriel et al, 1987; McMechan et al, 1981; Nolet et al, 1976; Park et al, 1999; Xia et al, 2002; Lin et al, 2002; Foti et al, 2002).

At the shallow depths, the stratum is generally a vertically heterogeneous medium. As a result, the phase velocity of surface wave propagating in the medium is a function of frequency, a phenomenon is called dispersion. The dispersion of the phase velocity of surface wave is governed by the mechanical properties of the layered medium. Once the phase velocity as a function of frequency is obtained, the mechanical properties of the medium can be inversely determined. Following this concept, Surface wave methods generally involve three major steps: (1) Generating artificial perturbations on tested sites and recording the seismograms via receivers (Geophones) and a seismograph. (2) Determination of the experimental dispersion curve by signal processing procedures from the collected field seismograms. (3) Determination of the stiffness profile from the experimental dispersion curve by an inversion algorithm.

Comparing with SSRW and SASW, MASW has advantages of field efficiency, automatic analysis, and data redundancy. Despite its advantages over conventional SSRW and SASW, the testing configuration remains a crucial factor that may affect the test results. To avoid errors and ambiguities caused by physical phenomena and digital signal processing, some constraints on survey line configurations diminish the convenience and feasibility of MASW.



Tradeoffs are involved when selecting the testing parameters. Especially for inexperienced testers, it could be a perplexity when conducting tests in the field. Furthermore, several algorithms with different preference in the literature exist for the dispersion analysis. A standard and preferred guideline is yet to be proposed for engineering practice.

## 1.2 Objectives

The wavefield recorded in-situ directly decides the quality of the result. The raw data is a time-space discretized wavefield and influenced by wave propagation phenomena and discrete recording. The dispersion curve analysis from the recorded data is affected by higher modes of wave propagation and discretization and truncation of wavefield. An inadequate testing configuration might cause deficient results for specific engineering problems. Although some rules are available for selecting the testing parameters, tradeoffs are involved and no clear guideline is available for conducting MASW tests.

Several algorithms were proposed to analyze the dispersion relations from the recorded wavefield. The analysis usually starts with a transformation from the original time-space ( $t$ - $x$ ) domain to the frequency-space ( $f$ - $x$ ) domain. The SASW uses only the information of phase angle versus offsets. It usually requires careful manual attention and is quite time-consuming due to the associated phase angle unwrapping (Lin et al, 2002). Other methods of dispersion analysis involve another sequential transformation. They transform the survey data in  $t$ - $x$  domain into frequency- wavenumber ( $f$ - $k$ ) (Capon, 1969; Yilmaz, 1987; Alleyne et al, 1990; Forchap et al, 1998; Lu et al, 2004), frequency- slowness ( $f$ - $p$ ) (McMechan et al, 1981) or frequency- velocity ( $f$ - $v$ ) (Park et al, 1998b) domains. Whether the dispersion relation in  $f$ - $k$ ,  $f$ - $p$  and  $f$ - $v$  spectra can be clearly and accurately identified depends not only on the complexity of strata and field configuration, but also on the discrete transformation algorithms. Several studies have made comparisons among aforementioned transformation algorithms, but

different algorithms were favored without consensus (Foti, 2000; Beaty, 2002; O'Neil, 2004; Mora, 2003; Xia et al, 2005).

Lack of standard guidelines for choosing the testing configuration and performing the dispersion analysis, the MASW method becomes ambiguous and the degree of success of MASW testing is uncertain. Incorrect results may occur, not from the inherent limitations of MASW, but due to negligence or mistakes from experimenters' lacks of expertise and experience. Therefore, this study is aimed to propose some operation principles or standard procedures for eliminating or mitigating those unnecessary errors and uncertainties. Besides ensuring the correctness, the proposed procedure is intended to optimize the investigation depth and resolution.

### 1.3 Dissertation outline

This study mainly focuses on field testing and dispersion analysis of MASW. It attempts to explicitly establish a set of standard procedures and logical thinking as guidelines for MASW experimenters. There are three major divisions of this dissertation. The motivation, objectives, and fundamental background of this study are introduced in the first part. The second part studies the effects on the field parameters and standardization of field testing. The last part is related to the unification of algorithms and techniques for enhancing the resolution and correctness of dispersion analysis.

The presentation of background in Chapter 2 includes several aspects. The dynamic properties of soil, laboratory and in-situ testing methods are first introduced. The basic theory of wave propagation and computation of dispersion curve and synthetic wavefield of surface wave will then follow. The last part gives an overall review on seismic tests using surface wave with emphasis on the field testing, dispersion analysis and inversion of MASW.

Chapter 3 investigates the influence of both temporal and spatial field parameters of

MASW. Although the corresponding rule for each temporal or spatial parameter can be made, the interworking of spatial parameters leads to conflict or dilemma. An innovative testing procedure and the associated signal processing is proposed to resolve the dilemma and standardize the testing procedure, which can also be used to optimize investigation depth and the lateral resolution. In addition, seismic sources for greater energy and lower frequency and sensors for better testing convenience are suggested and applied in this study.

Chapter 4 proposes a unified approach for dispersion analysis. The procedure starts with a method called multi-channel spectral analysis of surface wave (MSASW). It provides not only a preliminary dispersion analysis but also evaluation of data quality and optimum offset selection for removing the near and far field effects. The procedure is followed by the unified algorithm that transforms the time-space wavefield into  $f-k$ ,  $f-p$ ,  $f-\nu$  and  $f-\lambda$  domains simultaneously. The dispersion curves obtained by different transformation are shown to be equivalent by a newly-proposed optimization method for dispersion analysis. Further investigations on the data sampling of the dispersion curve are also discussed in this chapter.

Finally some conclusions and suggestions are summarized in Chapter 5. A set of operation principles or standard procedures of field testing and dispersion analysis of MASW is clearly proposed for experimenters. Future researches are also suggested in the end.

## 2 Literature review

### 2.1 Dynamic properties of soil and testing methods

#### 2.1.1 Dynamic properties of soil

Variables and factors affecting the dynamic behavior of a soil according to the previous can be broadly divided into two categories according to their origin: external variables and intrinsic variables. The external variables include the stress/strain path, stress/strain magnitude, stress/ strain rate, stress/strain duration and so on; the intrinsic variables include the soil type, the size of soil particles and the state parameters. The state parameters include the effective stress, the arrangement of soil particles and the stress-strain history. Fig. 2-1 summarizes the relationships between causes and effects in the response of soils to dynamic excitations (Lai et al, 1998).

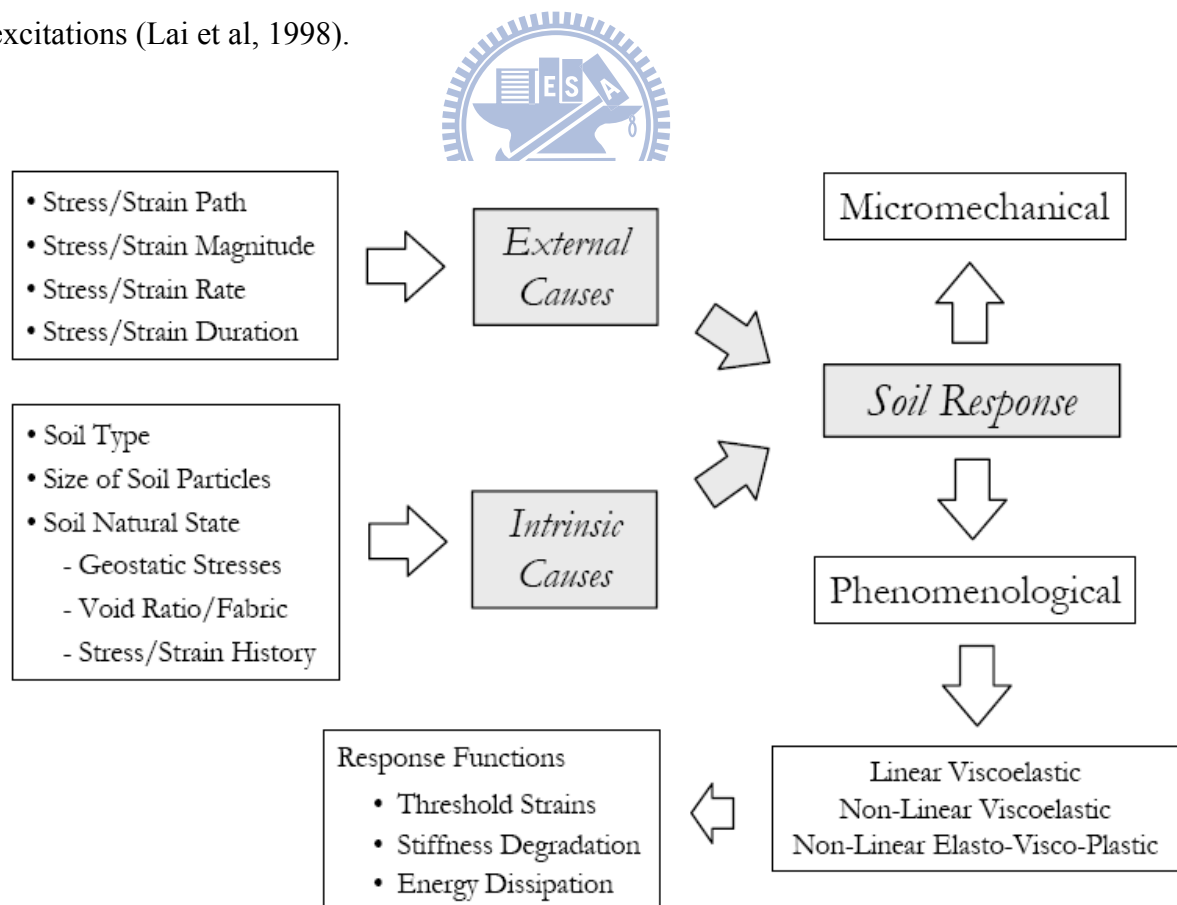


Fig. 2-1 Cause-effect relationships in soil response to dynamic excitations

(Lai et al, 1998)

Experimental evidence also shows that the magnitude of the applied stress or strain is the most important factor among the external variables affecting soil responses to dynamic excitations (Lai et al, 1998). Some important features of soil behaviors are reported for the different intervals of cyclic shear strains. Based on these findings, it was then possible to define a shear strain spectrum for simple shear conditions where distinct types of soil behaviors were identified (EPRI, 1991; Vucetic, 1994).

A threshold shear strain called linear cyclic threshold shear strain (Vucetic, 1994),  $\gamma_t^l$ , is defined for the very small strain region,  $0 < \gamma < \gamma_t^l$ . In this region the soil behaves linearly (without stiffness degradation) but not elastically (with energy dissipation) (Kramer, 1996). The value of  $\gamma_t^l$  varies considerably with the soil type. For example,  $\gamma_t^l$  for sands is on the order of  $10^{-3}\%$ , whereas for normally consolidated clays with a plasticity index (PI) of 50,  $\gamma_t^l$  is on the order of  $10^{-2}\%$  (Lo Presti, 1987; Lo Presti, 1989).

The small strain region is defined as  $\gamma_t^v < \gamma < \gamma_t^v$ , in which  $\gamma_t^v$  is called volumetric threshold shear strain (Vucetic, 1994). Once  $\gamma$  exceeds  $\gamma_t^v$ , there are irrecoverable volumetric change in drained tests and increases of pore-water pressure in undrained tests (Vucetic, 1994). In this region soil behaviors is non-linear and inelastic but material properties do not change rapidly and degrade little with increasing shear strain and number of loading cycles increasing (Lai et al, 1998). The values of  $\gamma_t^v$  are on the order of  $10^{-3}\%$  for gravels,  $10^{-2}\%$  for sands, and  $10^{-1}\%$  for normally consolidated, high plasticity clays (Bellotti et al, 1989; Lo Presti, 1989; Vucetic et al, 1991).

The intermediate strain region is defined as  $\gamma_t^v < \gamma < \gamma_t^{pf}$ , in which  $\gamma_t^{pf}$  is called pre-failure threshold shear strain (Vucetic, 1994). Due to irrecoverable volumetric changes in the previous stage, both instantaneous energy dissipation and losses occur as the number of loading cycles increases (Vucetic, 1994). In this range of deformation the degradation of soil properties with the shear strain is apparent not only within the hysteretic loop but also with

the increase of number of cycles (Ishihara, 1996).

The last region is defined as  $\gamma_i^{pf} < \gamma < \gamma_i^f$  for large strains (EPRI, 1991; Vucetic, 1994). In the region soil behaviors is highly non-linear and inelastic preceding the condition of failure occurring at the failure threshold shear strain  $\gamma_i^f$ .

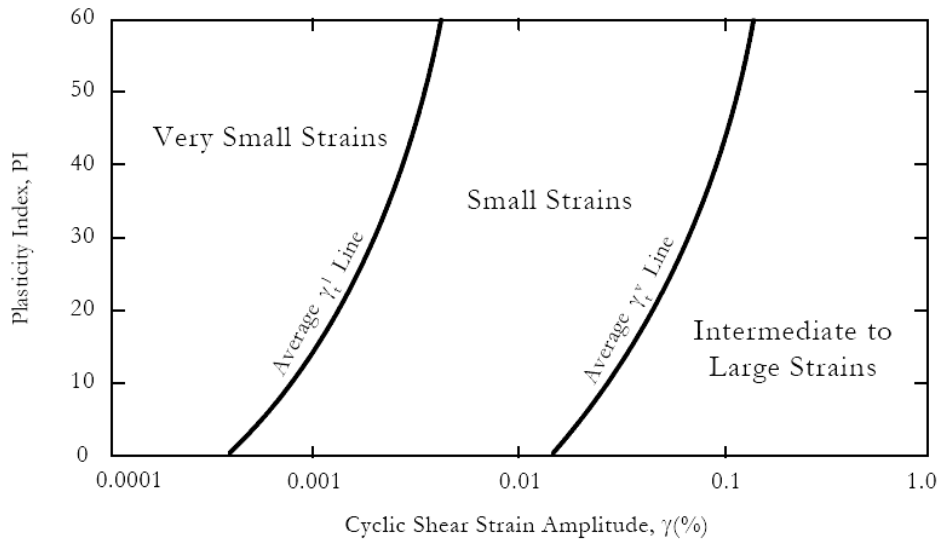


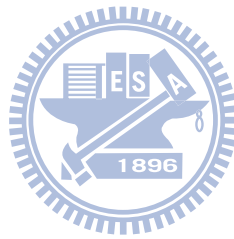
Fig. 2-2 Dependence of threshold shear strains from plasticity index

(After Vucetic, 1994)

Among the threshold strains mentioned above, the  $\gamma_i^l$  and  $\gamma_i^v$  are particularly important. Because  $\gamma_i^l$  separates the linear (though inelastic) responses from the non-linear responses of soil under cyclic excitation. The magnitude of these two threshold shear strains strongly depends on the plasticity of soil. Fig. 2-2 shows the dependence of threshold shear strains on plasticity index (Vucetic, 1994). The  $\gamma_i^v$  distinguishes different types of irrecoverable deformations occurring in soils undergoing harmonic oscillations. These changes result in two observable effects: stiffness reduction and entropy density production (Lai et al, 1998).

Soils show nonlinear variation in shear modulus with shearing strain ( $G-\log \gamma$  curve) and in shear stress with shearing strain ( $\tau-\gamma$  curve). However, in addition to dynamic response, the importance of small-strain stiffness on static deformation analysis has also been pointed out,

especially for analyses of settlement and soil structure interaction. Furthermore, Stokoe et al. (2004) show that  $V_s$  measurement in the field is a critical component in evaluating sample disturbance and in predicting nonlinear  $G - \log \gamma$  and  $\tau - \gamma$  curves. A few successful demonstrations of the use of seismically determined soil modulus for settlement predictions have been presented (see, for example, Shibuya et al. 1994, Jardine et al. 1998, Jamiolkowski et al. 2001, Di Benedetto et al. 2003, and Stokoe et al. 2004).



### 2.1.2 Testing methods

There are many techniques available in-situ or in laboratory for measurement of dynamic soil properties. Each of them has its own advantages and limitations with respect to different engineering problems. As mentioned above, soil behaviors under dynamic loading are mainly affected by the magnitude of shear strains. The Fig. 2-3 shows the ranges of shear strain amplitude of some laboratory and in-situ tests compared to those induced by earthquakes. A broad introduction on laboratory and in-situ tests will be present in the following sections in which tests are categorized by induced strain levels.

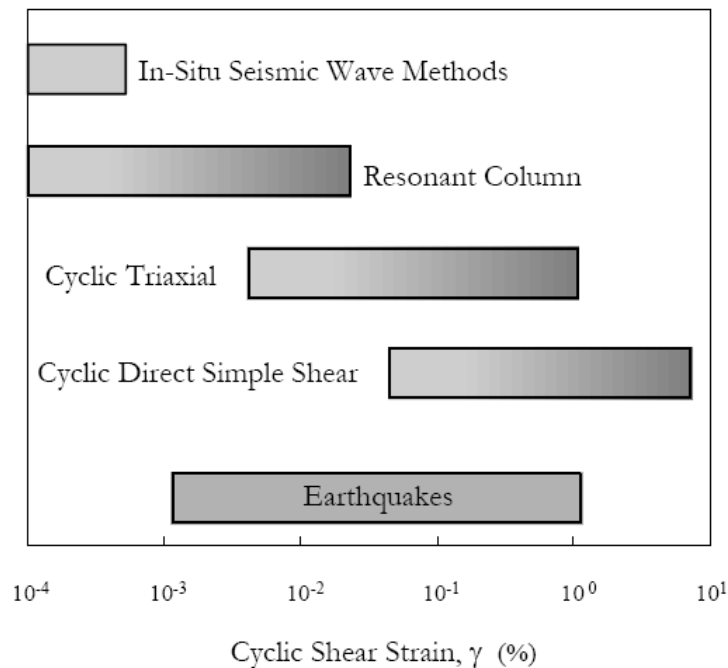


Fig. 2-3 Ranges of variability of cyclic shear strain amplitude in laboratory and in-situ tests

(Ishihara, 1996)

Under a well-controlled circumstance, laboratory tests definitely have advantages on precise measurement, repeatability and controlled boundary condition. However, original conditions of soil are usually altered during sampling tasks and it may be difficult for some kinds of soil to be sampled. Laboratory tests on samples are also time consuming and cost effective.



The main advantage of in-situ tests is no need for sampling. This avoids degrees of disturbance of soil specimen brought by sampling. Another nice feature of in-situ tests is more spatially representative since in-situ tests measure the responses of a relatively large volume of soil. Furthermore many in-situ tests induce the deformations similar to problems of interest, especially seismic tests. However, for most of in-situ tests, field operations lack of standard procedures and data interpretation is generally more difficult. That makes in-situ tests not user friendly. The comparison between in-situ and laboratory tests is summarized on Table 2.1.

Table 2.1 Measurement of low-Strain dynamic properties of soils comparison between in-situ and laboratory techniques  
(Lai et al, 1998)

| Type of Test     | Main Advantages           |                             |                                     | Main Disadvantages                 |                                       |                             |
|------------------|---------------------------|-----------------------------|-------------------------------------|------------------------------------|---------------------------------------|-----------------------------|
| In-Situ Tests    | Account for Scale Factors | Applicable to any Soil Type | No Alteration of Soil Natural State | Difficulties of Interpretation     | Little Control of Boundary Conditions | Lack of General Standards   |
| Laboratory Tests | Accurate Measurements     | Repeatable                  | Controlled Boundary Conditions      | Very Sensitive to Sampling Disturb | Results are Scale Dependent           | Difficult in Granular Soils |

### 2.1.2.1 Laboratory tests

For laboratory tests, as shown in Table 2.2, only few of them provide ability to measure the soil dynamic properties at low strain levels. At high-strain level, the volume of soil usually has irrecoverable change. Under drained condition it is easily to be observed from changes in volumetric strain. When under undrained condition the tendency of volume change in volume results in the change in porewater pressure and effective stress. So methods in this category should have capability to control the porewater drainage and measure the change in volume and stress.

Table 2.2 Laboratory tests for measuring dynamic properties of soil

| Test   | strain level | Note   |
|--|--------------|--|
| Resonant column test   | Low          | <ol style="list-style-type: none"> <li>1. Most common used in laboartory</li> <li>2. Well control testing condition</li> <li>3. Both stiffness and damping of soil measured</li> </ol> |
| Ultrasonic pulse test and Piezo-electric bender element test                           | Low          | <ol style="list-style-type: none"> <li>1. Useful for very soft materials</li> <li>2. Incorporated into conventional cubical txi axial devices and other</li> </ol>                     |
| Cyclic triaxial test<br>Cyclic direct simple shear test<br>Cyclic torsional shear test | High         | <ol style="list-style-type: none"> <li>1. Most commonly used at high strain levels</li> <li>2. Control the porewater drainage and measure the change in volume and stress</li> </ol>   |

### 2.1.2.2 Field tests

Field tests for measuring dynamic properties of soil, as shown in Table 2.3, induce different levels of strain. When selecting an appropriate test for purposes, the representatives of the soil behaviors shall be considered. Another important concern is the necessity of invasive tasks. Some of the tests need drilling of boreholes or penetration of testing devices, while some can be performed on the ground surface non-destructively. Tests performed on the ground surface are usually more efficient and cost effective. They are practically useful for geomaterials in which drilling and penetration are difficult. But the information gained from borehole tests is more direct than tests on ground surface.

Most of the high-strain tests aim to measure characteristics like soil strength at high-strain level and can be correlated to the low-strain behaviors. Several high-strain tests are common used in geotechnical engineering of different purposes. Basically the strains induced by low-strain tests are usually small enough for assuming linear stress- strain behavior of soil, in other words, the strain is smaller than the linear cyclic threshold shear

strain  $\gamma_t^1$ . Most of them are based on the theory of wave propagation in linear materials. The measured body or surface wave velocity and frequencies or wavelengths can all be directly related to the low-strain mechanic modulus of a soil.

Seismic tests involve generating a transient or steady stress wave and interpreting soil dynamic properties via measurements made at one or more different locations. Stress waves may be generated by various seismic sources ranging from sledgehammers to buried explosive charges. The measurement can be the distance and traveling time of waves or a digitized wavefield recorded by array receivers. For those needing boreholes, results (mostly wave velocities verse depth profile) can be easily obtained from simple computation of traveling time and distance of wave. But for those performed on the ground surface, the characteristic properties (such as traveling time- distance relation, dispersion relation) involve the signal processing of raw data (recorded digitized wavefield) and final results need inversion based on certain theories and hypothesis. The more complicated the interpretation process, the more uncertainty of results and expertise of testers required.

Non-invasive methods for measuring shear wave velocity include shear wave refraction survey and surface wave methods. Refraction techniques for near surface survey are traditionally based on head-wave methods. Recent developments in refraction tomography have enhanced the spatial resolution of the refraction survey. However, the results are subject to limitation that velocity must increase with depth. Furthermore, S-wave refraction survey may not provide the true S-wave velocity because of wave-type conversion in an area of non-horizontal layers. Surface wave methods do not suffer from aforementioned problems associated with refraction survey, hence are considered of special interest for the site surveys of geotechnical problems.

Table 2.3 Field tests for measuring dynamic properties of soil

| Test   | strain level | Borehole required | Remarks  |
|--|--------------|-------------------|--|
| Seismic reflection test  | Low          | No                | Reflected signals are recorded typically using common midpoint arrays. Velocity between reflectors may be estimated during normal move out correction. |
| Seismic refraction test  | Low          | No                | Velocity profile is deduced from recording the first arrival times versus source-to-receiver distance.   |
| Seismic tests using surface wave   | Low          | No                | Steady State Rayleigh Wave method (SSRW)<br>Spectral Analysis of Surface Waves Method (SASW)<br>Multi-station Analysis of Surface Waves method (MASW)  |
| Suspension logging test  | Low          | Yes               | Frequency components are much higher than those of interest in geotechnical earthquake engineering   |
| Seismic cross-hole test  | Low          | Yes               | At least two boreholes required  |
| Seismic down-hole (up-hole) test   | Low          | Yes               | Only one borehole required   |
| Standard Penetration Test (SPT)<br>Cone Penetration Test (CPT)<br>Dilatometer Test (DMT)<br>Pressuremeter Test (PMT) | High         | Yes               | Penetration or borehole required   |

## 2.2 Wave propagation and computation of surface wave

There are various kinds of wave produced when an impulse was applied on the ground surface. These waves generally are categorized into two main types: body waves and surface waves. Body waves travel through the interior of the medium. Surface waves are the result of the interaction between body waves, the free surface and surficial layers of the medium. They travel along the surface with amplitudes decreasing roughly exponentially with depth.

Body waves are of two types: P wave and S wave. P wave is also referred to as primary, compressional or longitudinal wave consisting of successive compression and relaxation of the medium. The individual particle moves parallel to the direction of P wave propagation. S wave is also known as secondary, shear or transverse wave. It induces the shearing deformation as it traveling through the medium. The particle motion when S wave traveling is perpendicular to the direction of S wave propagation. For a three dimensional coordination, the S wave has two components: the movement on vertical plane is SV wave and the movement on horizontal plane is SH wave. The velocities of body wave propagation depend on the stiffness of medium.

The surface waves include are Rayleigh wave and Love wave. Rayleigh wave generated by interaction of P wave and SV wave involves both vertical and horizontal particle motions. Love wave is produced by the interaction of SH wave with a surficial soft layer and it has no vertical particle motion. There is no Love wave on the surface in a half space without any interface of layers. The basic theory of elastic wave propagation and the characteristics of Rayleigh wave, the main role of this study, will be introduced in the following paragraphs.

## 2.2.1 Basic theory of elastic wave propagation

### 2.2.1.1 Stress, strain and their relationship

➤ Definition and notation of stress

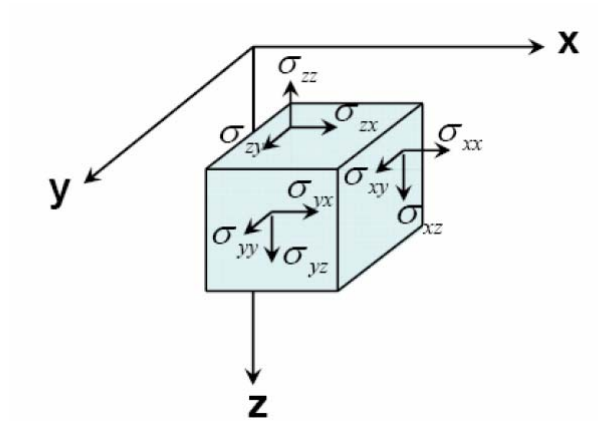


Fig. 2-4 Stress notation of an element in an x-y-z Cartesian coordination

$\sigma_{ij}$  is usually used as the symbol representing stress. In the subscript, the first letter denotes the axis perpendicular to the plane in which the stress acts and the second denotes the direction of stress. For a small element in an x-y-z Cartesian coordination, there are totally nine components acting on its face (as shown on Fig. 2-4).

The normal stresses are denoted as:

$$\sigma_{xx}, \sigma_{yy}, \sigma_{zz}$$

The shear stresses are denoted as:

$$\sigma_{xy}, \sigma_{xz}, \sigma_{yx}, \sigma_{yz}, \sigma_{zx}, \sigma_{zy}$$

For the moment equilibrium of the element, it requires that  $\sigma_{xy} = \sigma_{yx}$ ,  $\sigma_{xz} = \sigma_{zx}$ ,  $\sigma_{yz} = \sigma_{zy}$ . So there are only six independent components required for describing the state of stresses of an element.

➤ Definition and notation of displacement and strain

Let  $u_i$  represent the displacement in  $i$  direction. The relationship between displacements and strains can be defined as:

$$\varepsilon_{ij} = \frac{1}{2} \left( \frac{\partial u_i}{\partial j} + \frac{\partial u_j}{\partial i} \right) \quad (2-1)$$

For example,

$$\begin{aligned} \varepsilon_{xx} &= \frac{1}{2} \left( \frac{\partial u_x}{\partial x} + \frac{\partial u_x}{\partial x} \right) = \frac{\partial u_x}{\partial x} \\ \varepsilon_{xy} &= \frac{1}{2} \left( \frac{\partial u_x}{\partial y} + \frac{\partial u_y}{\partial x} \right) \\ \varepsilon_{xz} &= \frac{1}{2} \left( \frac{\partial u_x}{\partial z} + \frac{\partial u_z}{\partial x} \right) \end{aligned} \quad (2-2)$$

➤ Stress-strain relationship

For a homogeneous and isotropic linear elastic body, the stress-strain constitutive law can be described by two Lamé's constants,  $\lambda$  and  $\mu$ , and Hooke's law. The generalized form can be written as:

$$\sigma_{ij} = \lambda \varepsilon_{kk} \delta_{ij} + 2\mu \varepsilon_{ij} \quad (2-3)$$

where the volumetric strain  $\varepsilon_{kk} = \varepsilon_{xx} + \varepsilon_{yy} + \varepsilon_{zz}$  and  $\delta_{ij}$  represents Kronecker delta function. For example, substituting (2-2) into (2-3) gives

$$\begin{aligned} \sigma_{xx} &= \lambda \left( \frac{\partial u_x}{\partial x} + \frac{\partial u_y}{\partial y} + \frac{\partial u_z}{\partial z} \right) + 2\mu \frac{\partial u_x}{\partial x} \\ \sigma_{xy} &= \mu \left( \frac{\partial u_x}{\partial y} + \frac{\partial u_y}{\partial x} \right) \\ \sigma_{xz} &= \mu \left( \frac{\partial u_x}{\partial z} + \frac{\partial u_z}{\partial x} \right) \end{aligned} \quad (2-4)$$

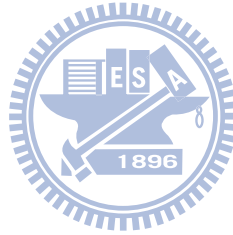
**2.2.1.2 Equation of motion for elastic solid**

Consider the infinitesimal element shown on Fig. 2-4 with dimensions of  $dx$ ,  $dy$  and  $dz$  respectively in  $x$ ,  $y$  and  $z$  direction. In the  $x$  direction, the unbalanced external force must be balanced by an inertial force in that direction. So,

$$\begin{aligned} \rho(dx dy dz) \frac{\partial^2 u_x}{\partial t^2} &= \left( \sigma_{xx} + \frac{\partial \sigma_{xx}}{\partial x} dx \right) dy dz - \sigma_{xx} dy dz \\ &+ \left( \sigma_{yx} + \frac{\partial \sigma_{yx}}{\partial y} dy \right) dx dz - \sigma_{yx} dx dz \\ &+ \left( \sigma_{zx} + \frac{\partial \sigma_{zx}}{\partial z} dz \right) dx dy - \sigma_{zx} dx dy \\ &+ f_x \end{aligned} \quad (2-5)$$

in which  $\rho$  is density and  $f_i$  is the body force in  $i$  direction. Supposing  $f_i = 0$ , repeating the operation in  $y$  and  $z$  directions gives

$$\begin{aligned} \rho \frac{\partial^2 u_x}{\partial t^2} &= \frac{\partial \sigma_{xx}}{\partial x} + \frac{\partial \sigma_{yx}}{\partial y} + \frac{\partial \sigma_{zx}}{\partial z} \\ \rho \frac{\partial^2 u_y}{\partial t^2} &= \frac{\partial \sigma_{xy}}{\partial x} + \frac{\partial \sigma_{yy}}{\partial y} + \frac{\partial \sigma_{zy}}{\partial z} \\ \rho \frac{\partial^2 u_z}{\partial t^2} &= \frac{\partial \sigma_{xz}}{\partial x} + \frac{\partial \sigma_{yz}}{\partial y} + \frac{\partial \sigma_{zz}}{\partial z} \end{aligned} \quad (2-6)$$



(2-6) represent the three dimensional equations of motion of solid. The equations are derived on the basis of equilibrium, therefore it is valid for solids of any constitutive model. Substituting (2-4) derived from Hooke's law into the equations of motion and repeating the operation in  $y$  and  $z$  directions, the equations of motion expressed in term of displacement are shown as following:

$$\begin{aligned} \rho \frac{\partial^2 u_x}{\partial t^2} &= (\lambda + \mu) \frac{\partial}{\partial x} \left( \frac{\partial u_x}{\partial x} + \frac{\partial u_y}{\partial y} + \frac{\partial u_z}{\partial z} \right) + \mu \left( \frac{\partial^2 u_x}{\partial x^2} + \frac{\partial^2 u_x}{\partial y^2} + \frac{\partial^2 u_x}{\partial z^2} \right) \\ \rho \frac{\partial^2 u_y}{\partial t^2} &= (\lambda + \mu) \frac{\partial}{\partial y} \left( \frac{\partial u_x}{\partial x} + \frac{\partial u_y}{\partial y} + \frac{\partial u_z}{\partial z} \right) + \mu \left( \frac{\partial^2 u_y}{\partial x^2} + \frac{\partial^2 u_y}{\partial y^2} + \frac{\partial^2 u_y}{\partial z^2} \right) \\ \rho \frac{\partial^2 u_z}{\partial t^2} &= (\lambda + \mu) \frac{\partial}{\partial z} \left( \frac{\partial u_x}{\partial x} + \frac{\partial u_y}{\partial y} + \frac{\partial u_z}{\partial z} \right) + \mu \left( \frac{\partial^2 u_z}{\partial x^2} + \frac{\partial^2 u_z}{\partial y^2} + \frac{\partial^2 u_z}{\partial z^2} \right) \end{aligned} \quad (2-7)$$

If the expression of vector is applied, equations (2-7) can be expressed as,



$$\rho \ddot{u} = (\lambda + \mu) \nabla(\nabla \cdot u) + \mu \nabla^2 u \quad (2-8)$$

in which, overdots are used to indicate time derivatives (e.g.,  $\dot{u} = \partial u / \partial t$ ,  $\ddot{u} = \partial^2 u / \partial t^2$ ),  $\nabla^2$  represents the Laplacian operator. The Laplacian operator has another alternative expression:

$$\nabla^2 u = \nabla(\nabla \cdot u) - (\nabla \times \nabla \times u) \quad (2-9)$$

Then (2-8) can be written as following:

$$\rho \ddot{u} = (\lambda + 2\mu) \nabla(\nabla \cdot u) - \mu(\nabla \times \nabla \times u) \quad (2-10)$$

According to the Helmholtz decomposition theorem, any vector field  $u$  can be considered to be generated by a pair of potentials: a scalar potential  $\phi$  and a vector potential  $\Psi$ .

$$u = \nabla \phi + \nabla \times \Psi \quad (2-11)$$

in which,

$$\nabla \times \phi = 0, \quad \nabla \cdot \Psi = 0 \quad (2-12)$$

Substituting (2-11) into (2-10) gives,

$$\nabla \left[ (\lambda + 2\mu) \nabla^2 \phi - \rho \ddot{\phi} \right] + \nabla \times \left[ \mu \nabla^2 \Psi - \rho \ddot{\Psi} \right] = 0 \quad (2-13)$$

let

$$v_p = \sqrt{\frac{\lambda + 2\mu}{\rho}}, \quad v_s = \sqrt{\frac{\mu}{\rho}} \quad (2-14)$$

Substituting (2-14) into (2-13), then (2-13) has solutions if the (2-15) are satisfied.

$$\nabla^2 \phi - \frac{1}{v_p^2} \ddot{\phi} = 0, \quad \nabla^2 \Psi - \frac{1}{v_s^2} \ddot{\Psi} = 0 \quad (2-15)$$

(2-15) are the wave equations, in which  $v_p$  and  $v_s$  are the propagating velocities of P wave and S wave respectively. As it shown, the displacements of solid after disturbance can be categorized into those related to P wave and those related to S wave. The propagating velocities of body waves in a solid are not correlative with the frequency of excitation but

correlative only with the Lamé's constants of the medium. From (2-14), it is obvious that  $v_p$  is greater than  $v_s$ . It can be observed on the seismogram of earthquake that the displacements caused by P wave always occur earlier than those caused by S wave.

The separation of variables is applied here for solution of wave equations (2-15).

Suppose

$$\phi(x, y, z, t) = X(x)Y(y)Z(z)T(t) \quad (2-16)$$

Substituting (2-16) into (2-15), the general solution of the wave scalar potential for plane waves propagating in any direction is obtained,

$$\phi(x, y, z, t) = A \exp\left[\pm i\left(\omega t \pm k_{px}^2 x \pm k_{py}^2 y \pm k_{pz}^2 z\right)\right] \quad (2-17)$$

in which,

$$k_{px}^2 + k_{py}^2 + k_{pz}^2 = \frac{\omega^2}{v_p^2} \quad (2-18)$$

(2-18) defines the surface of plane waves propagating in directions of  $(k_{px}, k_{py}, k_{pz})$  with a P wave velocity of  $v_p$  in a Cartesian coordinate. The constant A represents the amplitude. In the same way, the general solution of the wave vector potential for plane waves propagating in any direction can be obtained.

$$\Psi(x, y, z, t) = B \exp\left[\pm i\left(\omega t \pm k_{sx}^2 x \pm k_{sy}^2 y \pm k_{sz}^2 z\right)\right] \quad (2-19)$$

in which,

$$k_{sx}^2 + k_{sy}^2 + k_{sz}^2 = \frac{\omega^2}{v_s^2} \quad (2-20)$$

(2-19) defines the surface of plane waves propagating in directions of  $(k_{sx}, k_{sy}, k_{sz})$  with an S wave velocity of  $v_s$  in a Cartesian coordinate. The constant B represents the amplitude.

Base on the hypothesis of no inference when P and S wave propagating, the displacement field  $u$  caused by excitation can be represented by the linear combination of the vibrations caused by P wave and S wave. According to the Helmholtz theorem, the

displacement field  $u$  can be decomposed into:

$$u = u_p + u_s = \nabla \phi + \nabla \times \Psi \quad (2-21)$$

in which  $u_p, u_s$  represent the displacement caused by P wave and S wave respectively. So,

$$u_p = \nabla \phi = \frac{\partial \phi}{\partial x} \hat{x} + \frac{\partial \phi}{\partial y} \hat{y} + \frac{\partial \phi}{\partial z} \hat{z} \quad (2-22)$$

$$u_s = \nabla \times \Psi = \left( \frac{\partial \Psi_z}{\partial y} - \frac{\partial \Psi_y}{\partial z} \right) \hat{x} + \left( \frac{\partial \Psi_x}{\partial z} - \frac{\partial \Psi_z}{\partial x} \right) \hat{y} + \left( \frac{\partial \Psi_y}{\partial x} - \frac{\partial \Psi_x}{\partial y} \right) \hat{z}$$

in which,  $\Psi_x, \Psi_y, \Psi_z$  represent the components of  $\Psi$  in  $x, y, z$  directions. Equation (2-22)

also satisfies the form of general solution as shown in (2-19).  $\hat{x}, \hat{y}, \hat{z}$  represent the unit vectors in  $x, y, z$  directions. For simplifying the problem, the plane wave is supposed that  $k_{py}, k_{sy} = 0$ , which means the wave is steady in  $y$  direction,  $\partial \phi / \partial y \rightarrow 0$  and  $\partial \Psi_i / \partial y \rightarrow 0$ . Then  $u_s$

can be expressed as:

$$u_p = \frac{\partial \phi}{\partial x} \hat{x} + \frac{\partial \phi}{\partial z} \hat{z} \quad (2-23)$$

$$u_s = \left( -\frac{\partial \Psi_y}{\partial z} \right) \hat{x} + \left( \frac{\partial \Psi_x}{\partial z} - \frac{\partial \Psi_z}{\partial x} \right) \hat{y} + \left( \frac{\partial \Psi_y}{\partial x} \right) \hat{z}$$

The equation (2-21) can be re-written by substituting (2-22) and (2-23).

$$u = \left( \frac{\partial \phi}{\partial x} - \frac{\partial \Psi_y}{\partial z} \right) \hat{x} + \left( \frac{\partial \Psi_x}{\partial z} - \frac{\partial \Psi_z}{\partial x} \right) \hat{y} + \left( \frac{\partial \phi}{\partial z} + \frac{\partial \Psi_y}{\partial x} \right) \hat{z} \quad (2-24)$$

From the result of (2-24), the displacement in  $y$  direction depends only on S wave. But displacements in  $x$  and  $z$  direction is a combination provided by P wave and S wave and the interference of S wave here is different from the interference of S wave in  $y$  direction. Distinctly, the displacement field  $u$  can be discussed separately in the  $x$ - $z$  plane and  $y$  direction. The displacement in  $y$  direction is represented by SH wave and the displacement in  $x$ - $z$  plane is represented by P-SV wave.

### 2.2.1.3 Rayleigh wave in a homogeneous halfspace

A free surface is necessary for occurrence of surface waves. The main characteristic of surface waves is that the carried energy decays with increasing depth. Surface wave in a homogeneous halfspace is the focus of this section. From (2-24), it is clear that the components of the displacement field  $u$  in  $x, y, z$  directions are:

$$\begin{aligned} u_x &= \frac{\partial \phi}{\partial x} - \frac{\partial \Psi_y}{\partial z} \\ u_y &= \frac{\partial \Psi_x}{\partial z} - \frac{\partial \Psi_z}{\partial x} \\ u_z &= \frac{\partial \phi}{\partial z} + \frac{\partial \Psi_y}{\partial x} \end{aligned} \quad (2-25)$$

As mentioned above, the  $u_y$  depends only on the vector potential of S wave. Keeping it in term of  $u_y$  does not affect the form of general solution. For a wave with a frequency of  $\omega$  and velocity of  $v_R$  traveling through a homogeneous halfspace, its  $\phi$ ,  $\Psi_y$  and  $u_y$  can be supposed as:

$$\begin{aligned} \phi &= f(z) \exp[ik(x - v_R t)] \\ \Psi_y &= g(z) \exp[ik(x - v_R t)] \\ u_y &= h(z) \exp[ik(x - v_R t)] \end{aligned} \quad (2-26)$$

in which,  $f(z)$ ,  $g(z)$ ,  $h(z)$  are used for the phenomenon that energy decays gradually with depth ( $z$ ) increasing;  $k = \omega / v_R$  represents spatial frequency. Putting (2-26) into (2-15) leads to

$$\begin{aligned} f''(z) + k^2 r^2 f(z) &= 0 \\ g''(z) + k^2 s^2 g(z) &= 0 \\ h''(z) + k^2 s^2 h(z) &= 0 \end{aligned} \quad (2-27)$$

in which

$$\begin{aligned} r &= \left( \frac{v_R^2}{v_p^2} - 1 \right)^{1/2} \\ s &= \left( \frac{v_R^2}{v_s^2} - 1 \right)^{1/2} \end{aligned} \quad (2-28)$$

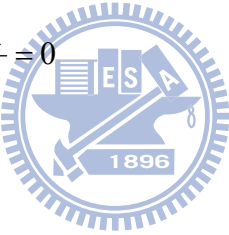
The solutions of (2-27) can be expressed as:

$$\begin{aligned}
f(z) &= A' \exp(ikrz) + A \exp(-ikrz) \\
g(z) &= B' \exp(iksz) + B \exp(-iksz) \\
h(z) &= C' \exp(iksz) + C \exp(-iksz)
\end{aligned} \tag{2-29}$$

in which,  $A, A', B, B', C, C'$  are all arbitrary constants. The constants  $A', B', C'$  equal to zero due to the behavior of energy decay with depth increasing. Both of  $r$  and  $s$  are imaginary numbers, which implies  $v_p > v_s > v_R$ . Substituting (2-29) into (2-26) gives,

$$\begin{aligned}
\phi &= A \exp[-ikrz + ik(x - v_R t)] \\
\Psi_y &= B \exp[-ikrz + ik(x - v_R t)] \\
u_y &= C \exp[-ikrz + ik(x - v_R t)]
\end{aligned} \tag{2-30}$$

The boundary conditions are necessary for resolving the constants  $A, B, C$ . On the free surface, the stresses in  $z$  direction must be zero,  $\sigma_{zz} = 0, \sigma_{zx} = 0, \sigma_{zy} = 0$ . The boundary conditions here are:

$$\begin{aligned}
\sigma_{zz} &= \lambda \left( \frac{\partial u_x}{\partial x} + \frac{\partial u_y}{\partial y} + \frac{\partial u_z}{\partial z} \right) + 2\mu \frac{\partial u_z}{\partial z} = 0 \\
\sigma_{zx} &= \mu \left( \frac{\partial u_z}{\partial x} + \frac{\partial u_x}{\partial z} \right) = 0 \\
\sigma_{zy} &= \mu \left( \frac{\partial u_z}{\partial y} + \frac{\partial u_y}{\partial z} \right) = 0
\end{aligned} \tag{2-31}$$


Substituting (2-24) and (2-29) into (2-31), that gives:

$$\begin{aligned}
2 \frac{\partial^2 \phi}{\partial z \partial x} + \frac{\partial^2 \Psi_y}{\partial x^2} - \frac{\partial^2 \Psi_y}{\partial y^2} &= 0 \\
\frac{\partial u_y}{\partial z} &= 0 \\
(\lambda + 2\mu) \frac{\partial^2 \phi}{\partial z \partial x} + \lambda \frac{\partial^2 \phi}{\partial x^2} + 2\mu \frac{\partial^2 \Psi_y}{\partial z \partial x} &= 0
\end{aligned} \tag{2-32}$$

Substituting the third of (2-30) into the second of (2-32) resolves that the constant  $C$  equals zero which means no displacement in  $y$  direction ( $u_y=0$ ). It implies the surface wave in a homogeneous halfspace does not contain Love wave. Next, substituting the first and the second of (2-30) into the first and third of (2-32) respectively obtains a homogeneous system

of linear equations.

$$\begin{aligned} 2rA - (1 - S^2)B &= 0 \\ [v_p(r^2 + 1) - 2v_s]A - 2v_s^2sB &= 0 \end{aligned} \quad (2-33)$$

If nontrivial solutions of (2-33) exist, the following requirement should be satisfied,

$$\begin{vmatrix} 2r & -(1 - s^2) \\ v_p(r^2 + 1) - 2v_s & -2v_s^2s \end{vmatrix} = 0 \quad (2-34)$$

Calculating the determinant gives

$$[v_p(r^2 + 1) - 2v_s](1 - s^2) - 4rsv_s^2 = 0 \quad (2-35)$$

Substituting (2-28) into (2-35) and rearranging,

$$\left(2 - \frac{v_R^2}{v_s^2}\right)^2 = 4\left(1 - \frac{v_R^2}{v_p^2}\right)^{1/2}\left(1 - \frac{v_R^2}{v_s^2}\right)^{1/2} \quad (2-36)$$

(2-36) is first presented by Rayleigh in 1887 for the wave velocity of Rayleigh wave. The equation clearly shows that the propagating velocity of Rayleigh wave in a homogeneous halfspace is irrelevant to frequency (which means non-dispersive).

Let

$$\xi = \frac{v_R}{v_s}, \quad q = \frac{v_s}{v_p} \quad (2-37)$$

Substituting (2-37) into (2-36) and rearranging,

$$\xi^3 - 8\xi^2 + 8(3 - 2q)\xi + 16(q - 1) = 0 \quad (2-38)$$

in which, q is a constant once the Lamé's constants of the homogeneous halfspace are assured.  $\xi$  is the only unknown which have three nontrivial solutions for the cubic equation. The propagating velocity of Rayleigh wave,  $v_R$ , wave should satisfy the requirement of  $v_p > v_s > v_R$ . Therefore the solution satisfying  $\xi < 1$  is the one for the propagating velocity of Rayleigh wave.

One can express (2-39) in terms of Poisson's ratio and solve the cubic equation. For

typical values of Poisson's ratio,  $0.2 < \nu < 0.4$ , the velocity of Rayleigh wave ranges from  $0.9 v_s$  to  $0.95 v_s$ . The ratios between  $v_R$ ,  $v_p$  and  $v_s$  as a function of  $\nu$  is shown in Fig. 2-5. The particle motion of a propagating Rayleigh wave in a homogeneous half space transits from retrograde to prograde elliptical with depth as shown in Fig. 2-6 and Fig. 2-7. The Rayleigh wave comprises both compressional and rotational components and the eccentricity of the ellipse for locus of particle motion depends on Poisson's ratio.

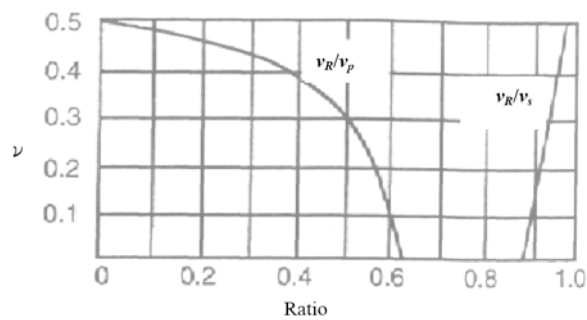


Fig. 2-5 The ratio of Rayleigh wave velocity,  $v_R$ , verse body wave velocities as a function of Poisson ratio,  $\nu$  (Sheriff et al, 1982)

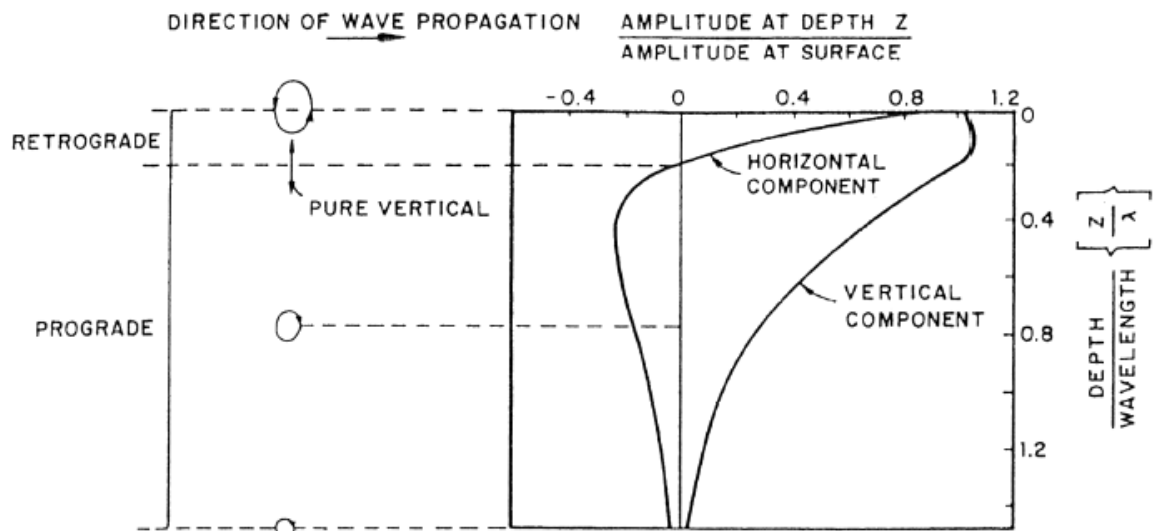


Fig. 2-6 Rayleigh wave particle motion in a homogeneous, isotropic half space; retrograde at the surface, passing through purely vertical at about  $\lambda/5$  then becoming prograde at depth

(Cuellar, 1997)

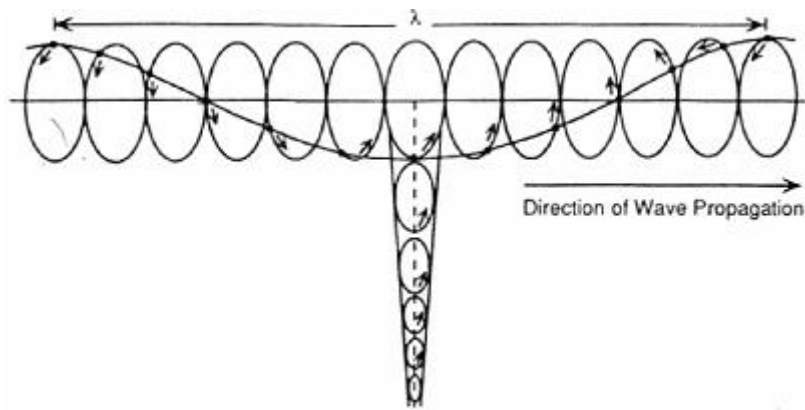


Fig. 2-7 Particle motions of Rayleigh wave over one wavelength along the surface and as a function of depth

(Sheriff et al, 1982)

#### 2.2.1.4 Rayleigh wave in a vertically heterogeneous halfspace

The surface wave applied in this study is Rayleigh wave due to the interference of P wave and SV wave. Its most important characteristic is dispersion due to the stiffness variation with depth of the tested strata. Dispersion means the propagating velocity of wave varies with frequency.

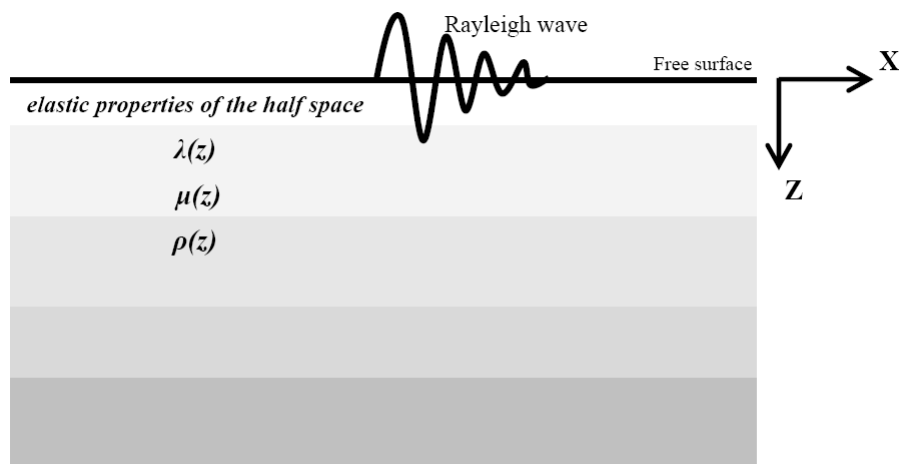


Fig. 2-8 The model of a vertically heterogeneous halfspace



Considering a vertically heterogeneous halfspace as shown in Fig. 2-8, the elastic parameters depend only on the depth  $z$ . The following discussion focuses only on the part related to P-SV wave, so the component of displacement on  $y$  direction,  $u_y$ , is assumed to be zero. For a plane wave propagating in  $+x$  direction, it can be expressed as:

$$\begin{aligned} u_x &= r_1(k, z, \omega) \exp[i(kx - \omega t)] \\ u_z &= ir_2(k, z, \omega) \exp[i(kx - \omega t)] \end{aligned} \quad (2-39)$$

in which,  $r_1(k, z, \omega)$  and  $r_2(k, z, \omega)$  represent the amplitudes of components of the displacement in  $x$  and  $z$  directions respectively. Both have characteristics of decay with  $z$  increasing and each different frequency  $\omega$  with a corresponding spatial frequency  $k$ .

Due to the continuity of stress between layers, so let

$$\begin{aligned} \sigma_{zx} &= r_3(k, z, \omega) \exp[i(kx - \omega t)] \\ \sigma_{zz} &= ir_4(k, z, \omega) \exp[i(kx - \omega t)] \end{aligned} \quad (2-40)$$

in which,  $r_3(k, z, \omega)$  and  $r_4(k, z, \omega)$  represent the amplitudes of stresses on plane  $z$  in  $x$  and  $z$  directions respectively. Both have characteristics of decay with  $z$  increasing and each different frequency  $\omega$  with a corresponding spatial frequency  $k$ .

For solutions of  $r_1(k, z, \omega)$ ,  $r_2(k, z, \omega)$ ,  $r_3(k, z, \omega)$  and  $r_4(k, z, \omega)$ , it is necessary to obtain four equations for four unknowns. Two can be obtained from the stress-strain relationship,

$$\begin{aligned} \sigma_{zz} &= \lambda(z) \left( \frac{\partial u_x}{\partial x} + \frac{\partial u_z}{\partial z} \right) + 2\mu(z) \frac{\partial u_z}{\partial z} \\ \sigma_{zx} &= \mu(z) \left( \frac{\partial u_z}{\partial x} + \frac{\partial u_x}{\partial z} \right) \end{aligned} \quad (2-41)$$

Substituting (2-39) into (2-41) gives

$$\begin{aligned} \sigma_{zz} &= i(\lambda(z) + 2\mu(z)) \frac{dr_2}{dz} \exp[i(kx - \omega t)] + i\lambda(z)kr_1 \exp[i(kx - \omega t)] \\ \sigma_{zx} &= \mu(z) \left( -kr_2 \exp[i(kx - \omega t)] + \frac{dr_1}{dz} \exp[i(kx - \omega t)] \right) \end{aligned} \quad (2-42)$$

Then substituting (2-40) into (2-42) and rearranging,

$$\begin{aligned}\frac{dr_1}{dz} &= \frac{1}{\mu(z)}r_3 + kr_2 \\ \frac{dr_2}{dz} &= \frac{1}{\lambda(z) + 2\mu(z)}[r_4 - \lambda(z)kr_1]\end{aligned}\tag{2-43}$$

(2-43) are two of four equations for solutions. The other two can be found by means of the equations of motion (2-7),

$$\begin{aligned}\rho(z)\frac{\partial^2 u_x}{\partial t^2} &= (\lambda(z) + \mu(z))\frac{\partial}{\partial x}\left(\frac{\partial u_x}{\partial x} + \frac{\partial u_z}{\partial z}\right) + \mu(z)\left(\frac{\partial^2 u_x}{\partial x^2} + \frac{\partial^2 u_x}{\partial z^2}\right) \\ \rho(z)\frac{\partial^2 u_z}{\partial t^2} &= (\lambda(z) + \mu(z))\frac{\partial}{\partial z}\left(\frac{\partial u_x}{\partial x} + \frac{\partial u_z}{\partial z}\right) + \mu(z)\left(\frac{\partial^2 u_z}{\partial x^2} + \frac{\partial^2 u_z}{\partial z^2}\right)\end{aligned}\tag{2-44}$$

Substituting (2-39) and (2-43) into (2-44) and rearranging,

$$\begin{aligned}\frac{dr_3}{dz} &= k^2\left[-\rho(z)v_R^2\left(\frac{4\mu(z)(\lambda(z) + \mu(z))}{\lambda(z) + 2\mu(z)}\right)\right]r_1 + \frac{k\lambda(z)}{\lambda(z) + 2\mu(z)}r_4 \\ \frac{dr_4}{dz} &= -\rho(z)v_R^2k^2r_2 - kr_3\end{aligned}\tag{2-45}$$

Combining equations (2-43) and (2-45), the motion-stress vector (Aki et al, 2002) can be formed,

$$\frac{d}{dz}\begin{bmatrix} r_1 \\ r_2 \\ r_3 \\ r_4 \end{bmatrix} = \begin{bmatrix} 0 & k(\omega) & \frac{1}{\mu(z)} & 0 \\ \frac{-k(\omega)\lambda(z)}{\lambda(z) + 2\mu(z)} & 0 & 0 & \frac{1}{\lambda(z) + 2\mu(z)} \\ \zeta(z)k(\omega)^2 - \rho(z)\omega^2 & 0 & 0 & \frac{k(\omega)\lambda(z)}{\lambda(z) + 2\mu(z)} \\ 0 & -\rho(z)\omega^2 & -k(\omega) & 0 \end{bmatrix}\begin{bmatrix} r_1 \\ r_2 \\ r_3 \\ r_4 \end{bmatrix}\tag{2-46}$$

in which,

$$\zeta(z) = \frac{4\mu(z)[\lambda(z) + \mu(z)]}{\lambda(z) + 2\mu(z)}\tag{2-47}$$

Let  $\mathbf{f}(z) = [r_1 \ r_2 \ r_3 \ r_4]^T$  and a matrix  $A(z)$  denoting the 4x4 matrix whose elements are functions of stiffness, wavenumber and frequency. (2-47) can be expressed in the form of vector as,

$$\frac{d\mathbf{f}(z)}{dz} = A(z)\mathbf{f}(z) \quad (2-48)$$

### 2.2.2 Computation of theoretical dispersion curve

(2-48) defines a linear eigenvalue problem with displacement eigenfunctions  $r_1$  and  $r_2$  and stress eigenfunctions  $r_3$  and  $r_4$ . The boundary conditions with the eigenproblem are:

$$\begin{aligned} r_3(k, z, \omega) = 0, \quad r_4(k, z, \omega) = 0 \quad \text{at } z = 0 \\ \mathbf{f}(k, z, \omega) \rightarrow 0 \text{ as } z \rightarrow \infty \end{aligned} \quad (2-49)$$

And for the continuity of the stress and displacement fields, at each interface of layers in a vertical heterogeneous medium,

$$\begin{aligned} u(r, z^+) = u(r, z^-) \\ \sigma(r, z^+) \cdot n = \sigma(r, z^-) \cdot n \end{aligned} \quad (2-50)$$

For a give frequency  $\omega$ , (2-48) has nontrivial solutions existing only for specific wavenumbers  $k_j = k_j(\omega)$ . The particular  $k_j$  are the eigenvalues of the eigenproblem and the corresponding  $r_j(k_j, z, \omega)$  are the eigenfunctions.  $k_j = k_j(\omega)$  is known in the implicit form as:

$$F_R[\lambda(z), \mu(z), \rho(z), k_j, \omega] = 0 \quad (2-51)$$

where  $F_R[*]$  is a function of Lamé's constants, density, wavenumber and frequency of excitation. The relationship  $F_R[*] = 0$  is called Rayleigh dispersion equation. The relationship shows that Rayleigh wave possesses the characteristic of dispersion in vertically heterogeneous halfspace. Each  $k_j$  and its corresponding  $r_j(k_j, z, \omega)$  defines a mode of propagation and there are  $M$  modes of propagation at any given frequency. Due to multiple reflections or refractions of wave in layer interfaces, the different modes of propagation at a given frequency are reasonable and a result of constructive interference occurring among waves.

Two tasks are involved for the solution of Rayleigh eigenvalue problem. The first is the construction of the Rayleigh dispersion equation  $F_R[*] = 0$  (also called Rayleigh secular

function). The second is the computation of the roots as a function of frequency, which is to find the Rayleigh eigenvalue  $k_j=k_j(\omega)$ , as illustrated in Fig. 2-9. Once the roots are obtained, it is straightforward to compute the Rayleigh eigenfunctions  $r_j(k_j,z,\omega)$  for understanding the depth-dependence of displacement and stress as illustrated in Fig. 2-10.

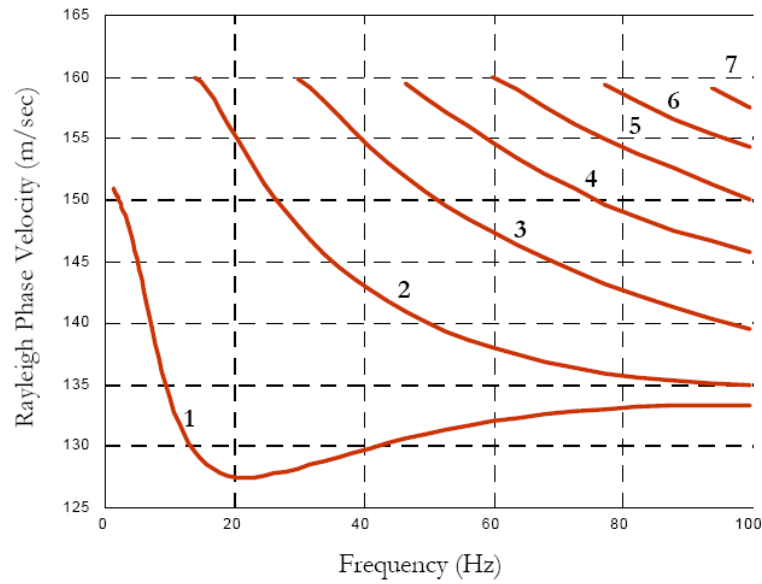


Fig. 2-9 Rayleigh waves dispersion curves in vertically heterogeneous media  
(Lai et al, 1998)

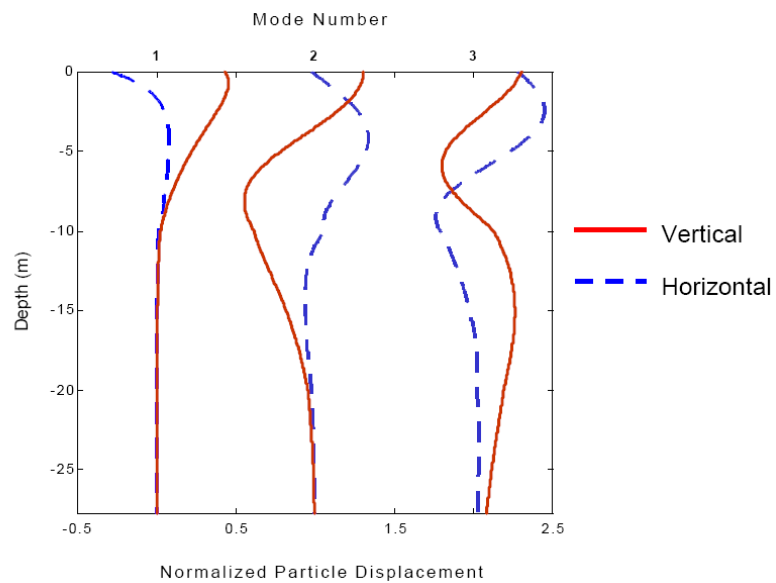


Fig. 2-10 Rayleigh displacement eigenfunctions in vertically heterogeneous media  
(Lai et al, 1998)

As shown in Fig. 2-9. The higher mode of propagation is characterized by higher velocity when several modes at a given frequency occur. Each mode of propagation holds a lower bound of frequency called the cut-off frequency,  $\omega_{cn}$ . The cut-off frequency is a function of stiffness and thickness of layers. The  $n^{\text{th}}$  mode will not exist unless the frequency of propagation  $\omega$  larger than its  $\omega_{cn}$ . Another important feature is that modes become more closely spaced as frequency increase. All modes tend to a lower bound of phase velocity which is the phase velocity of the thin layer bordering the free surface of a vertically heterogeneous halfspace. In a vertically heterogeneous media, the Rayleigh displacement eigenfunction is shown in Fig. 2-10.

The wave components with lower frequencies (larger wavelengths) induce the particles motion in larger depth as shown in Fig. 2-11(a). It implies the wavelength has a close relation with the investigated depth. The dispersion curve in the wavelength- velocity ( $\lambda$ - $v$ ) domain is analogous to the depth-velocity profile. Three typical cases of strata are discussed in literature: (1) The homogeneous half space: the shear wave velocity is not dispersive, as shown in Fig. 2-11(b). (2) The normally dispersive case: the shear wave velocity increases with depth and the fundamental mode of propagation is usually dominant, as shown in Fig. 2-11(c). (3) The irregularly dispersive case: the shear wave velocity does not increase with depth regularly and the higher mode of propagation may dominate in some frequencies, as shown in Fig. 2-11(d).

There are several methods for solutions of (2-48) including numerical integration, finite difference, finite element, boundary element and propagation matrix method (Lai et al, 1998). The propagation matrix method is commonly applied due to satisfying the hypothesis of horizontal layered strata and conceptual simplicity. Applying the method for solutions of (2-48) is first presented by Thomson in 1950 and modified by Haskell in 1953. The dispersion equation is constructed by a sequence of matrix multiplication involving terms of transcendental functions of material properties of layers in stratified halfspace. The Thomson-

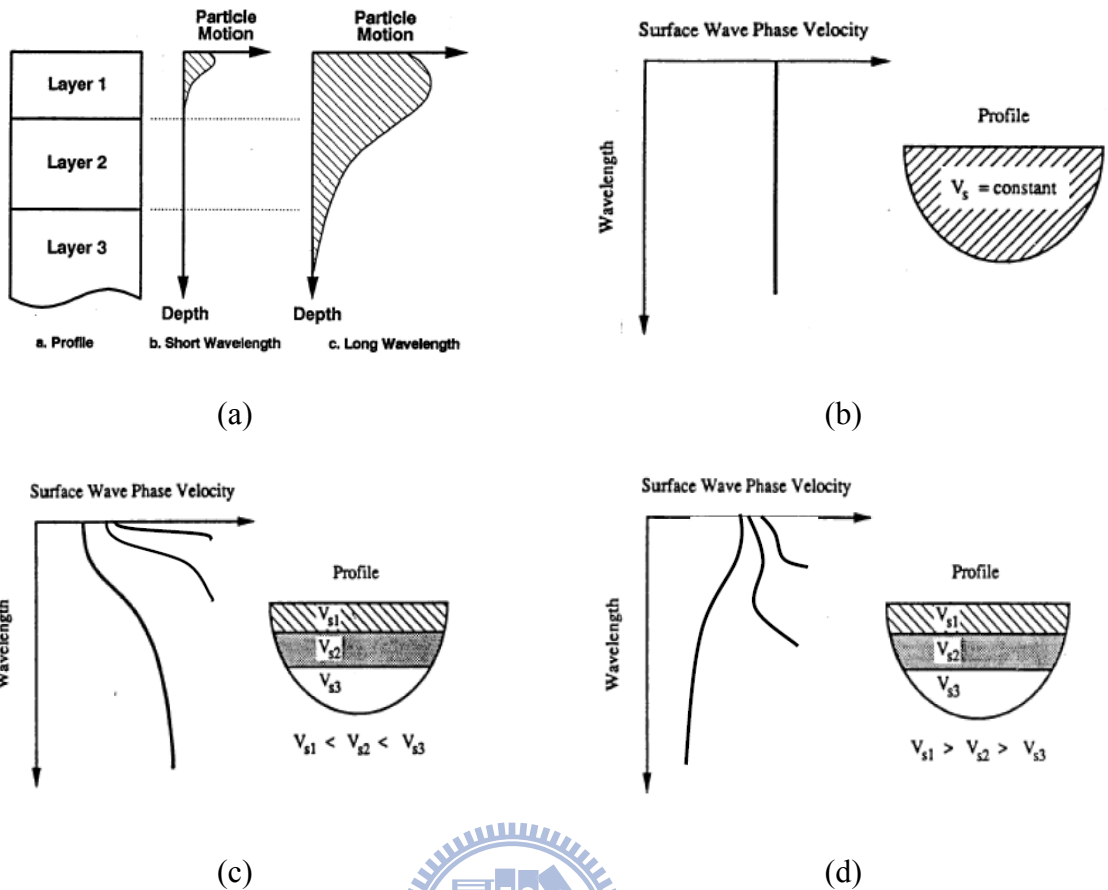


Fig. 2-11 Typical dispersion curves of different type of strata

(a) The relationships between wavelength, depth and particle motion (b) Dispersion curve of a homogeneous half space (c) Dispersion curve of a normally dispersive strata (d) Dispersion curve of an irregularly dispersive strata

Haskell algorithm suffers numerical instability problems at high frequency (Knopoff, 1964) and has been modified and improved by numerous researchers (Gilbert et al, 1966; Schwab et al, 1970; Abo-Zena, 1979; Harvey, 1981).

The finite element method for solving wave propagation problems in seismology was applied since early 70's. Dynamic stiffness matrix method is derived from Thomson- Haskell algorithm via finite element formulation (Kausel et al, 1981). The main part of this method is to replace the transfer matrices with layer stiffness matrices which are similar to stiffness matrices used in conventional structural analysis. The ability to use techniques in structural analysis like condensation and substructuring is an advantage for solving elastodynamic

problem of layered medium (Lai et al, 1998).

Method of reflection and transmission coefficients (Kennet, 1974) is another important one for solving eigenvalue problems of surface wave. Like Thomson- Haskell algorithm, the method is only suitable for multi-layered medium. Based on the use of reflection and transmission coefficients, the reflection and transmission matrices for a stratified medium is constructed for modeling the constructive interference leading to formation of different modes of surface waves (Kennet, 1983).

### **2.2.3 Computation of synthetic wavefield**

Analytical and numerical approaches are the two divisions of methods for synthetic seismic wavefields. Complicated attributes of inhomogeneous distribution in earth often make analytical simulations of seismic studies under the hypothesis of horizontal layered strata. For laterally heterogeneous problems, to obtain the general analytical solution is difficult and numerical methods seem a better approach in this aspect.

#### **2.2.3.1 Analytic approach**

The first analytic approach for synthetic seismic wavefield was presented by Lamb in 1904, in which he analyzed the displacement of the wavefield in an isotropic and homogeneous stratum caused by an impulsive point source. This synthetic wavefield includes all effect from body waves and Rayleigh wave. But the results were not precise when compared with actual seismic records.

Since then, more applicable analytical approaches have been developed and can be grouped into five categories:

1. Generalized ray theory (Helmberger, 1968; Muller, 1969; Ben-Menahem and Vered, 1973)

2. Full-wave theory (Comier and Richards, 1977; Choy, 1977)
3. WKBJ theory (Chapman, 1978)
4. Wavenumber or slowness integration (Kind,1978; Cormier, 1980; Wang and Herrmann, 1980; Ingate et al, 1983; Ha,1984 )
5. Modal summation (Takeuchi and Saito, 1972; Harvey, 1981; Panza, 1985)

Mathematical transformations, usually Fourier Transform or Hankel transform, are involved in above methods. Seismologists usually process the displacement functions in frequency-slowness domain rather than in space-time domain. For stratified media, the main differences between methods are the ways to find the governing equation in frequency-slowness domain and to process the transforms between different domains. The displacement function in space-time domain can be obtained by integrating its transform in frequency-slowness domain. Therefore the routes and hypotheses of integrations will affect the scope of applications of those analytic methods.

The synthetic wavefields and dispersion relationships of strata used in this study are generated by a set of computer programs released by Professor R.B. Herrmann and his research team at Saint Louis University, USA. The dispersion relationships form the eigenvalue problems of Rayleigh wave is solved by delta matrix method (Dunkin, 1965). The synthetic wavefields is created by modal summation of surface waves and the effects from body waves are exclusive.

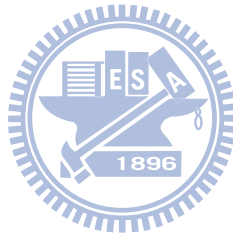
### **2.2.3.2 Numerical approach**

Numerical simulations on seismic data are now broadly applied to interpretations of earthquakes data, signal processing and parametric studies of seismic tests, and researches on seismic wave behaviors in an anisotropic and inhomogeneous medium. Several kinds of numerical method are available:



1. Finite differences method (Alterman and Karal, 1968 ; Boore, 1972 ; Kelly et al., 1976 ; Virieux, 1986 ; Levander, 1988 ; Takeuchi and Geller, 2000 ; Zhang, 2004)
2. Finite element method (Lysmer and Drake, 1972 ; Schlue, 1979 ; Chen, 1984 ; Kay and Krebes, 1999)
3. Pseudo-spectral method (Gazdag, 1973 ; Kosloff and Baysal, 1982 ; Johnson, 1984 ; Reshef et al., 1988a, 1988b ; Huang and Yeh, 1991)
4. Hybrid method (Shtivelman, 1985 ; Kummer, Behle & Dorau, 1987 ; Ven den Burg, 1984 ; Emmerich, 1992 ; Moczo et al., 1997)

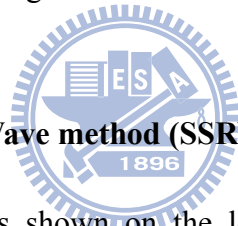
This study mainly deals with horizontal layered media which can be more effectively simulated by analytic approaches.



## 2.3 Seismic tests using surface wave

### 2.3.1 Overview of surface wave methods

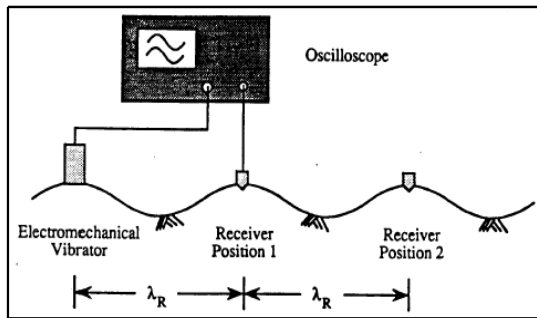
Application of surface testing to geotechnical site characterization started at the end of 1950s in the Steady State Rayleigh Wave method (SSRW) with single-station recording. Successively the Spectral Analysis of Surface Waves Method (SASW) using two-station data recording was introduced during the 1980s. Meanwhile geophysicists also consider the surface waves as a potential tool for underground explorations in which they utilized multi-station data. The application of surface wave method for site investigation becomes more and more popular in practices due to its non-intrusive feature and convenient operation. In particular, Multi-station Analysis of Surface Waves method (MASW) permits a single survey of a broad depth range and high levels of redundancy with a single field configuration.



#### 2.3.1.1 Steady State Rayleigh Wave method (SSRW)

The field setup of SSRW is shown on the left part of Fig. 2-12. A vertical acting sinusoidal vibrator, vibrating at a given frequency, is placed on the surface and one vertical receiver also placed on the ground is used to detect the ground motion. The receiver is moved away from the source until both the source and receiver are in phase. The distance between the two adjacent in-phase recordings is assumed to be the wavelength at the particular frequency. For every frequency, the slope of the relationship between the source-to-receiver offset and corresponding numbers of wave can be used to determine the wavelength or velocity of Rayleigh waves. The stiffness profile can then be inverted by using the measured dispersion curve (frequency versus wavelength or frequency versus velocity).

Seismic energy of Rayleigh waves concentrate mostly in the shallow depth. The influenced depth is about 1.0 to 1.5 times the wavelength. The relationship between Rayleigh



$\lambda_R$  is found moving the receiver  
(the receiver and the source are in phase)

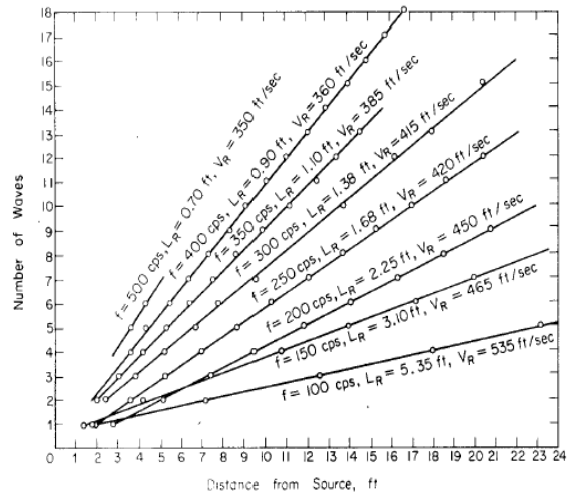


Fig. 2-12 Steady State Rayleigh Wave (SSRW) method: field procedure  
(Rix, 1988)

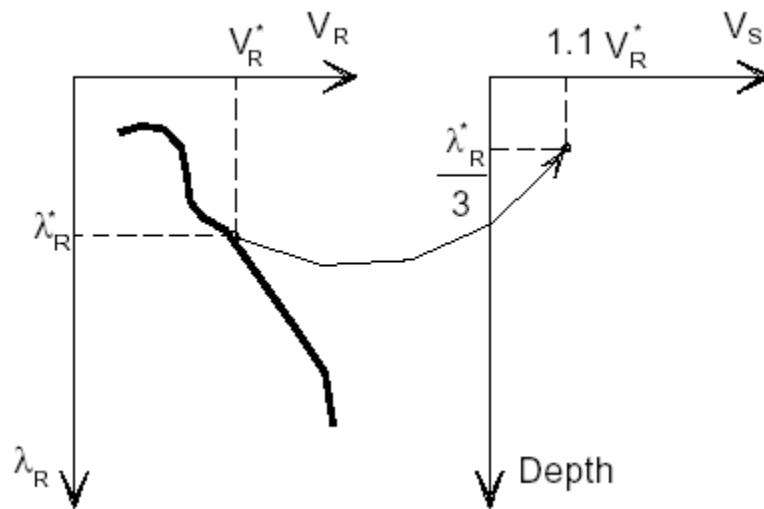


Fig. 2-13 Simplified inversion process proposed for the SSRM  
(Foti, 2000)

wave velocity and shear waves could be roughly expressed as: (Richart, 1962)

$$0.87 < \frac{v_R}{v_S} < 0.96 \tag{2-52}$$

$$v_S \approx 1.1v_R \tag{2-53}$$

When SSRW was developing, a simple approximate inversion process was done by

direct mapping from the  $v_R-\lambda_R$  domain to  $v_S-z$  domain, as illustrated in Fig. 2-13. The simple inversion may work reasonably well in a normal condition in which  $v_S$  increases by depth. But for the stratum with a stiff layer over soft layers, the simple inversion may produce serious errors. More rigorous inversion will be discussed in Sec. 2.3.4. The SSRW test is quite time-consuming because it needs to keep conducting the same procedures for each different frequency and adjusting the spacing of receivers until the source and receiver is are phase.

### 2.3.1.2 Spectral Analysis of Surface Waves method (SASW)

The SASW takes advantage of the availability of two-channel signal analyzer to improve testing efficiency. It was developed in the context of geotechnical applications (Nazarian and Stoke, 1986; Nazarian et al, 1983; Nazarian and Stoke, 1985).

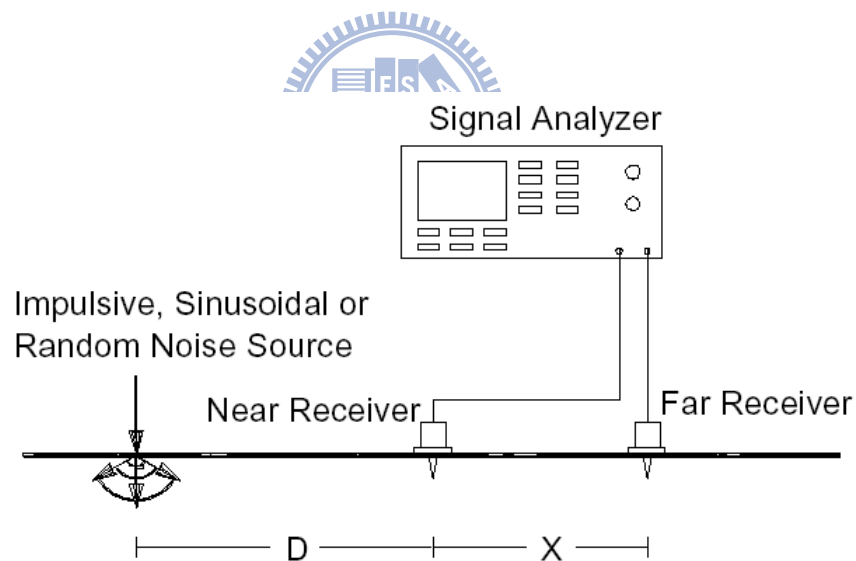


Fig. 2-14 SASW method field configuration

(Foti, 2000)

The test is performed typically using a vertical impulse applied to the ground surface and recording the transient signal composed mainly of Rayleigh waves over a certain frequency range, by means of two receivers placed along a straight line passing through the impulse point as shown in Fig. 2-14. The distance between the source and first receiver is usually set

equal to that between two receivers. To avoid the near field effect, several tests are conducted with various sources-to-receiver and receiver-to-receiver distance.

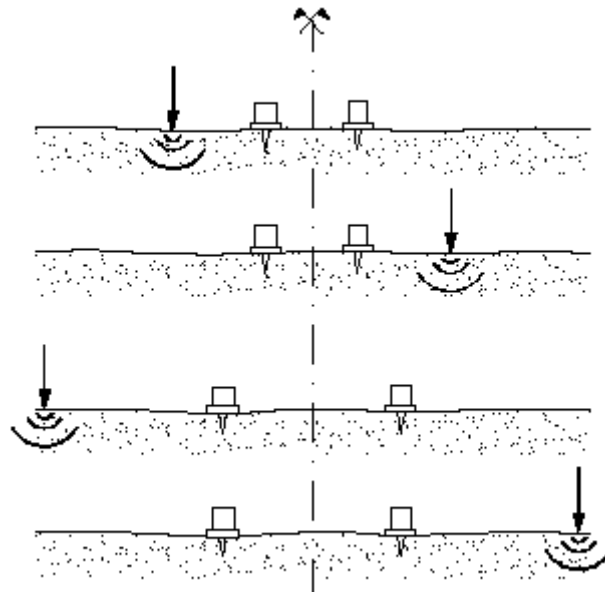


Fig. 2-15 Common receiver midpoint array with source position reversing

(Foti, 2000)

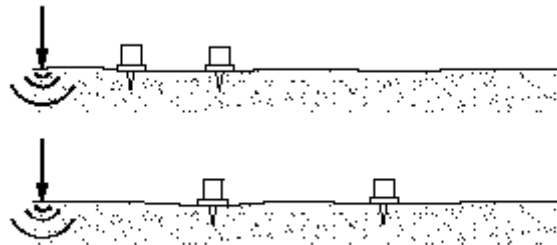


Fig. 2-16 Common source array

(Foti, 2000)

Two different testing schemes have been used

1. Common receiver midpoint array as shown in Fig. 2-15
2. Common source array as shown in Fig. 2-16

Surface waves in a typical SASW test are generated by an impact source, detected by a pair of geophones, and recorded on an appropriate recording device. The signals are recorded for several shots to evaluate the signal-to-noise ratio (or data coherence). The difference

between the difference of phase angles of the two signals ( $\Delta\phi = \phi_2 - \phi_1$ ) is equal to the phase angle of the average cross-spectral density  $CSD(u_1, u_2)$ :

$$\Delta\phi(\omega) = \phi_2(\omega) - \phi_1(\omega) = \text{Angle}[CSD(u_1(t), u_2(t))] \quad (2-54)$$

where  $\phi_2(\omega)$  and  $\phi_1(\omega)$  are the phase angles of  $u_2$  and  $u_1$  respectively as a function of angular frequency  $\omega$ . For the assessment of signal quality, the coherence function,  $r^2(\omega)$ , is defined to measure the linearly correlated degree between two signals:

$$r^2(\omega) = \frac{G_{12}(\omega) \cdot G_{12}^*(\omega)}{G_{11}(\omega) \cdot G_{22}(\omega)} \quad (2-55)$$

where  $G_{12}$  is the cross power spectrum of  $u_1$  and  $u_2$ ,  $G_{12}^*$  is the complex conjugate of  $G_{12}$ ,  $G_{11}$  and  $G_{22}$  are the auto power spectra of  $u_1$  and  $u_2$  respectively.

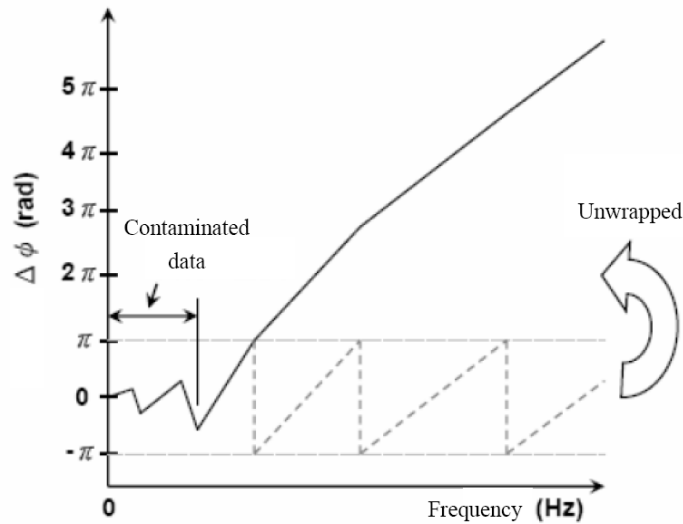


Fig. 2-17 SASW signal processing-  $\Delta\phi$  vs Frequency

Following (2-54), the apparent phase velocities of different frequencies can be determined as

$$v_a(\omega) = \frac{\omega}{\frac{\Delta\phi(\omega)}{\Delta x}} \quad (2-56)$$

where  $\Delta x$  is the geophone spacing. The actual phase difference  $\Delta\phi(\omega)$  increases with

frequency. But the angle of the cross-spectral density oscillates between  $-\pi$  and  $\pi$  by definition. Thus, the angle of cross-power spectrum has to be un-wrapped before applying it to (2-56) as shown in Fig. 2-17.

There are some drawbacks of SASW. This un-wrapping process is often a ticklish task. The correctness of un-wrapping at high frequencies relies on that at low frequencies. The energy generated by an impact source is band-limited, with low signal-to-noise ratio at very low and high frequencies. Geophones act as high-pass filters that damp the low-frequency components below the natural frequency of the geophones. Therefore, the signal-to-noise ratio of the signals is low below a particular frequency depending on the source and receiver characteristics. Consequently, un-wrapping may be erroneous, especially for large geophone spacing since larger geophone spacing implies greater number of cycles in the phase spectrum. Removing of these un-wrapping errors is time consuming and depends on the analyst's judgment and experience. The natural frequency of geophones used for typical refraction survey is equal to or greater than 4.5 Hz, hence not suitable for SASW test. Wave Form analyzer rather than typical seismograph is preferred because it has built-in spectral functions necessary for instantaneous inspection of the recorded data.

It has been shown that errors may arise in experimental dispersion curves when usual SASW test and data analysis procedures are followed, in particular the phase unwrapping procedure. Sources that contain significant energy in very low frequencies and receivers with very low natural frequency are necessary to avoid erroneous un-wrapping of phase angles at low frequencies. Hence, the data acquisition system of a SASW test is typically different from that of a refraction survey although they share many things in common. Unwrapping errors may occur for sites where, across the frequency range used, there is a shift from one dominant surface wave propagation mode to another, a phenomenon termed 'mode jumping'. Furthermore, the use of only a pair of receivers leads to the necessity of performing the test

using several testing configuration and the so-called common receiver midpoint geometry. For each receiver spacing, multiple measurements are necessary for evaluating the data coherence. This results in a quite time-consuming procedure on site for the collection of all the necessary data and on data reduction for combining the dispersion data points from records obtained at all spacings. Since many non-trivial choices need to be made based on the data quality and testing configuration, the test requires the expertise of an operator and automation of the data reduction is difficult.

### 2.3.1.3 Multi-channel Analysis of Surface Waves method (MASW)

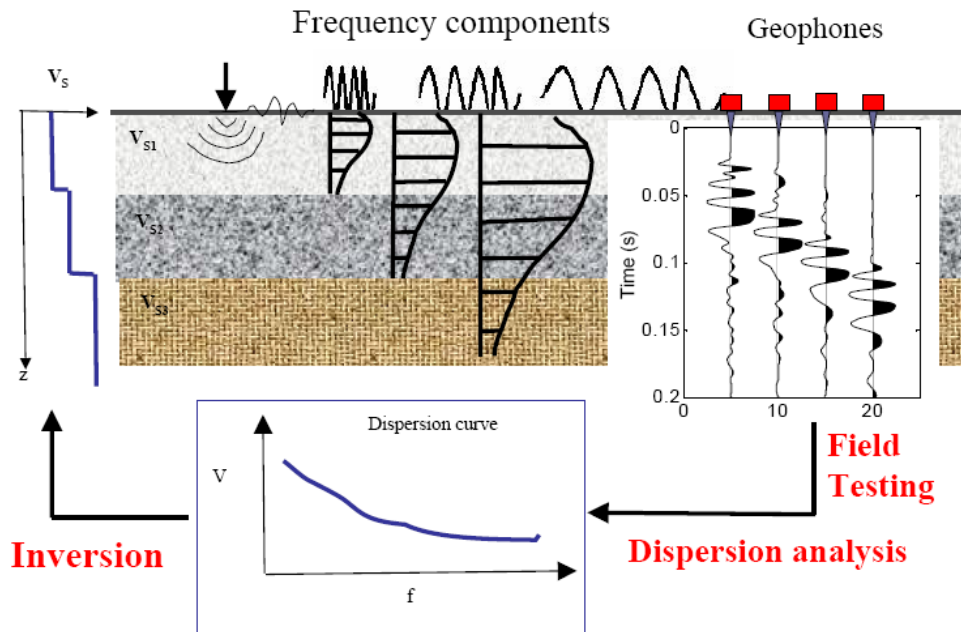


Fig. 2-18 Scheme of MASW

Thanks to advancement in electronics, multi-channel seismographs are widely available. Surface wave studies using multi-channel records have been carried out by controlled sources (Gabriel et al, 1987; McMechan et al, 1981) and earthquake as a source (Nolet et al, 1976). The integration of multi-channel processing techniques in geophysics with smaller geotechnical engineering surveys has lead to the development of a new surveying technique,



called multi-channel analysis of surface waves (MASW) at the Kansas Geological Survey (Park et al, 1999; Xia et al, 2002). Methods based on multi-station data and wavefield transform are recently reported to possess several advantages for dispersion curve analysis (Park et al, 1999; Xia et al, 2002; Lin et al, 2002; Foti et al, 2002). Multi-station recording permits a single survey of a broad depth range, high levels of redundancy with a single field configuration, and the ability to adjust the offset, effectively reducing near field and far field effects.

As mentioned earlier, MASW, like other surface wave methods, involves three major steps: (1) Generating artificial perturbations on tested sites and recording the seismograms via sensors (Geophones) and a seismograph. (2) Determination of the experimental dispersion curve with signal processing procedures from the collected field seismograms. (3) Determination of the stiffness profile with an inversion process. A brief scheme of MASW is shown in Fig. 2-18. Detailed illustrations for field test configuration, extracting dispersion curves from Multi-channel seismic records and inversion process will be introduced in the following.

### **2.3.2 Field testing procedure of MASW**

The field test configuration of MASW is shown in Fig. 2-19. An array of receivers (geophones) is placed on the ground surface of a planed survey line. The impulsive or harmonic source is located on the extended direction of the survey line with an appropriate distance. At the time that the impulsive or harmonic loading applied, the seismograph is triggered simultaneously and start to record vertical motions (in displacement, velocity or accelerations) of the 2-D (time-space) wavefield. The acquired wavefield is discretized and truncated in both the time and space domains. Several acquisition parameters are involved. The temporal parameters include the sampling interval,  $\Delta t$ , and total sampling duration,  $T$ ; the

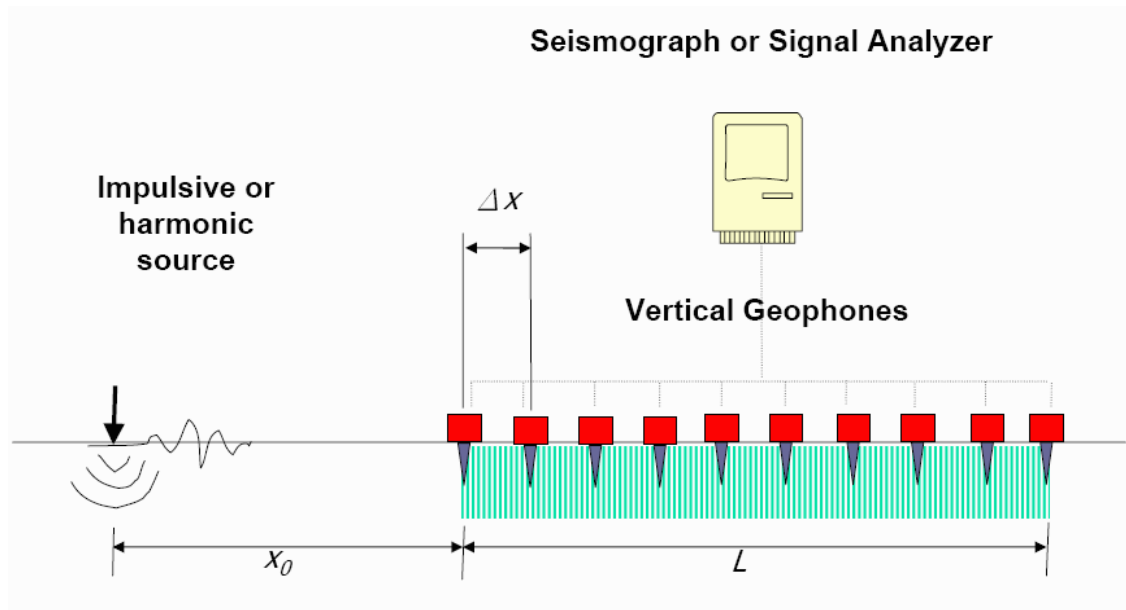


Fig. 2-19 Field test configuration of MASW

spatial parameters include the geophone spacing,  $\Delta x$ , the geophone spreading,  $L$  and near offset (distance from source to the nearest offset),  $X_0$ . Testing parameters need to be appropriately chosen considering aliasing phenomenon (due to discretization), leakage (due to truncation), and near and far field effects. Detailed discussions on this issue will be introduced in Chapter 3.

### 2.3.3 Dispersion analysis of MASW

Three common algorithms are applied for extracting the dispersion relationship from multi-stations seismic records. They are (1) frequency-wavenumber,  $f-k$ , transformation (Capon, 1969; Yilmaz, 1987; Alleyne et al, 1990; Forchap et al, 1998; Lin et al, 2003; Lu et al, 2004) (2) frequency- slowness,  $f-p$ , transformation (McMechan et al, 1981) (3) Phase shift method (Park et al, 1998b). These methods are reviewed as follows.

### 2.3.3.1 *f-k* transformation

Due to the frequency-dependant characteristic, geophysicists always need to map data from time domain to frequency domain. The Discrete Fourier Transform (DFT) is the common one used for any sequential series. For a discrete 2-D wavefield collected in the field,  $u(t_m, x_n)$  with  $m$  samples in time domain and  $n$  samples in space domain, the algorithm starts with a DFT and its DFT spectra at multiple stations is,

$$U(f_i, x_n) = \frac{1}{M} \sum_{m=0}^{M-1} u(t_m, x_n) \exp(-j2\pi f_i t_m) \quad (2-57)$$

where  $u$  is the velocity or acceleration measured by the receiver,  $U$  is the DFT of  $u$ ,  $j = \sqrt{-1}$ ,  $t_m = m\Delta t$ ,  $f_i = i\Delta f = i/[(M-1)\Delta t]$ , and  $x_n = n\Delta x$ . The  $i$ ,  $n$ , and  $m$  in (2-56) are integer indices to represent respectively discrete points in the frequency, space, and time domain.

For each frequency component, the wavefield is a harmonic function of space. The wavenumber  $k$  (i.e. spatial frequency) can be determined from the wavenumber analysis (spectral analysis in space). The wavenumber analysis of the multi-station signals can be performed using the discrete-space Fourier Transform (Lin et al, 2003):

$$Y(f_i, k) = \sum_{n=0}^{N-1} U(f_i, x_n) \exp(-j2\pi k x_n) \quad (2-58)$$

where  $Y(f_i, k)$  represents the wavefield in the frequency-wavenumber domain, as shown in Fig. 2-20.

Obviously the number of stations is much less than the number of samples in the time domain. Hence the aliasing problem in space domain is the first great concern when *f-k* transformation applied. Besides the adjustment of spatial testing parameters, focusing on the aspect of signal processing, the common way for enhancing the resolution in space domain is to add zero-value traces after the raw data. However the algorithm presented here (Lin et al, 2003) applies the discrete-space Fourier Transform in space domain.

The discrete-space Fourier Transform is different from the discrete Fourier Transform in that the wavenumber remains continuous but the fast algorithm (FFT) cannot be used. Due to deficiency of space sampling, the discrete-space Fourier Transform rather than discrete Fourier Transform is used in the space domain, such that the resolution in the wavenumber domain can be arbitrarily chosen. The wavenumber ( $k$ ) of the surface wave can be identified at the peaks of the amplitude spectrum of  $Y(f_i, k)$ . The phase velocity is then determined by the definition  $v = 2\pi f/k$ . An example of  $f$ - $k$  transformation is shown in Fig. 2-20.

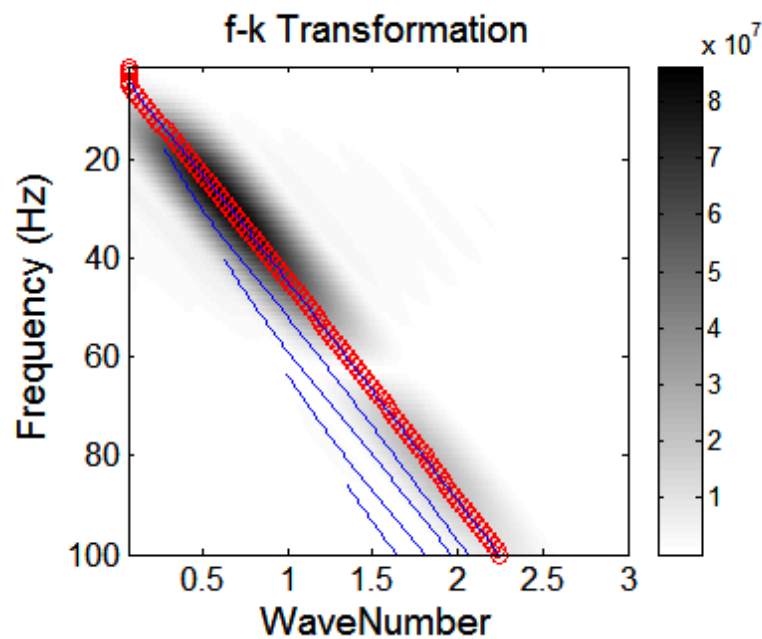


Fig. 2-20 An example of  $f$ - $k$  transformation

### 2.3.3.2 $p$ - $f$ transformation

The  $f$ - $p$  transform is equivalent to a plane-wave decomposition of the wavefield, where  $p$  is the horizontal slowness (i.e. the inverse of velocity) and the intercept  $\tau$  is a transformed time (linearly moved out). The transform is often called Slant-Stack because considering a wavefield the basic operation is that of stacking all values along each inclined (slant) line (Robinson, 1982). The sum of all the values along the line is then associated to a point in the

new domain having as coordinates the slope  $p_0$  and intercept  $\tau_0$  of the line as shown on Fig. 2-21 (Foti, 2000).

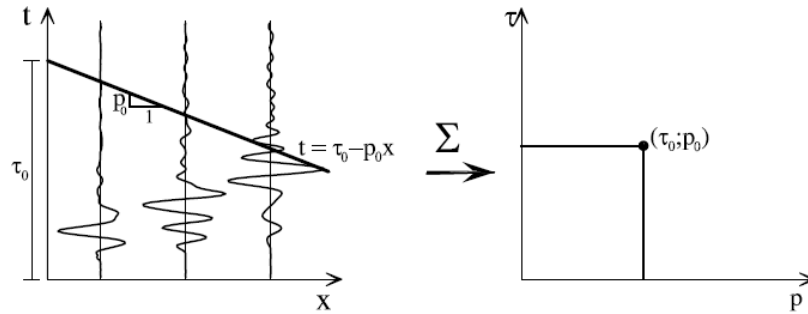


Fig. 2-21 Exemplification of the Slant-Stack transform concept

(Foti, 2000)

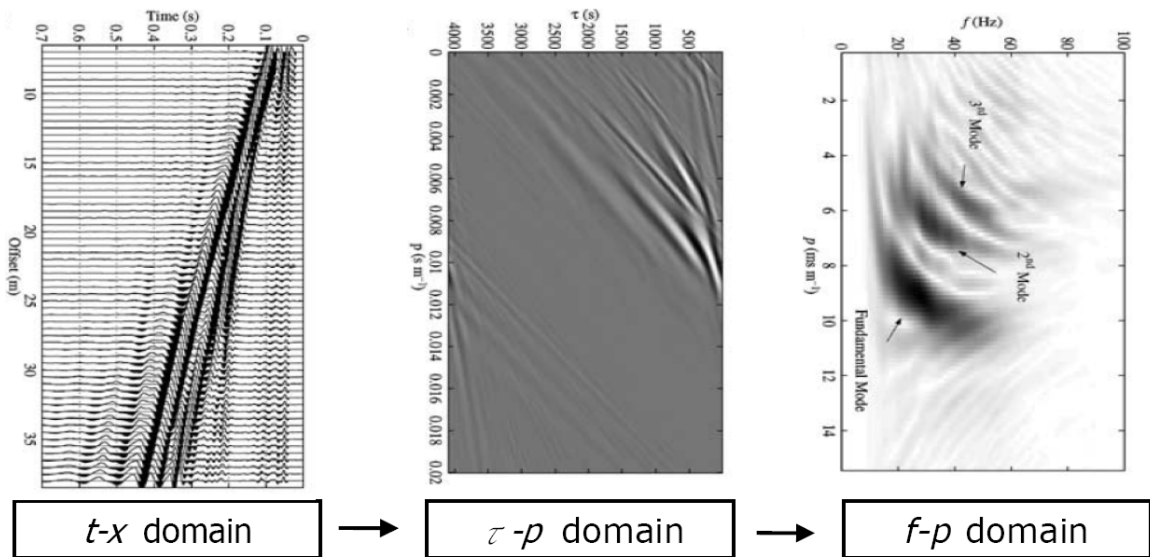


Fig. 2-22 An example of  $p$ - $f$  transformation

(Beatty et al, 2003)

For a recorded wavefield,  $u(x_i, t)$ , the slant-stack transform, as shown in Fig. 2-22, is given in the following expression: (Beatty, 2000; Forbriger, 2003)

$$U(p, \tau) = \sum_{i=1}^N u(t = \tau + px_i, x_i) \quad (2-59)$$

where  $\tau$  is an intercept time,  $p=1/v$  is slowness or the inverse of velocity,  $x_i$  is the offset value

for the channel  $i$  and  $N$  is the number of the seismic channels used in the  $\tau$ - $p$  domain.

If the seismic signal  $u(t, x_i)$  is written as a Fourier integral:

$$u(t, x_i) = \int_{-\infty}^{+\infty} \tilde{u}(\omega, x_i) e^{-i\omega t} \frac{d\omega}{2\pi} \quad (2-60)$$

The slant stack becomes:

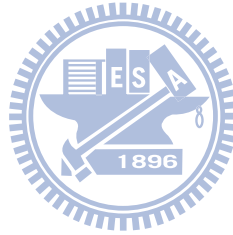
$$U(\tau, p) = \sum_{i=1}^N \int_{-\infty}^{+\infty} \tilde{u}(\omega, x_i) e^{-i\omega p x_i} e^{-i\omega \tau} \frac{d\omega}{2\pi} \quad (2-61)$$

From (2-61) the Fourier coefficients of the slant stack:

$$\tilde{U}(\omega, p) = \sum_{i=1}^N \tilde{u}(\omega, x_i) e^{-i\omega p x_i} \quad (2-62)$$

To gain full resolution it is best to normalize the signal energy to the offset dependence of plane wave in elastic media which is (Forbriger, 2003):

$$\int_0^{+\infty} u^2(t, x) dt = \text{constant} \quad (2-63)$$



Then (2-64) becomes:

$$G^{SLS}(\omega, p) = \sum_{i=1}^N f_i \tilde{u}(\omega, x_i) e^{-i\omega p x_i} \quad (2-64)$$

$f_i$  are appropriate factor to scale the seismogram to match (2-63). Substantial components of the seismic wavefield that travel with phase slowness  $p$  at an angular frequency  $\omega$  will produce an amplitude maximum of  $G^{SLS}$  at  $(\omega, p)$ . The dispersion relation  $p(\omega)$  of the surface wave will become apparent from these maxima. An example of  $p$ - $f$  transformation is shown in Fig. 2-22.

### 2.3.3.3 Phase shift method

A phase shift method, as shown in Fig. 2-23, was presented by Park et al (1998). A wavefield in time-space domain is represented as  $u(x, t)$ . Applying the Fourier Transform with

respect to time gives,

$$U(x, \omega) = \int u(x, t) e^{i\omega t} dt \quad (2-65)$$

$U(x, \omega)$  can be expressed as the multiplication of two separate terms:

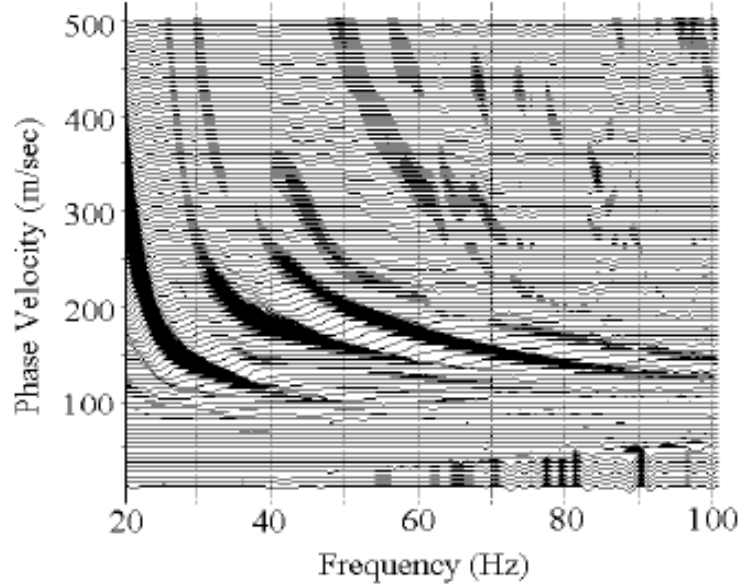
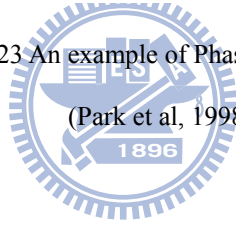


Fig. 2-23 An example of Phase shift method

(Park et al, 1998)



$$U(x, \omega) = P(x, \omega) A(x, \omega) \quad (2-66)$$

where  $P(x, \omega)$  and  $A(x, \omega)$  are phase and amplitude spectrum respectively.  $P(x, \omega)$  contains all the information about dispersion properties and  $A(x, \omega)$  contains the information about all other properties such as attenuation and spherical divergence. Therefore,  $U(x, \omega)$  can be expressed as follows:

$$U(x, \omega) = e^{-i\Phi x} A(x, \omega) \quad (2-67)$$

where  $\Phi = \omega/c_\omega$ ,  $\omega =$  frequency in radian, and  $c_\omega =$  phase velocity for frequency  $\omega$ .

Applying the following integral transformation to  $U(x, \omega)$  in (2-67) we obtain  $V(\omega, \phi)$ :

$$V(\omega, \phi) = \int e^{-i\phi x} \left[ \frac{U(x, \omega)}{|U(x, \omega)|} \right] dx = \int e^{-i(\Phi - \phi)x} \left[ \frac{A(x, \omega)}{|A(x, \omega)|} \right] dx \quad (2-68)$$

The integral transformation in (2-68) can be thought of as the summing over offset of

wavefields of a frequency after applying offset-dependent phase shift determined for an assumed phase velocity  $c_\omega (= \omega/\varphi)$  to the wavefields in (2-67). This process is identical to applying a slant stack to the equivalent time-domain expression of  $U(x,\omega)/|U(x,\omega)|$  for a single frequency. To insure equal weighting during analysis of wavefields from different offsets  $U(x,\omega)$  is normalized with respect to offset compensating for the effects of attenuation and spherical divergence. Therefore, for a given  $\omega$ ,  $V(\omega,\varphi)$  will have a maximum if

$$\Phi = \phi = \omega / C_\omega \quad (2-69)$$

Because  $A(x,\omega)$  is both real and positive. For a value of  $\varphi$  where a peak of  $V(\omega,\varphi)$  occurs, the phase velocity  $c_\omega$  can be determined. If higher modes get appreciable amount of energy, there will be more than one peak.

Dispersion curves result from transforming of  $V(\omega,\varphi)$  to obtain  $I(\omega,c_\omega)$  through changing the variables such that  $c_\omega = \omega/\varphi$ . In the  $I(\omega,c_\omega)$  wavefields, there will be peaks along the  $c_\omega$ -axis that satisfy (2-69) for a given  $\omega$ . The locus along these peaks over different values of  $\omega$  that permits the images of dispersion curves to be constructed (Park et al, 1998). An example of  $f$ - $v$  transformation is shown in Fig. 2-23.

### 2.3.4 Inversion for the stiffness profile

Direct inversion from dispersion curve to its unique stiffness profile is not available. Therefore, a typical inversion is an iterative process of theoretical dispersion modeling to fit the measured field dispersion. Therefore there are two main tasks in the inversion based on dispersion: dispersion modeling and optimization method.

Theoretical dispersion modeling has been introduced in previous sections. Inversion techniques aim to minimize an objective function the measure the misfit (e.g. RMS error) between the measured and forward modeled data. The local least-square methods are widely applied in geophysical problems. The modeled dispersion is compared to the measured



dispersion and model parameters adjusted by the assumption of local linearity to subsequently match the modeled and measured curve within a user-defined Root-Mean-Square (RMS) error. In most cases, the modeled parameters are confined to the layer thickness and shear wave velocity which provide the largest sensitivities. Newton-Gaussian framework can be used for

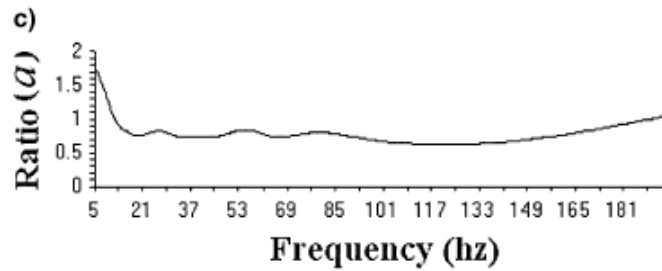


Fig. 2-24 Ratio  $a$  that was used during construction of the initial  $v_s$  profiles

(Park et al, 1999)

nonlinear optimization. But least-squares optimization has been the mainstay method of most researches as well as current available commercial systems.

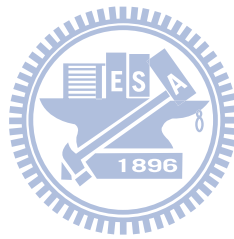
Global optimization methods are also available although less employed. Genetic algorithms are applied to upper crustal investigation via both Love (Yamanaka et al, 1997) and Rayleigh (Mackenzie et al, 2001) wave data as well as pavement evaluation via SASW (Hunaidi, 1998). Simulated annealing has also been successfully used in multi-mode MASW inversion (Beaty et al, 2002). By scanning a much broader model space, the global minimum is more likely to be found. The drawback is computational inefficiency due to hundreds or thousands of iterations required.

The  $v_s$  profiles are calculated using an iterative inversion procedure that requires the dispersion data and estimates of Poisson's ratio and density. An initial earth profile needs to be specified as a starting point for the iterative inversion process. The model consists of velocity (P-wave and S-wave velocity), density and thickness parameters. Among these four parameters,  $v_s$  has most significant effect on the reliable convergence of the algorithm (Park et

al, 1999). An initial  $v_s$  profile was proposed such that  $v_s$  at a depth  $z$  is 1.09 times (Stokoe et al, 1994) the measured phase velocity  $v_R$  at the frequency where wavelength  $\lambda_R$  satisfies the relationship,

$$z = a \cdot \lambda_R \quad (2-70)$$

where  $a$ , as shown in Fig. 2-24, is a coefficient that only slightly changes with frequency and is based on extensive modeling.



### **3 Investigation of field parameters and standardization of field testing**

Due to the strong energy carried by surface wave, the high signal-to-noise (S/N) ratio makes the MASW have a greater tolerance of selections on field parameters than other seismic methods using body waves. Discretization and truncation during MASW data acquisition may cause errors and ambiguities in dispersion analysis if field parameters are not selected carefully. However, tradeoffs are involved when selecting the configuration parameters (including temporal and spatial). Especially for inexperienced testers it could be a perplexity when conducting tests in the field. A standard and preferred guideline is proposed here for engineering practice.

As mentioned in previous sections, MASW surveys involve temporal and spatial parameters. The temporal parameters include the sampling intervals,  $\Delta t$ , and total sampling duration,  $T$ ; the spatial parameters include the geophone spacing,  $\Delta x$ , the geophone spread,  $L$ , and the near offset (the nearest source-to-receiver offset),  $X_0$ . The effects of those field parameters will be investigated first. The dilemma of selecting the field parameters and its countermeasures will be then presented.

### 3.1 Temporal parameters of field testing

#### 3.1.1 Aliasing due to time domain discretization: the sampling interval, $\Delta t$

Aliasing in signal processing is referred as an effect that causes different continuous if different frequencies signals indistinguishable after discrete sampling. As shown in Fig. 3-1, two different continuous signals can be reconstructed from the same set of samples.

The frequency aliasing can be avoided by using a sufficiently small  $\Delta t$  or the anti-aliasing filter in the data acquisition system such that

$$\Delta t \leq \frac{1}{2f_{\max}} \quad (3-1)$$

where  $f_{\max}$  is the maximum attainable frequency of the signal.



Fig. 3-1 Two different signal fitting the same set of samples

#### 3.1.2 Leakage due to time domain truncation: total sampling duration, $T$

The leakage in the frequency domain does not occur when  $T$  is greater than the maximum duration of the transient signals incurred by an impact source. For stationary harmonic signals, the leakage in the frequency domain is lessened to an acceptable level by using a time window  $T$  greater than the maximum period of the signals such that

$$T = (M - 1)\Delta t \geq \frac{1}{f_{\min}} \quad (3-2)$$

where  $f_{\min}$  is the lowest frequency of the signal and  $M$  is the number of sampling in the time domain. Most modern data acquisition systems have small enough  $\Delta t$  and large enough  $M$  to avoid problems related to frequency aliasing and leakage.

## 3.2 Spatial parameters of field testing

### 3.2.1 Aliasing due to space domain discretization: the geophone spacing, $\Delta x$

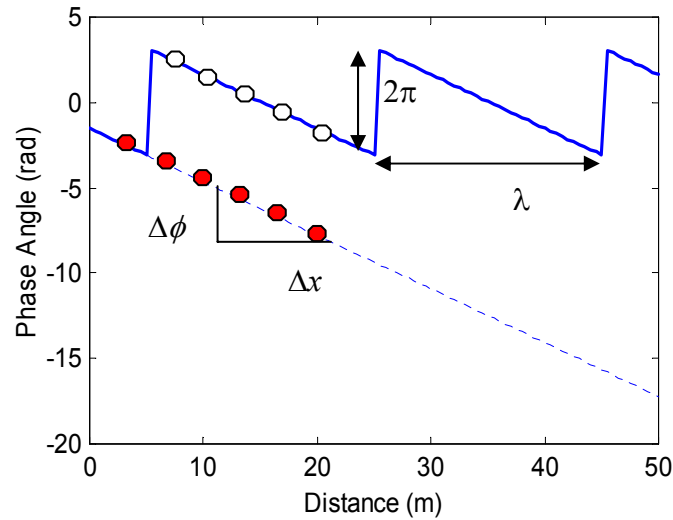
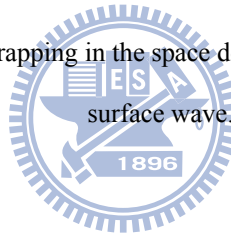


Fig. 3-2 An illustration of phase un-wrapping in the space domain for the multi-station spectral analysis of surface wave.



Following the concept of dispersion analysis of MSASW and f-k transformation, the discrete Fourier Transform of the wavefield  $u(t_m, x_n)$  with respect to time ( $t_m$ ) produces  $U(f_i, x_n)$  (given in (2-56)) with a modulo- $2\pi$  representation in the phase spectrum. In the MSASW approach, the phase angle can be unwrapped in the space domain since it monotonically increases with the source- to- receiver offset  $x$ , as shown in Fig. 3-2. In order to correctly unwrapping the phase angles in the space domain, the following criterion should be satisfied

$$\Delta x < \frac{\lambda_{\min}}{2} \quad (3-3)$$

where  $\lambda_{\min}$  is the shortest wavelength of interest.

A simple example is used here to illustrate the validity of (3-3). Two synthetic recording wavefields including several superposed modes of vibrations, as listed in Table 3.1 , were

Table 3.1 Modes used to generate synthetic wavefields using modal superposition

(equal weights of each mode are used)

| mode | f (Hz) | v (m/sec) | k (rad/m) | $\lambda$ (m) | p (sec/m) |
|------|--------|-----------|-----------|---------------|-----------|
| 1    | 10     | 500       | 0.1257    | 50.00         | 0.0020    |
| 2    | 10     | 400       | 0.1571    | 40.00         | 0.0025    |
| 3    | 20     | 300       | 0.4189    | 15.00         | 0.0033    |
| 4    | 20     | 350       | 0.3590    | 17.50         | 0.0029    |
| 5    | 30     | 300       | 0.6283    | 10.00         | 0.0033    |

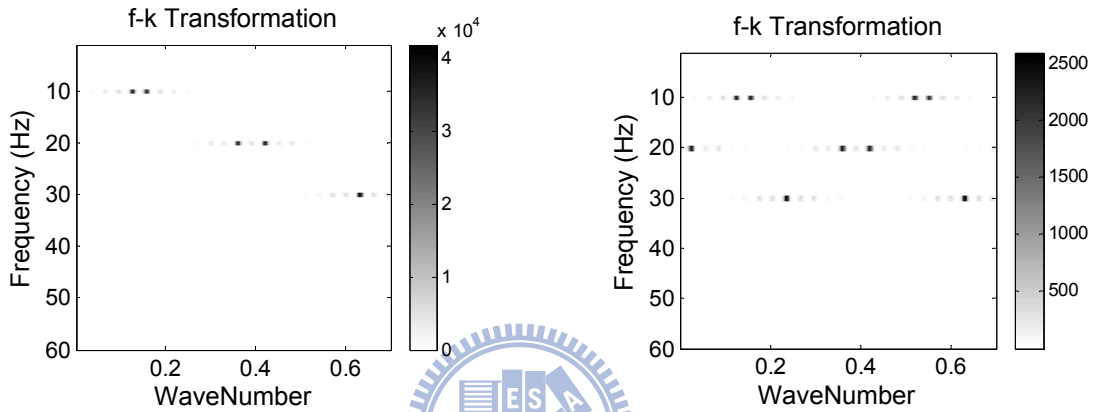


Fig. 3-3 The geophone spacing  $\Delta x$  influence on aliasing problem

The  $f$ - $k$  spectra of the synthetic wavefields (Left:  $\Delta x=1$ m; Right:  $\Delta x=16$ m)

generated for signal analysis. The recording parameters ( $\Delta t=0.005$  sec,  $M=2048$  and  $L=1024$  m) are the same except for the geophone spacing  $\Delta x$  (one signal with  $\Delta x=1$  m; another with  $\Delta x=16$  m).

The minimum wavelength  $\lambda_{min}$  of the wavefield is 10 m. According to (3-3), the geophone spacing  $\Delta x$  needs to be less than 5 m. For the wavefield with  $\Delta x=1$  m, the  $f$ - $k$  spectrum, as showed on the left part of Fig. 3-3, clearly shows the energy concentrations of five modes. When  $\Delta x$  increases up to 16 m, as showed on the right part of Fig. 3-3, there are several additional energy concentrations appearing on the  $f$ - $k$  spectrum. These are the aliasing phenomena due to large geophone spacing.

### 3.2.2 Leakage due to space domain truncation and modal separation: the geophone spread, $L$

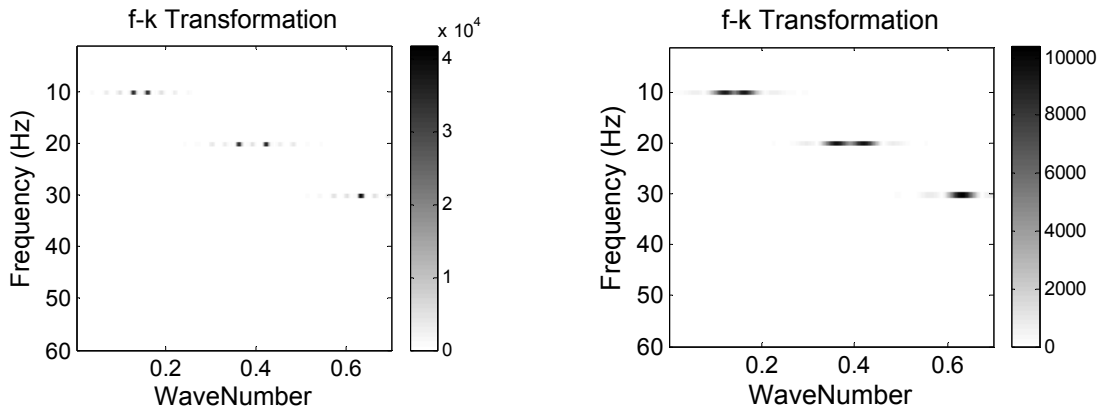


Fig. 3-4 The geophone spread  $L$  affects the modal separation  
the  $f$ - $k$  spectra of the synthetic wavefields (Left:  $L=1024$  m; Right:  $L=256$  m)

Similarly to that in the time domain, the discretization and truncation in the space domain may cause wave number aliasing and leakage respectively. Wave number aliasing can be avoided by using a sufficiently small  $\Delta x$  as given by (3-3). According to the modal summation theory,  $U(f_i, x_n)$  is a summation of harmonic functions in space. Analogous to (3-2), the measurement range in space ( $L$ ) should be sufficiently long to avoid leakage problem.

$$L = (N - 1)\Delta x \geq \lambda_{\max} \quad (3-4)$$

where  $\lambda_{\max}$  is the longest wavelength of interest and  $N$  is the number of sampling in space domain.

The influence caused by the geophone spreading  $L$  on modal separation is presented on Fig. 3-4. The synthetic wavefield ( $\Delta t=0.005$  sec,  $M=2048$  and  $\Delta x=1$  m) consists of five modes of vibrations as listed on Table 3.1.

Table 3.1 The left f-k spectrum is obtained from the wavefield with 1024 traces ( $L=1024\text{m}$ ); the right one is obtained from the wavefield with 256 traces ( $L=256\text{m}$ ). It is obvious that the energy concentrations are not as clear when geophone spread increases from 256m to 1024m. The will make mode separation more difficult.

The phase angle increases linearly with the source-to-receiver offset for a single mode of surface wave. However, when there are multiple modes,  $\varphi(x)$  becomes non-linear. Consider the wavefield of a single frequency surface wave consisting of two modes as shown in Fig. 3-5. The mode velocities at  $f=10$  Hz are  $v_0=200$  m/s and  $v_1=400$  m/s. Fig. 3-6 shows that  $f(x)$  oscillates around the linear line of the dominant mode with an oscillation wavelength equal to  $2\pi/\Delta k$ , where  $\Delta k=k_0-k_1$  is the difference between the wave numbers of the two modes. The  $f$ - $k$  transform method is more effective in mode separation, especially when more than two modes are present. The ability to separate two modes depends on the length of the survey line ( $L$ ) and how close adjacent two modes are. The criteria for mode separation can be written as

$$L \gg \frac{2\pi}{\Delta k} \quad (3-5)$$

where  $\Delta k=k_0-k_1$  is the difference between the wave numbers of two mode. The peaks associated with two adjacent modes in the f-k amplitude spectrum cannot be distinguished if the above criterion is not satisfied.



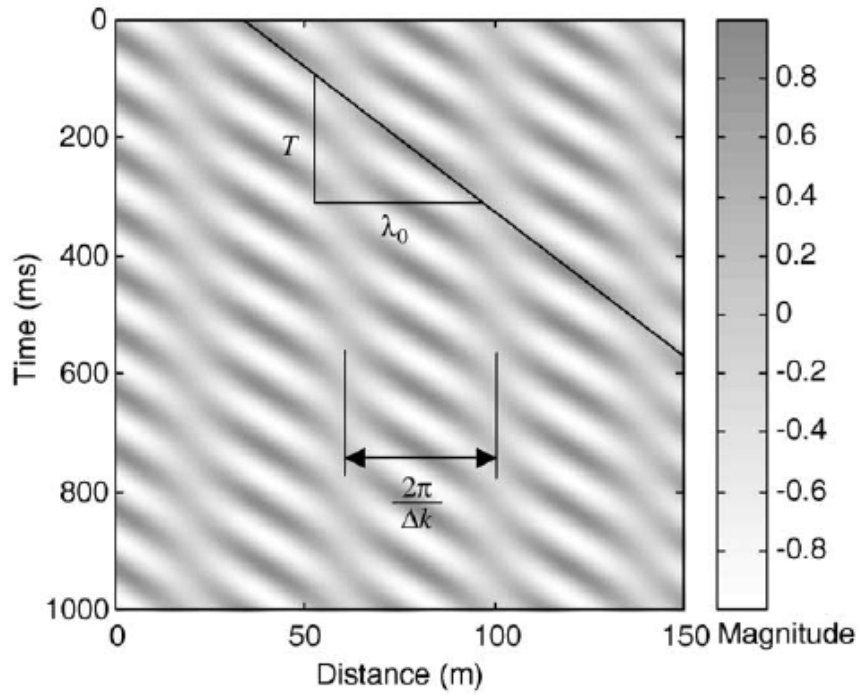


Fig. 3-5 An example wavefield of a multi-mode surface wave

( $f=10$  Hz,  $v_0=200$  m/s, and  $v_1=400$  m/s)

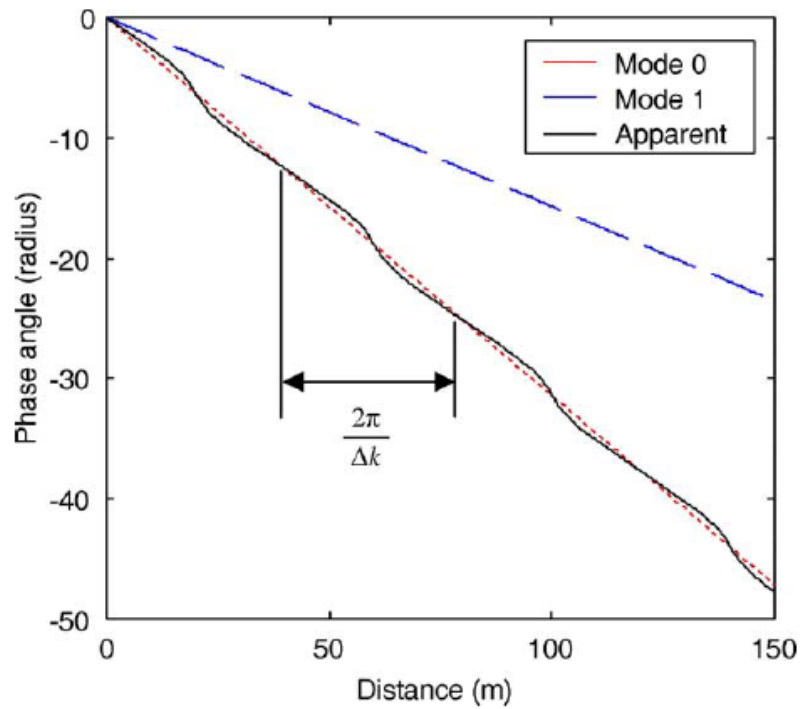


Fig. 3-6 Effects of multiple modes on the phase angle as a function of the source-to-receiver offset.

The phase velocities at 10 Hz for Mode 0 and Mode 1 are 200 and 400 m/s, respectively. The amplitude ratio of

Mode 0 to Mode 1 is 6:4.

### 3.2.3 Near and far field effects: the minimum offset, $X_0$ and maximum offset, $(X_0+L)$

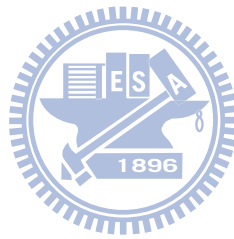
The surface waves attenuate due to spherical spreading at a rate of  $r^{-1/2}$  along the free surface, where  $r$  is the distance from the source. Aside from geometric spreading and scattering at discontinuities, seismic wave amplitudes are degraded by inelastic loss during propagation known as intrinsic or material attenuation. These attenuations reduce the signal-to-noise ratio of the testing data, especially for higher frequency components. In addition to the signal attenuation with distance, there is a strong interference of body waves at nearer offsets. In dispersion analysis, plane wave condition is often assumed. At nearer offsets, the plane wave condition does not hold and it can be difficult to identify the surface wave components because the recorded seismograms contain influence from body waves. This effect contaminates the surface wave data and induces errors on the dispersion analysis. The phenomenon is often called “near field effect”. On the other hand, for those of longer offsets, surface waves of higher frequencies may attenuate so much and there is not enough S/N ratio. That is often referred as “far field effect”. Both near field and far field effects play important roles in selecting the test configuration and processing the signals of surface wave testing.

The near field is defined as the area in the vicinity of the source where the body-wave field is of the same order of magnitude as the surface-wave field. Numerical studies have shown that depending on the variation of shear wave velocity with depth, near-field effects are significant up to a distance from the source from one-half to two wavelengths.

The measurable frequency also decreases as near offset increases. Although it is generally true that surface wave is much more energetic than body waves, the high-frequency (short-wavelength) components lose their energy quite rapidly because they normally propagate through the shallowest veneer of the surface where attenuation is most significant. Contamination by body waves because of attenuation of high-frequency ground roll at longer offsets is referred to as the far field effect (Park et al, 1999). This effect limits the highest

frequency at which phase velocity can be determined.

Although a long survey line is desirable to identify individual modes in Rayleigh waves when multiple modes participate, it is often impractical and it is not known a priori how long is long enough. In practice, the available testing space, source characteristics, near field effect, and attenuation restrict the range of source-to-receiver offsets where  $\phi(x)$  can be measured accurately for a particular frequency. Hence, the apparent velocity in a MSASW test is determined from the average slope of  $\phi(x)$  over some source-to-receiver offsets, where  $\phi(x_n)$  varies smoothly with  $x_n$ . The selection of the proper offset range is analogous to the filtering criteria in the SASW test. In the later section, both effects on estimation of phase velocity will be clearly observed in  $\phi$ - $x$  domain.



### 3.2.4 The dilemma

Combining those criteria for selections of spatial parameters as mentioned in previous sections, there are some situations of dilemma for the field testers when conducting MASW. To avoid the aliasing in the space domain, geophone spacing ( $\Delta x$ ) need to be less than half of the minimum wavelength of interest but channels of the seismograph are limited. As a consequence, geophone spread length ( $L$ ) is constrained in a certain range. However, on the other hand, a sufficiently geophone spread is required for mode separation and the investigation depth.

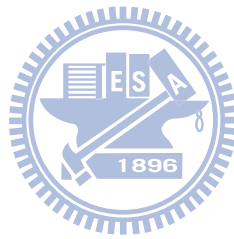
Another scruple is the choice of source-to-receiver offset  $X_0$ . A shorter  $X_0$  causes contamination on low frequency signals due to body waves but a longer one deteriorates higher frequency components due to attenuation. In the other words, that is a tug of war between the near-field and far-field effects.

Conventionally, the “spatial sampling point” is logically assumed to be at the mid-point of the survey line. The measured dispersion curve is the average response of the stratum under the entire survey line. The assumption of horizontally layered medium is inherent to the inverse problems required for estimating the S-wave velocity profile from dispersion curve. The velocity variation due to lateral heterogeneity in a MASW test may be misinterpreted as vertical variation of S-wave velocity.

To increase the spatial resolution of site investigation and minimize the effect of lateral heterogeneity on the estimation of depth–velocity profiles, one might think of reducing the geophone spread ( $L$ ). However, the geophone spread ( $L$ ) in a MASW test should be sufficiently long for two reasons: (a) to reduce spectral leakage and (b) distinguish between fundamental mode and possible higher modes (Lin et al, 2004)

Those above controversies lead to ambiguity in selecting field testing parameters. The testing configurations can have a great effect on the test results. But tradeoffs are involved

when selecting the configuration parameters (including temporal and spatial). Especially for beginners of MASW, it could be a perplexity when conducting tests on field. Therefore, a set of standard procedures for selecting appropriate or optimal parameters and collecting abundant data are desired.



### 3.3 The countermeasure: Pseudo-section approach

#### 3.3.1 The concept of Pseudo-section method

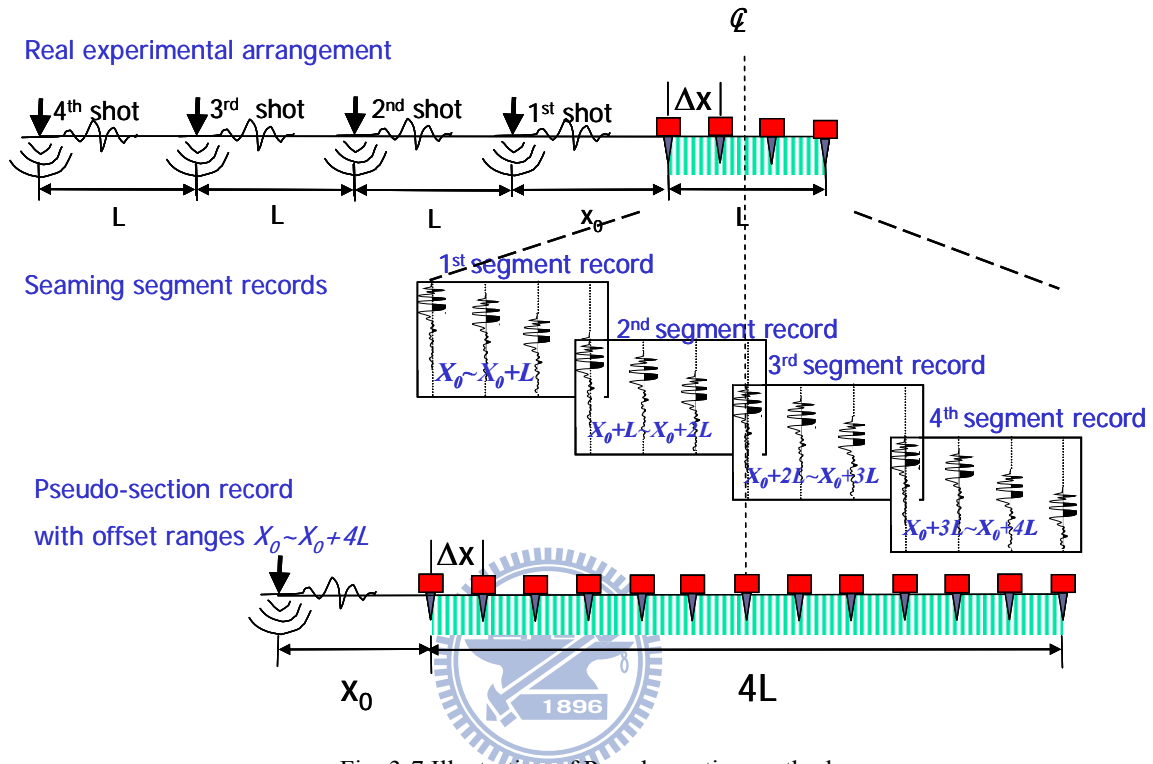


Fig. 3-7 Illustration of Pseudo-section method

To resolve aforementioned controversies, an alternative countermeasure, named pseudo-section, is proposed to reduce the effect of lateral heterogeneity and at the same time increase investigation depths and lateral resolution. It is based on conducting the field survey and collecting the data in a special manner.

The concept of Pseudo-section is to expand the sufficient geophone spreading ( $L$ ) via walk-away and common receiver measurements. For the same survey line, the changes of near offset  $X_0$  generate seismic records with different offset ranges but within the same location of the job site. Synthesizing those records with different offset ranges abstractly expand the offset ranges of a survey line even with a small geophone spread ( $L$ ).

Fig. 3-7 illustrates the concepts of pseudo-section method. Multiple shots are recorded

with spatial intervals between shots equal to geophone spread  $L$  such that the farthest source-to-receiver offset of the preceding shot is equal to the nearest source-to-receiver offset of the subsequent shot. The offset range of the first shot record is from  $X_0$  to  $(X_0+L)$ , same as using the conventional multi-station configuration. After three consecutive walk-away shots, all collected field data can be synthesized into one seismic record according to the source-to-receiver offset. The synthesized seismic record has an extended offset range from  $X_0$  to  $(X_0+3L)$ . If the number of shots is significantly greater than the number of geophones, the shots and geophones can be interchanged to increase the survey efficiency. Due to the extended offset range, the synthesized seismic record can reduce the truncation leakage problem. In addition, the tradeoffs between channel numbers and geophone spacing can be solved by Pseudo-section method to obtain data meeting both spatial resolution and offset range requirements.

The following summarizes problems of conventional MASW that are resolved by pseudo-section method:



1. The offset range is not limited to the geophone spread ( $L$ ). Short geophone spread can be used to increase lateral spatial resolution without sacrificing the offset range.
2. Sufficient offset range reduces the leakage problem in the space domain during the spectral analysis of signal processing. This will enhance wavenumber ( $k$ ) resolution and facilitate modal separation when multiple modes exist.
3. Sufficient offset range provides optimal offset range selection on  $\phi$ - $x$  domain. The correctness of the estimation of  $v_R$  at each frequency can be enhanced by eliminating the data of some offset ranges in which phase angles are contaminated by the near and far field effects.

### 3.3.2 Combining seismic records of the pseudo-section method

#### 3.3.2.1 Static errors

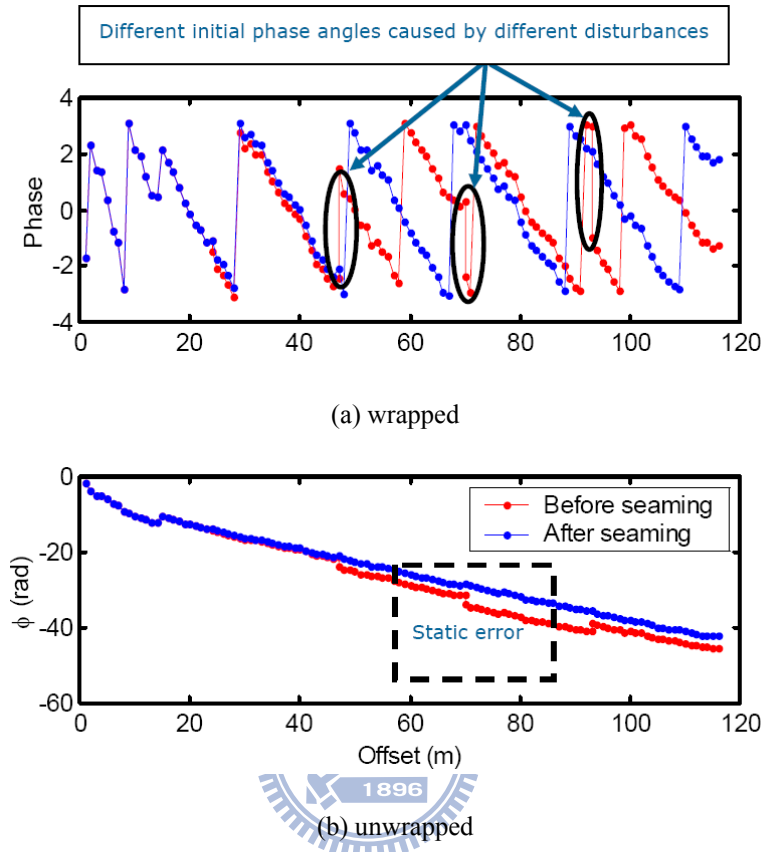


Fig. 3-8 Static errors in  $\phi-x$  domain

Although sufficient offset range can be obtained via the pseudo-section method, trigger delay and lateral variation of the stratum may induce static phase shift in the seismic records and cause discontinuous phase propagation with offset. This discontinuity in the synthesized record of the pseudo-section method will cause errors in the estimation of dispersion curve. An example synthesized record of the pseudo-section method at a particular frequency in the  $\phi-x$  domain is shown in Fig. 3-8, Fig. 3-8(a) shows the static errors of phase angles at each overlapping offset; the static errors are much clearer in Fig. 3-8(b) after unwrapping of phase angles.



### 3.3.2.2 The correction of static errors

A post processing was proposed to correct the static error that may appear in the pseudo-section method. Some experimental results are given in the following to illustrate the correction method and demonstrate its performance.

A series of tests were performed at the Bao-Shan second reservoir in Hshin-Tsu, Taiwan. One seismogram was collected by the conventional single-shot MASW with offset range from 24m to 47m and geophone spacing  $\Delta x = 1\text{m}$ . The other was gathered by multi-shot walk-away tests with same geophone spacing but using only 6 geophones. The offset ranges of these segment records are 24~29m, 29~34m, 34~39m, 39~44m and 44~49m, respectively. These segment records were processed by direct gathered without static correction and synthesized with a static correction procedure. Results were compared with the conventional MASW method.

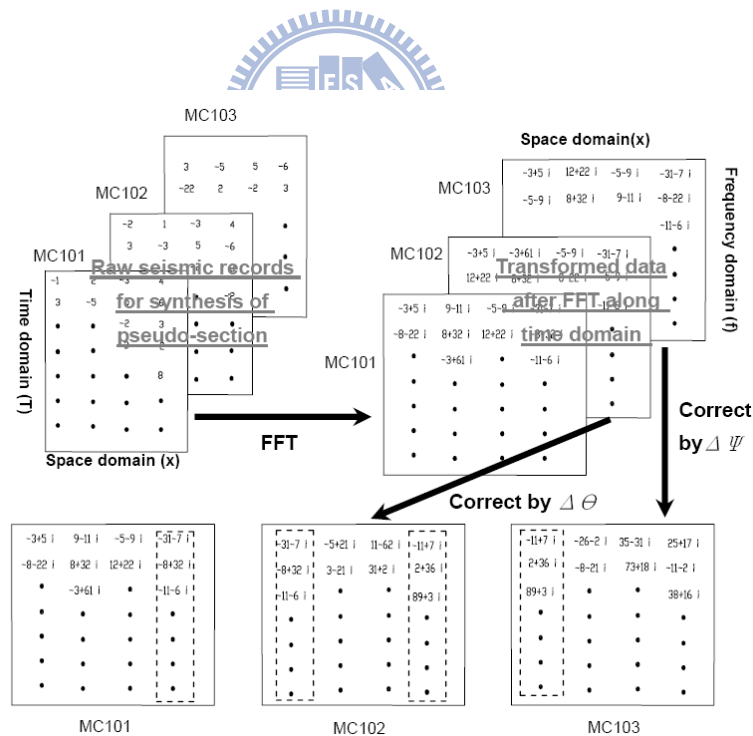


Fig. 3-9 Scheme of signal process for correction of the static error when seaming seismic records for synthesis of pseudo-section

1. Direct gather by source-to-receiver offset

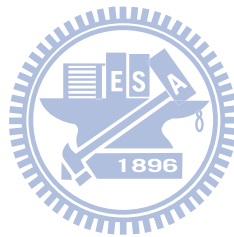
In the pseudo section method, the far offset is kept the same as the near offset of the sequential walk-way shot. The last channel of each segment records may be discarded so that there is no overlapping source-to-receiver offset. Hence the offset ranges of these segment seismic records become 24~28m, 29~33m, 34~38m, 39~43m and 44~49m respectively. These records are then combined for further dispersion analysis.

## 2. Seaming

The static error is generally frequency dependent. To correct the static errors, an additional data reduction procedure is required before further analysis in the space domain. At each frequency, the static phase error between the last waveform of the preceding shot and the first waveform of the subsequent shot is first determined. The static error is then deducted from all traces of the subsequent shot. As shown in Fig. 3-9, for any two consecutive seismic records, they contain one seismic trace at the same source-to-receiver offset. Following the Fourier Transform along the time domain, there may be a phase angle difference  $\Delta\theta$  between the seismic trace of the same source-to-receiver offset. All seismic data of the later record are corrected by a deduction of static error  $\Delta\theta$ . This procedure begins with the first two shot records and repeated for the next pair of shot record (e.g. 2<sup>nd</sup> and 3<sup>rd</sup> shot records) until all static errors are corrected. After static error corrections, the phase angle of any two seismic traces of the same source-to-receiver offset becomes identical such that the correction procedure is called “seaming” and one of them can be removed. The synthetic record of the pseudo-section can then be generated by combining all shot records according to the source-to-receiver offset.

To demonstrate the effectiveness of static error correction, dispersion curves extracted from raw data collected by the conventional and pseudo-section methods are shown on Fig. 3-10. The results on Fig. 3-10 are obtained by (a) unified wavefield transformation, UWFT, and (b) multi-station spectral analysis of surface wave, MSASW. Chapter 4 has a detailed

introduction on these two approaches of signal processing. The dispersion curve from the pseudo-section record with seaming correction agrees well with the dispersion curve from the conventional MASW record in both results. However, the dispersion curve from the pseudo-section record without static correction error shows distinct difference from the dispersion curve from the conventional MASW record, especially in the result from UWFT, Fig. 3-11 further illustrates the static errors and corresponding corrections in  $\varphi-x$  domain. For frequency at which data show a better quality, such as frequency  $f=30\text{Hz}$ , phase angles in  $\varphi-x$  domain are almost identical for all three records, as shown in Fig. 3-11 (a). But for frequency showing static errors, such as  $f=70\text{Hz}$  shown in Fig. 3-11 (b), the importance of seaming correction is obvious. The unwrapped phase angles shown in Fig. 3-11 clearly illustrate that the static error is frequency dependent.



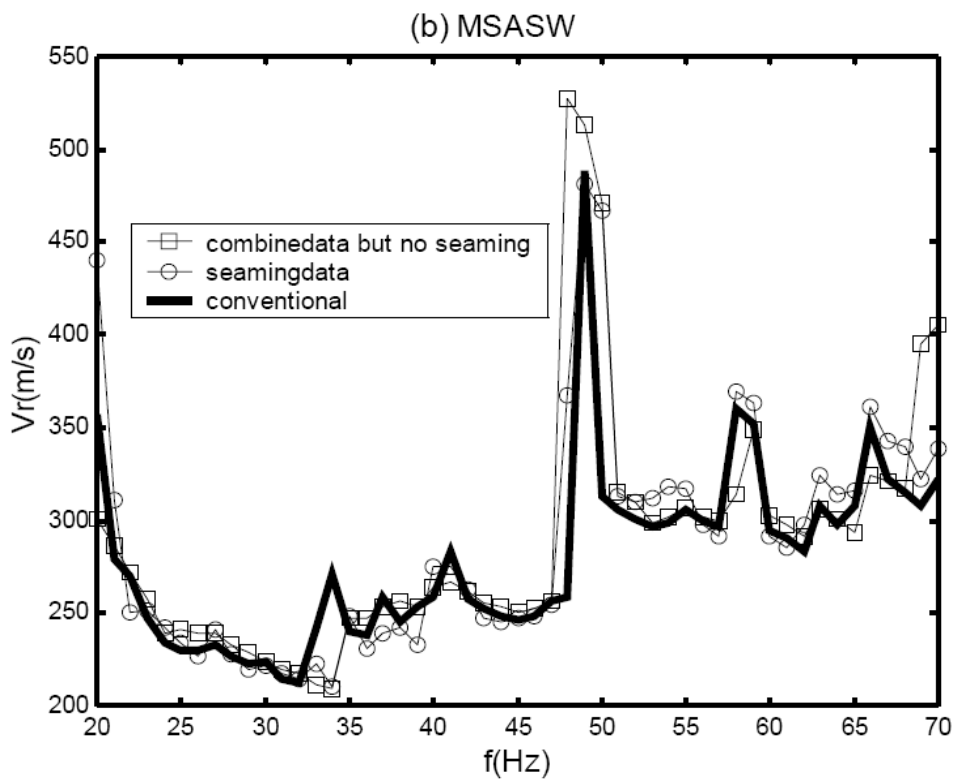
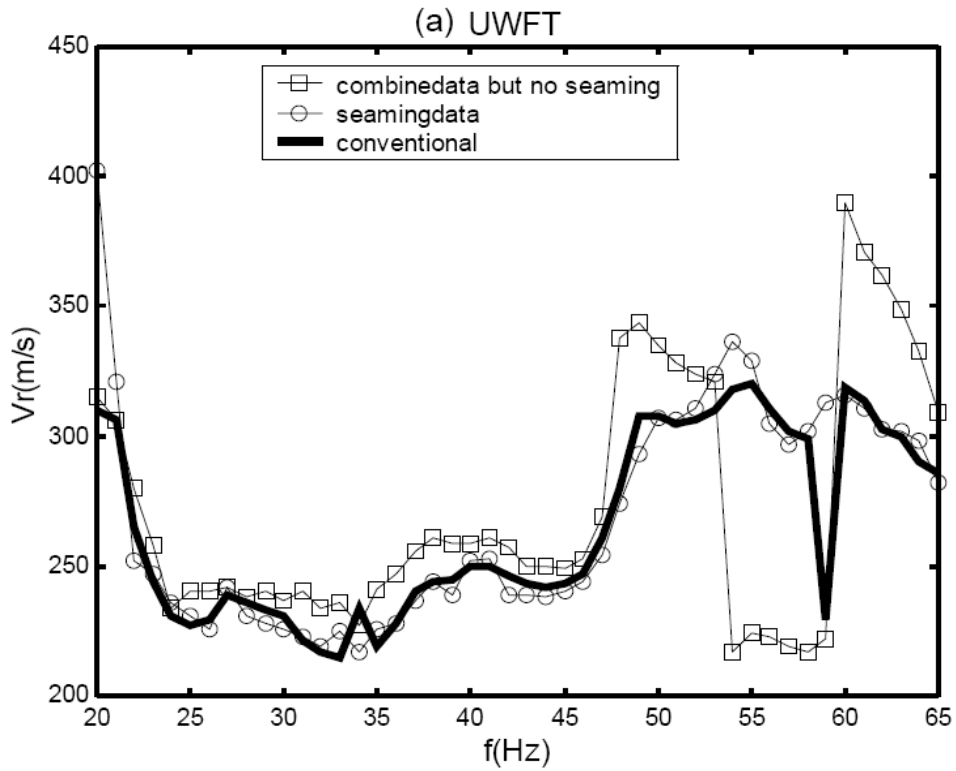
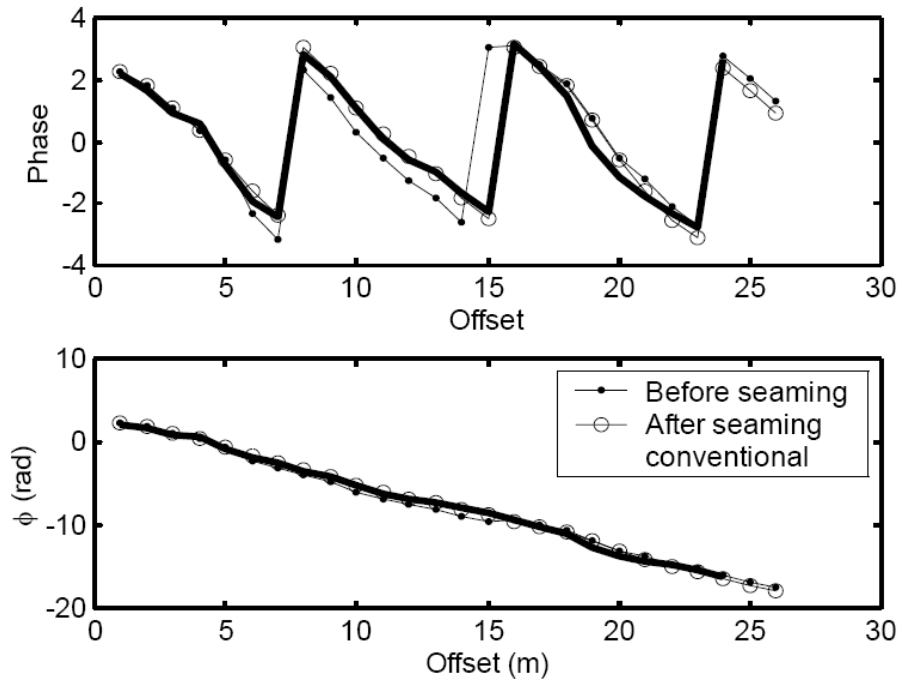


Fig. 3-10 Dispersion curves from conventional and pseudo-section records analyzed by (a) Unified WaveField Transformation (UWFT) (b) Multi-channel Spectral Analysis of Surface Wave (MSASW)

(a)  $f=30$  Hz



(b)  $f=70$  Hz

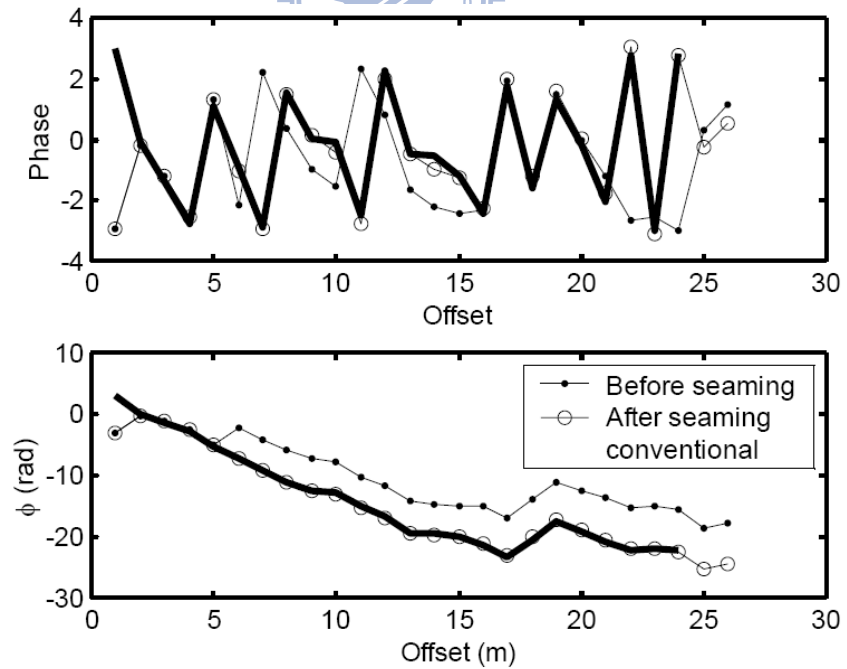


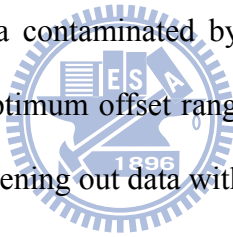
Fig. 3-11 Phase angle difference of conventional and pseudo-section records  
(at frequency  $f=30$ Hz and  $f=70$ Hz)

### 3.3.3 Observation on near and far field effects via pseudo-section method

Although the pseudo-section method can resolve the problems of data leakage and lateral heterogeneity, the inherent near and far field effects of wave propagation remain. With sufficient source-to-receiver offset obtained by the pseudo-section method, however, the data with near and far field effects may be clearly observed and screened out.

A series of field tests conducted at the Pao-Ai campus of NCTU provides a synthesized pseudo-section record with offsets up to 70 m. The unwrapped phase angles in  $\varphi-x$  domain are shown in Fig. 3-12. The phase angle of the wave component at frequency  $f=19\text{Hz}$  does not follow a linear trend from the offset  $x=0\text{m}$  to  $x=20\text{m}$  and from the offset  $x=35\text{m}$  to  $x=70\text{m}$  at frequency  $f=52\text{Hz}$ .

These deviations are apparently due to the near and far field effect. When computing the phase velocity by (2-55), the data contaminated by these deviations will bias the velocity estimation. A technique called “optimum offset range selection” for data quality control will be introduced in Chapter 4 for screening out data with the near and far field effects.



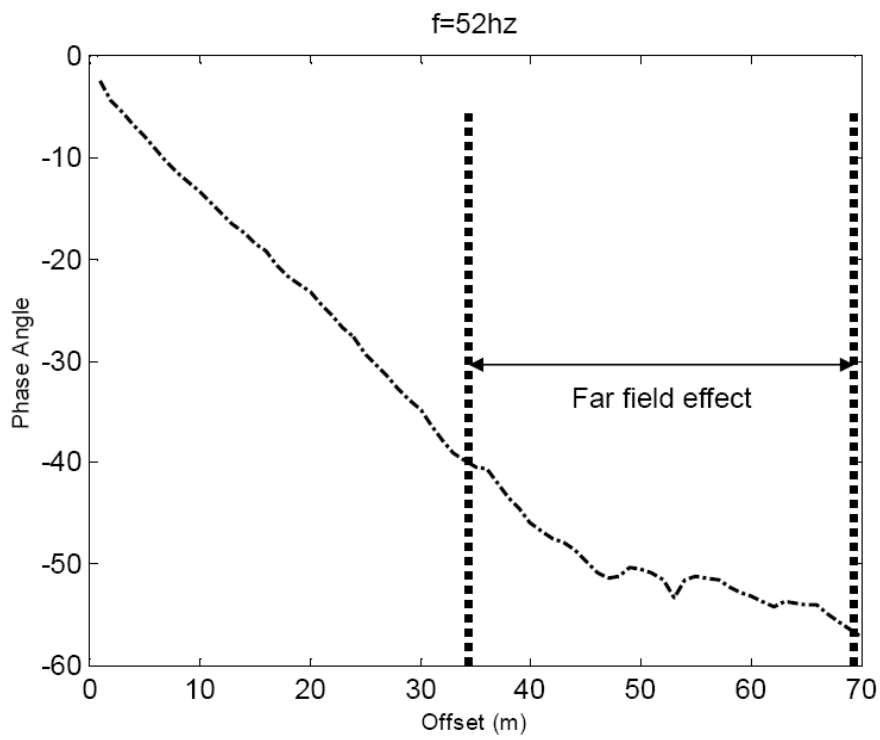
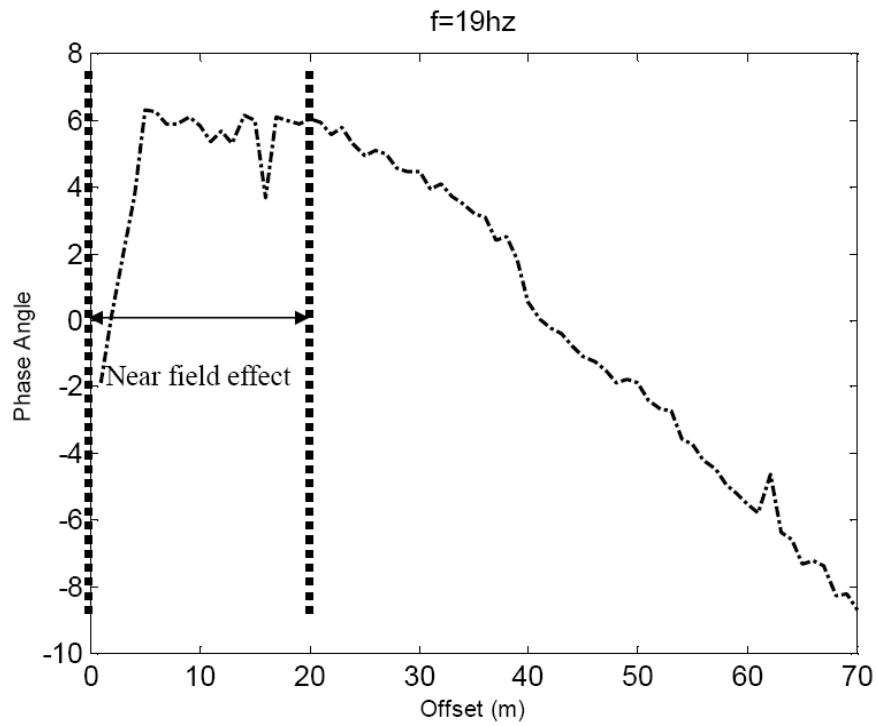


Fig. 3-12 Near and far field effects observed in  $\varphi - x$  domain

### **3.4 Seismic sources and receivers**

The devices for field acquisitions of MASW or other seismic tests basically include a seismograph, sources and receivers. The contemporary seismograph is quite sufficient for sampling intervals and numbers in the time domain. Although data sampling in the space domain is limited by the number of channels in the seismography, the data acquisition by the pseudo-section method can virtually extend the offset range. Therefore the seismography is typically not the critical component in a MASW test.

As mentioned above, the investigated depth is determined by the wavelength. In general, MASW users wish to acquire good quality signals of lower frequencies for larger wavelengths and investigated depths. However, the data quality of seismic signal at low frequency depends mainly on the spectral characteristic of the seismic source and the geological environment of the test site. So improving the energy and spectral characteristic of a seismic source to generate signals of lower frequencies is an important issue for the field tasks of MASW.

Typical receivers used for MASW testing need to be planted into the ground for measuring tremors caused by seismic sources. Planting geophones is time-consuming in the field, especially on hard surfaces like pavement or concrete. To expedite field deployment of MASW testing, non-invasive receivers that perform equally well as planted geophones are desired. This section introduces some improvements on seismic sources and receivers. The performance of these developments will be experimentally evaluated by examining the signal contents and spectral characteristics and comparing with those collected by conventional devices.

#### **3.4.1 Some improvement on the seismic source**

The ways used for seismic tests to actively produce seismic waves can be divided into two categories; mechanical and explosive. The mechanical approach applies the potential or



kinetic energy onto the surface to generate a disturbance of stress field, this category includes hammers or sledgehammers with different weights, weight-drop, spring accelerators and vibrators. The explosive approach mainly includes shotguns and dynamites which generate seismic waves via various kinds of explosion. Due to constraints of the laws, the mechanical sources are more often used in Taiwan for seismic tests.



Fig. 3-13 Electrical operated seismic source ESS100SC

The seismic sources originally available at NCTU are:

1. 12 lb sledgehammer (BH) and other hammer with lighter weights
2. Spring accelerator (AF), ESS100SC, manufactured by Geophysical Instrument Supply Company (GISCO), as shown on Fig. 3-13

From field experience, both sources do not supply sufficient energy for long offsets. Although the signal/noise ratio can be enhanced by signal stacking, the quality of signals at low frequencies is not improved unless the spectral characteristic and energy of the seismic sources are enhanced. So a portable and mobile seismic source that can produce lower frequency signals with higher energy is desirable.



Fig. 3-14 New developed weight-drop seismic source

The new seismic source developed in the study is similar to the weight-drop system used for Standard Penetration Test (SPT), as shown in Fig. 3-14. The system includes a portable tripod providing a maximum dropping distance of 2.5 m, a manual chain block with maximum allowable load of 500 kg and a 125 kg cast-iron ball, 300 mm in diameter.

A series of field tests was conducted at the Pao-Ai campus of NCTU to evaluate the characteristic of the new weight-drop source. Due to its heavy weight, the offset range of the pseudo-section record was obtained from 38m to 104m, for comparison, offset range from 16m to 104m was also obtained for the 12 lb sledgehammer (BH) and spring accelerator (AF). These seismic records are presented in different domains for further discussions of their characteristics, as shown on Fig. 3-15, Fig. 3-16 and Fig. 3-17.

1. The seismograms, time-offset ( $t-x$ ) domain,

The duration of the tremors caused by the BH source is slightly less than 0.1 sec. The energy carried by the surface wave is invisible as the offset exceeds 70 m. For the offset range of 35~55 m, the oscillations of signals seems to be most intact; For the AF source, the

duration of tremors is also slightly less than 0.1 sec and the energy starts to vanish as the offset exceeds 80 m. The oscillations of signals are most intact for the offset range from 25m to 65m. As expected, the duration of the tremors caused by the WD source is about 0.3 sec, longer than those by BH and AF sources. The energy remain significant until the offset exceeds 100 m. The offset range from 45m to 80m offers best quality signals. From the records in time-offset domain, it is obvious that the WD source provides a longer duration of tremors with larger energy. So it can be initially considered that the signals produced by the WD source contain more lower-frequency components than those by BH and AF sources.

## 2. The energy spectrum verse offset in the frequency-offset ( $f-x$ ) domain

After a Fourier Transform with respect to time, the raw  $t-x$  data are transformed to complex data in frequency-offset ( $f-x$ ) domain. The real part (or imaginary part) and amplitude (or energy) of the complex signals can provide different insights.

The energy spectrum of time-domain Fourier Transform can be helpful to understand the energy distributions with respect to frequency and offset. The major frequency content is within 20~80 Hz in the case of BH source. But as the offset exceeds 70m, the energy of signals becomes scattered. And beyond 90m offset, the scattered energy is mainly due to background noises. In the case of AF source, major frequency content is within 20~70 Hz. As the offset exceeds 80m, the energy of high-frequency components become scattered and the dominant frequencies are 20~25 Hz. Beyond 90m offset, the scatter become more serious even in the part of frequency under 20 Hz.

For signals generated by the WD source, the major frequency content is 15~40 Hz. There is almost no energy for frequency components exceeding 40 Hz. But the dominant frequencies remain strong through out the testing offset and show more abundant energy in the low frequency.

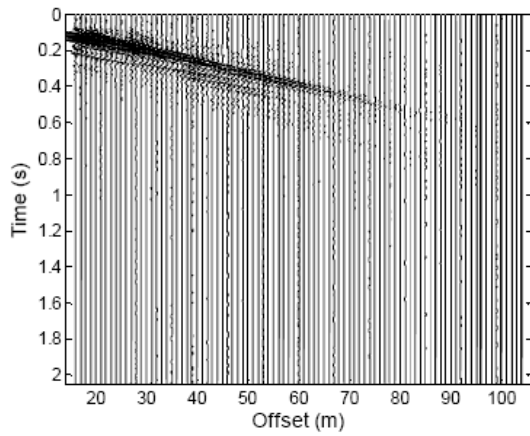
## 3. The real part of time-domain Fourier Transform verse offset in $f-x$ domain

The real part of the time domain Fourier Transform is equivalent to data produced by a harmonic vibrator. For each frequency, the harmonic oscillation with offset can be clearly seen at the region without near and far field effects. The harmonic variations can be observed in the frequency range 25~85 Hz, 20~70 Hz and 15~50 Hz for BH source, AF source and WD source respectively. Offsets that are affected by near or far field effects can also be seen in this domain. This feature will be used in later chapter for screen out data contaminated by near and far field effects.

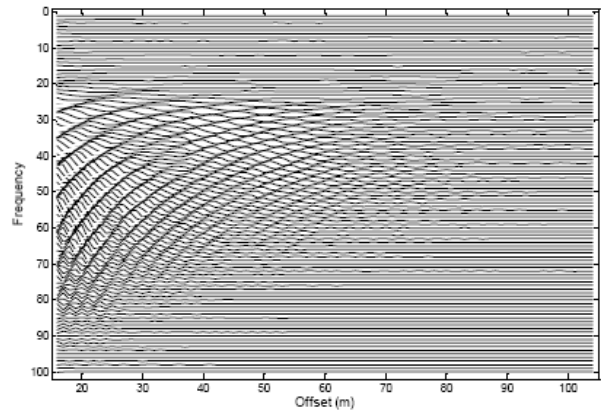
#### 4. The energy spectrum in $f$ - $v$ domain

Using the 2-D wavefield transformation, the dispersion curve can be picked at the peaks in the  $f$ - $v$  energy spectrum. The credible frequency ranges in the dispersion analysis are 20~80 Hz, 20~70 Hz, 15~40 Hz for the BH, AF and WD sources respectively. The corresponding wavelengths are 2.5~20 m, 2.8~22.5 m and 5~33 m.

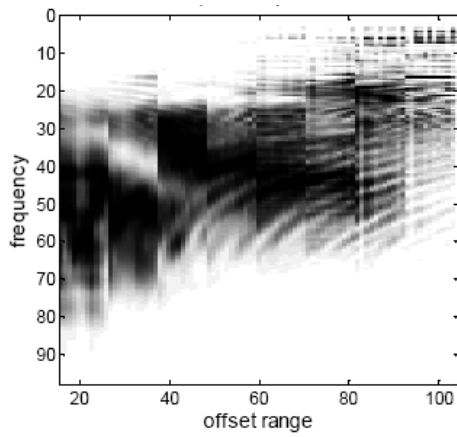
Comparing the above results, the WD source does produce higher energy for low-frequency than other twos. This improvement is important for MASW method because the lower frequency components can effectively increase the sampling depth. The down side is that the signal generated by the WD source loses some higher frequency components. However, the corresponding wavelengths of lost components represent highly concentrated samples in very shallow depth. These high frequency components may be supplemented by using a sledgehammer for the near offsets (e.g. offset < 38m). Therefore the new weight-drop source can play an important role to extend the investigation depth in MASW testing.



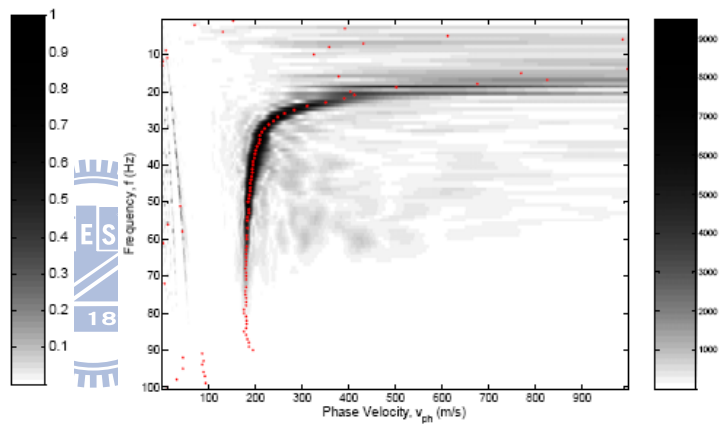
(a) The  $t$ - $x$  seismogram



(b) The real part of time-domain Fourier Transform vs offset in  $f$ - $x$  domain

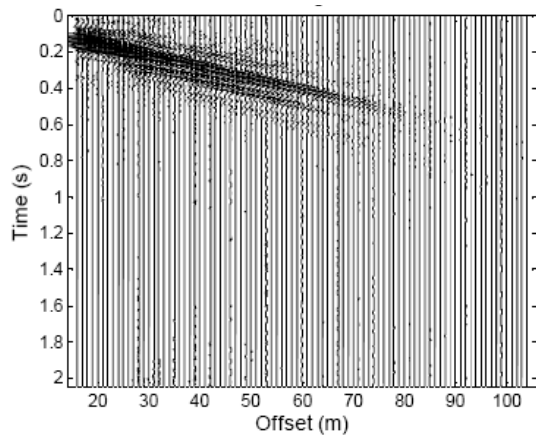


(c) The energy spectrum vs offset in the  $f$ - $x$  domain

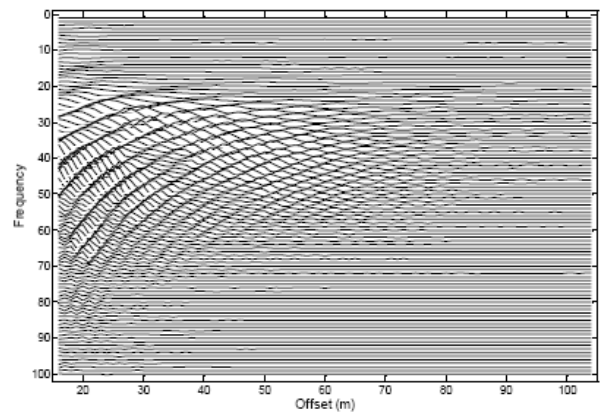


(d) The energy spectrum in  $f$ - $v$  domain

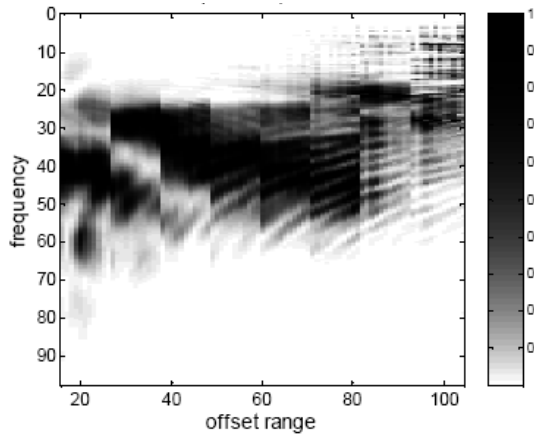
Fig. 3-15 The pseudo-section record by the source of the 12 lb sledgehammer (BH)



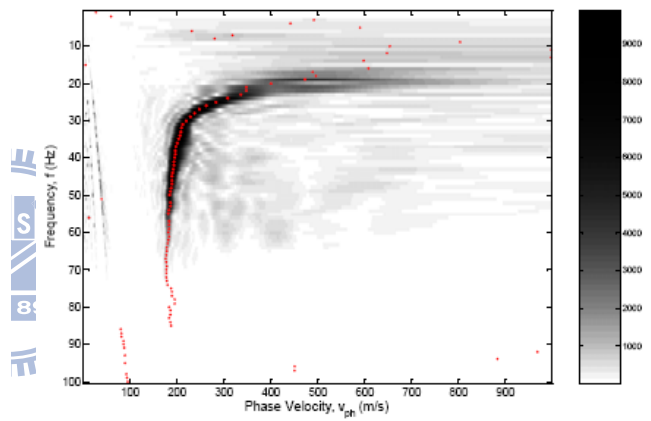
(a) The  $t$ - $x$  seismogram



(b) The real part of time-domain Fourier Transform vs offset in  $f$ - $x$  domain

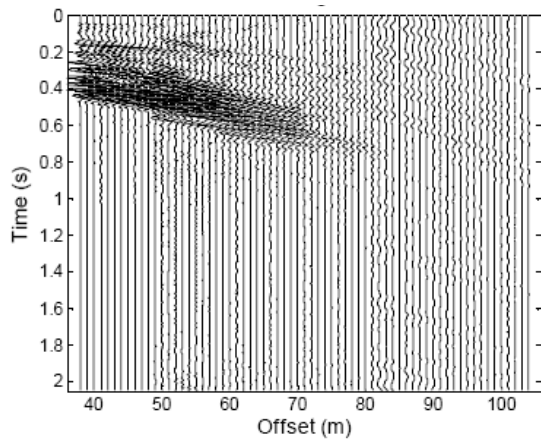


(c) The energy spectrum vs offset in the  $f$ - $x$  domain

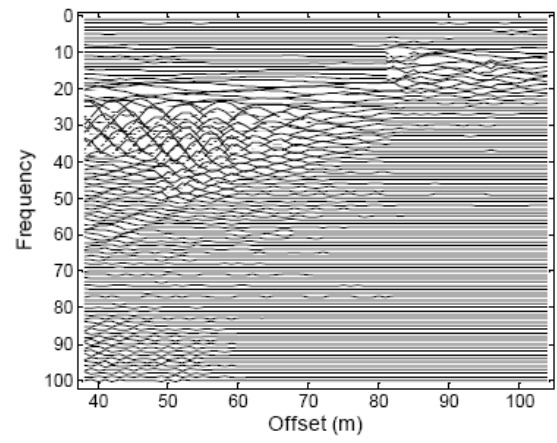


(d) The energy spectrum in  $f$ - $v$  domain

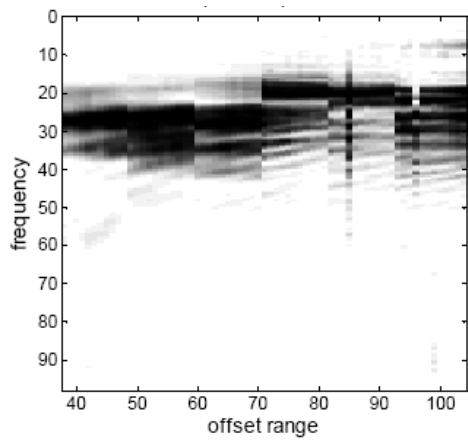
Fig. 3-16 The pseudo-section record by the source of the spring accelerator (AF)



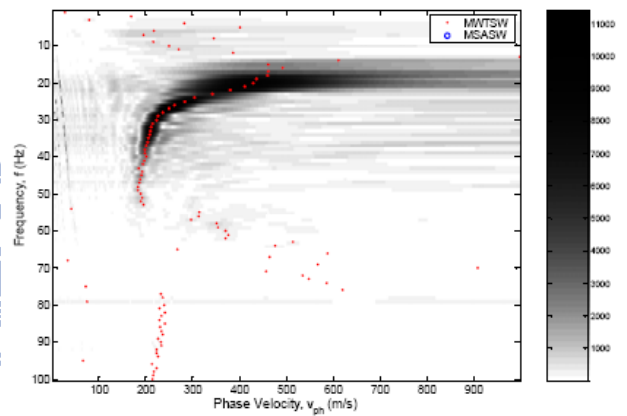
(a) The  $t$ - $x$  seismogram



(b) The real part of time-domain Fourier Transform vs offset in  $f$ - $x$  domain



(b) The energy spectrum vs offset in the  $f$ - $x$  domain



(d) The energy spectrum in  $f$ - $v$  domain

Fig. 3-17 The pseudo-section record by the source of the new developed weight-drop source (WD)



### 3.4.2 Some improvement on the receivers

The receivers, or geophones, used for data acquisition in this study are OYO Geospace GS-11D. The geophone natural frequency is 4.5 Hz. The truthfulness of the tremors of ground surface depends on the coupling between geophones and the ground provided by planting installations. However, planting installations is time-consuming for hard surfaces like concrete or pavement. If the geophone spread is to be moved forward for a 1.5-D survey, the installation of geophones could be a formidable task. This problem calls for development of a non-invasive geophone string.

Different from spike receivers used on land, geophysical scientists use a series of hydrophones, so-called “marine streamer”, dragged at the aft of a ship to receive marine seismic data. Massive data can be sufficiently collected due to its acquisition efficiency. Referring to the marine type receivers, geophysicists have developed a series of geophones bound by belts, called “land streamer”, for fast data acquisitions on land seismics. Basically the land streamers should provide sufficient weight for well coupling between geophones and the ground. At present there are several designs available by different institutions like Kansas Geological Survey (USA) and Tyrens (Sweden).

A similar land streamer was developed at NCTU and experimentally evaluated to verify its feasibility. The main concept of the new land streamer developed at NCTU is a receiver pedestal on which OYO Geospace GS-11D geophone can be attached. As shown on Fig. 3-18, it is made of aluminum alloy due to its high strength and lightweight. The sizes of the upper and lower plates are 16\*10\*0.6 cm and 12\*10\*0.6 cm respectively. Two plates are bonded by 4 1/8-inch bolts. The weight of a single unit including the geophone is 0.7 kg. The receivers are connected by a 5-cm wide polyester belt between the upper and lower plates for dragging operation. The interval of receivers can be adjusted as required in a particular survey, as shown in Fig. 3-19.



A series of field tests was conducted at the Pao-Ai campus of NCTU to verify the performance and reliability of the newly developed land streamer. The records were collected by the conventional spike geophone array (SGA) and the new land streamer (LS) on the surface of asphalt pavement. The offset ranges of the pseudo-section records by the BH and WD sources are 16~93 m and 38~104 m respectively. Fig. 3-20 and Fig. 3-21 present the testing results in different domains.

1. The seismograms, time-offset ( $t-x$ ) domain,

For the signals generated by the BH source, the seismograms collected by LS and SGA agree well in the far offset range. In the nearer offset range, however the first-arriving times are slightly different. This implies that the coupling between land streamers and the ground less sufficient for high frequency (short wavelength) components.

For the signals generated by the WD source, the seismograms collected by LS and SGA are consistent in both far and near offset ranges. As mentioned in the previous section, the signals produced by the WD source lose some higher-frequency components. Therefore inconsistency of seismograms in nearer offset ranges is not apparent. The performance of LS receivers will be further evaluated in other domains.

2. The energy spectrum verse offset in the  $f-x$  domain

For the signal generated by the BH source, the effective bandwidth of the signals recorded by LS is 20~70 Hz while that recorded by SGA is 20~80 Hz. The difference between the LS and SGA mainly occurs in the nearer offset ( $< 49\text{m}$ ). It appears that some higher-frequency components ( $> 70\text{ Hz}$ ) in nearer offset ranges ( $< 49\text{ m}$ ) are lost in data by the LS receiver. This phenomenon may be attributed to less sufficient coupling between the LS receivers and the ground surface. Wave components that are lost in the data recorded by

the LS are those of wavelength  $< 3\text{m}$ .

For signals generated by the WD source, the signals recorded by the LS and SGA receiver have the almost identical spectral energy distribution. The inconsistency between signals recorded by the LS and by the SGA receivers does not appear when the WD source is used. That is because the WD source does not produce some higher-frequency components of surface wave as comparing to the BH source does.

From the above results, the LS receiver seems to act as a role of low-pass filter when recording the tremors and may lose some high frequency (short wavelength) components. Wave components, whose wavelength are less than 3m may be eliminated by the less ideal coupling between the LS streamers and the ground surface.

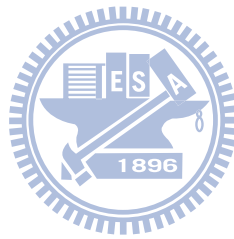
### 3. The energy spectrum in the $f$ - $v$ domain

The ultimate result of a MASW field test is the estimated dispersion curve. Therefore, the performance of the LS receivers should ultimately evaluated by comparing resultant dispersion curve with that obtained by the SGA receivers. For BH source, the dispersion curves obtained by the LS recordings generally agree well with that from the SGA recordings. Although there is some inconsistency for the frequencies greater than 70 Hz (the corresponding wavelengths is smaller than 3 m), velocity difference is not significant and it only slightly affect information related to shallow depths.

Due to the original loss of higher-frequency components of signals induced by the WD source, the  $f$ - $v$  spectra and dispersion curves extracted from the LS recordings and SGA recordings are in good agreement in the whole effective bandwidth.

In summary, on hard surface like asphalt pavement, wave components whose wave length is less than 3 m are significantly attenuated due to the non-ideal coupling between the LS streamers and the ground surface. However, the experimental results shows the resultant

dispersion curve is only slightly affected in those short wavelengths. This difference from results obtained by the traditional SGA receivers is considerable minor. Thus, the LS receiver can used to offer significant efficiency boost infield works with enough confidence in data quality.



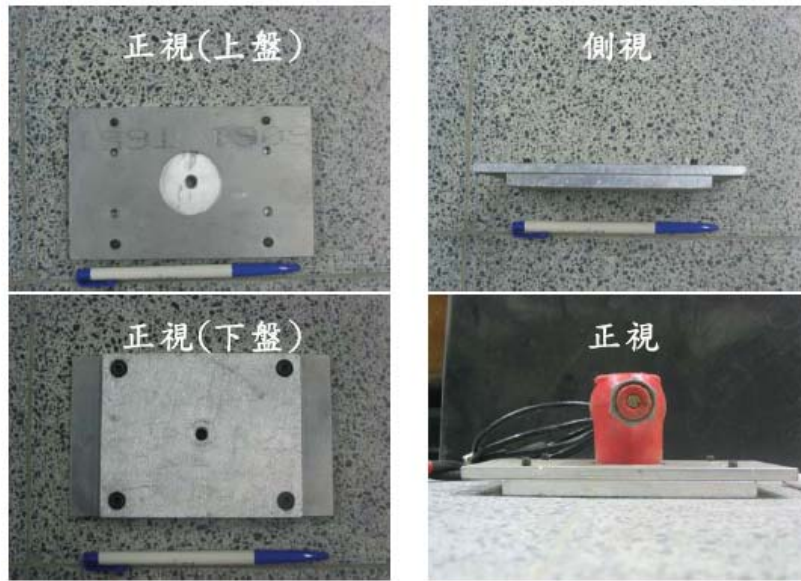


Fig. 3-18 The pedestals and receiver of the land streamer developed at NCTU



Fig. 3-19 The land streamer developed at NCTU

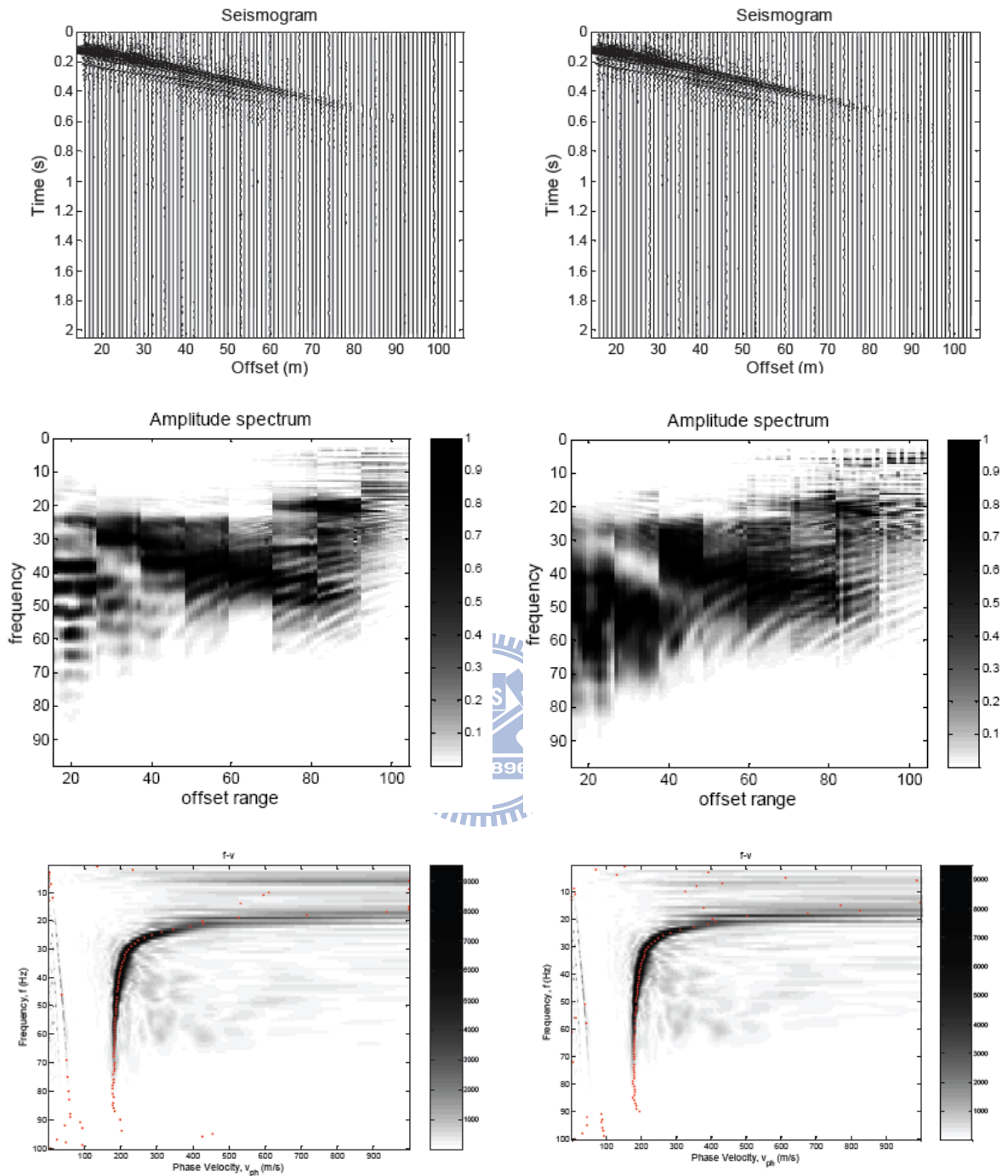


Fig. 3-20 The pseudo-section records collected by Land Streamer (left) and Spike Geophone Array (right) in  $t-x$ ,  $f-x$  and  $f-v$  domains (signals produced by the BH source)

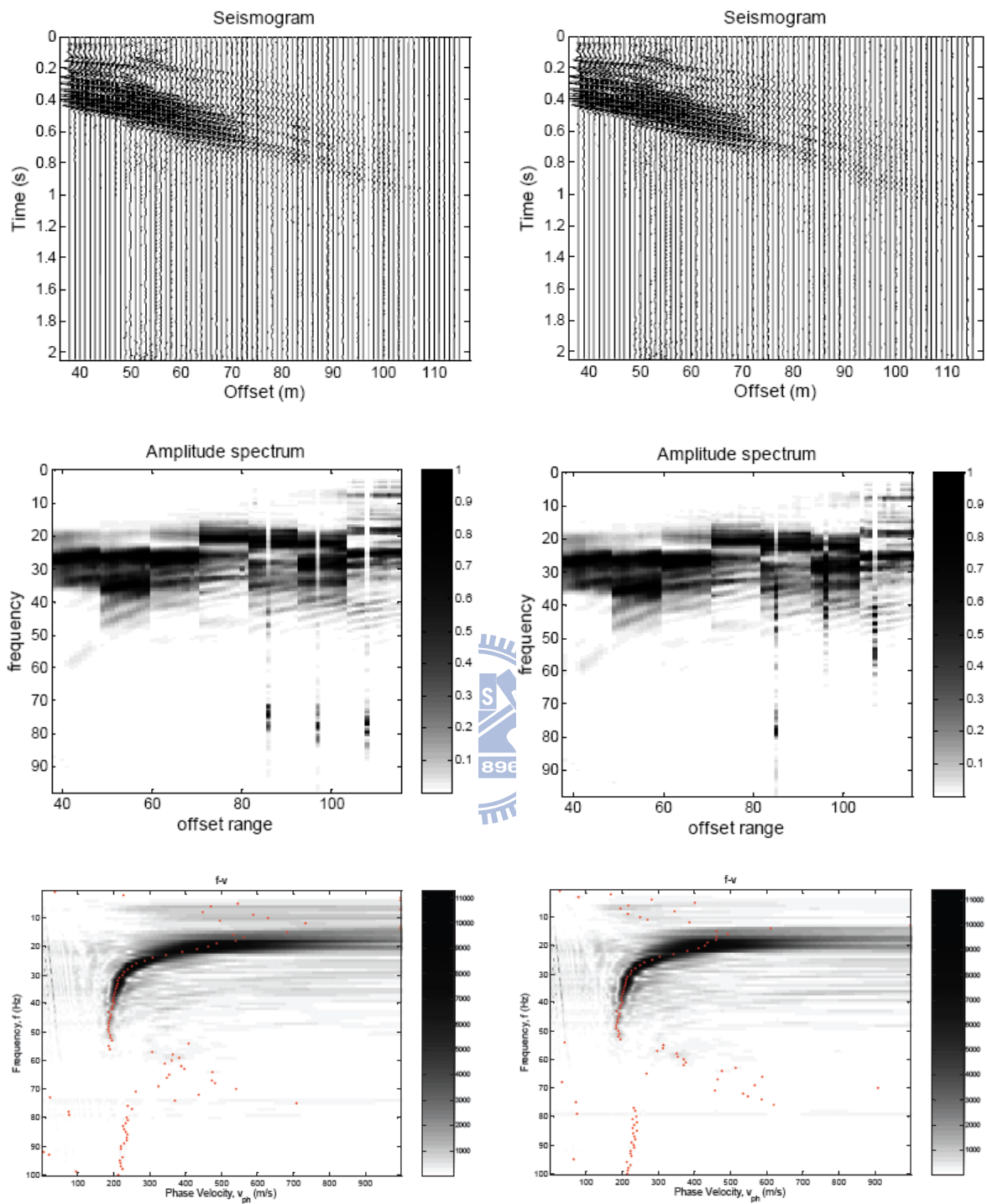


Fig. 3-21 The pseudo-section records collected by Land Streamer (left) and Spike Geophone Array (right) in  $t-x$ ,  $f-x$  and  $f-v$  domains (signals produced by the WD source)

### 3.5 The proposed standard field testing

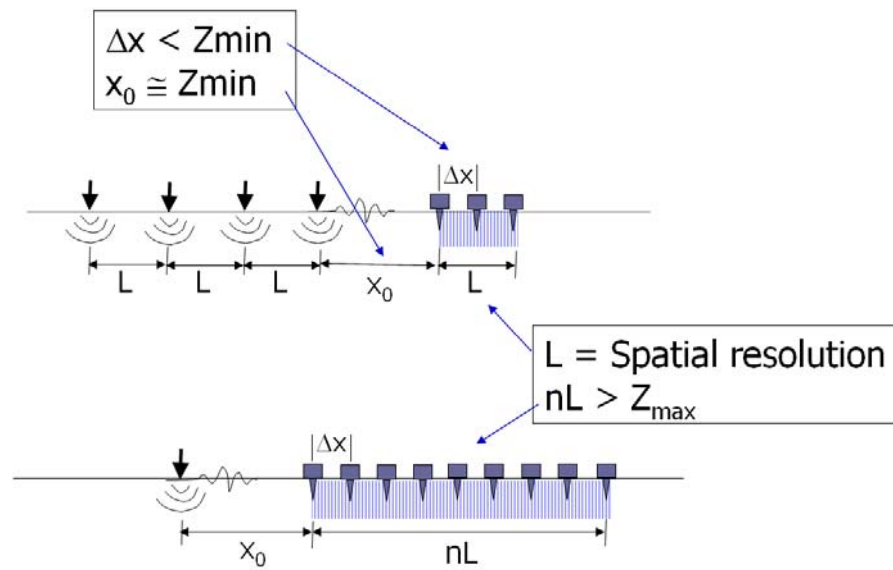


Fig. 3-22 (a) The proposed standard field testing configuration and (b) the corresponding pseudo-section.

After investigating the influences of field parameters, the rules for choosing parameters lead to dilemmas. However a countermeasure, the pseudo-section method, is proposed to resolve the problems. The standard field testing arrangement, as shown in Fig. 3-22, and procedures are summarized as the following:

1. The wavelength  $\lambda$  positively correlates with the disturbed depth  $Z$  during the surface wave propagation. According to the anti-aliasing rule in space domain, the geophone spacing,  $\Delta x$ , should not be greater than  $1/2 \lambda_{min}$ . It is reasonable to use the minimum depth of interest  $Z_{min}$  as the geophone spacing and the minimum offset  $X_0$  for recording complete wavefield.
2. The geophone spread  $L$  can be determined by the desired spatial resolution. But the virtual geophone spread  $nL$  of the combined pseudo-section record should be sufficiently long for solving the leakage and modal separation problems.
3. The near and far field effects are controlled by the minimum offset  $X_0$  and maximum virtual offset ( $X_0+nL$ ). They can not be avoided by choosing field

parameters. However, these effects can be mitigated during the signal process. It will be introduced late in the next chapter.

4. The non-invasive receiver stream can be used to improve testing efficiency if necessary.
5. The heavy weight-drop source can be used to enhance the low frequency measurements if necessary.





## 4 Unified dispersion analysis

Several algorithms were proposed to analyze the dispersion relation from the recorded wavefield of surface waves. The SASW uses only the information of phase angle Fourier Transformation with respect to time. Other methods of dispersion analysis involve subsequent transformation in the space domain. They transform the survey data in the  $t$ - $x$  domain into frequency- wavenumber ( $f$ - $k$ ) (Capon, 1969; Yilmaz, 1987; Alleyne et al, 1990; Forchap et al, 1998; Lu et al, 2004), frequency- slowness ( $p$ - $f$ ) (McMechan et al, 1981) or frequency- velocity ( $f$ - $v$ ) (Park et al, 1998b) domains. Whether the dispersion relation in  $f$ - $k$ ,  $f$ - $p$  and  $f$ - $v$  spectra can be clearly and accurately identified depends not only on the complexity of strata and field configuration, but also on the discrete transformation algorithms. Several studies have made comparisons among aforementioned transformation algorithms, but different algorithms were favored without consensus (Foti, 2000; Beaty, 2002; O'Neil, 2004; Mora, 2003; Xia et al, 2005). It is often ambiguous as to which algorithm should be used.

Another problem of current available dispersion analysis methods is the lack of mechanism for screening the wavefield data and estimating the uncertainty of the dispersion analysis. The dispersion analysis is performed using the entire wavefield recorded without screening out the contaminated data. No data quality or standard deviation is given for the resultant dispersion curve.

To resolve the ambiguity and provide appraisal for the dispersion analysis, a unified dispersion analysis is proposed in this study. The procedures start with a Fourier Transform with respect to time that transforms the  $t$ - $x$  wavefield into the  $f$ - $x$  domain. In this domain, a new dispersion analysis, called multi-station spectral analysis of surface wave (MSASW), is proposed using the variation of phase angles with offset. The data quality of the dispersion curve can be evaluated in this new approach. In the  $f$ - $x$  domain, wavefield contaminated by the near and far field effects can also be identified and screened out before the dispersion

analysis.

The unified procedure is followed by another Fourier Transform with respect to space that transforms the wavefield into another  $f-k$ ,  $f-p$ ,  $f-v$  or  $f-\lambda$  representations. The dispersion curves obtained by different transformation are shown to be exactly equivalent by a newly-proposed optimization method for dispersion analysis. Further investigations on the data sampling of the dispersion curve are also discussed in this chapter.



## 4.1 Analyses in the frequency-space ( $f$ - $x$ ) domain

### 4.1.1 Representation of surface waves in $f$ - $x$ domain

Neglecting material damping, the surface-wave signal  $u$  (, be it displacement, velocity, or acceleration) for a single mode observed at a distance  $x$  from the source and a particular frequency  $\omega$  ( $=2\pi f$ ) is written as

$$u(x, t) = \frac{1}{\sqrt{x}} S(\omega) A(\omega) e^{-j\psi} e^{-jkx} e^{j\omega t} \quad (4-1)$$

where  $S(\omega)$  is complex source spectrum,  $A(\omega) \exp(-j\psi)$  represents the complex excitation of surface waves for a point source;  $k$  is the wave number whose reciprocal  $\lambda$  ( $= 2\pi/k$ ) is the wavelength. The wave number is related to the phase velocity  $v$  by the definition  $\omega = kv$ . Eg. (4-1) represents the wave propagation and decay of a single-mode surface wave. The surface wave which includes multiple modes can be rewritten as (Aki et al, 2002):

$$u(x, t) = \frac{1}{\sqrt{x}} S(\omega) e^{j\omega t} \sum_m A_m(\omega) e^{-j(k_m x + \psi_m)} \quad (4-2)$$

where the index  $m$  is the mode number. The presence of multiple modes complicates the interpretation of phase velocity. (4-2) can be written in the form of (4-1) as:

$$u(x, t) = \frac{1}{\sqrt{x}} S(\omega) A'(\omega) e^{-j\phi(x, \omega)} e^{j\omega t} \quad (4-3)$$

where  $A'(\omega)$  is the effective magnitude function of excitation and  $\phi(x, \omega)$  is a composite phase function. The position of a given characteristic point of the harmonic wave (such for example a peak or a trough) is described by constant values of the phase:

$$\omega t - \phi(x, \omega) = \text{const} \quad (4-4)$$

Hence differentiating with respect to time, the local phase velocity  $v(x)$  can be defined as:

$$v(x) = \frac{\omega}{\frac{\partial \phi(x, \omega)}{\partial x}} \quad (4-5)$$

It is important to note that since the Rayleigh wave velocity is a function not only of the frequency but also of the distance from the source, it is a local quantity.

As mentioned in Chapter 2, For a discrete 2-D wavefield collected,  $u(t_m, x_n)$  with  $m$  samples in time domain and  $n$  samples in space domain, most adopted algorithms start with a DFT and its DFT spectra at multiple stations is as expressed as (2-56),

$$U(f_i, x_n) = \frac{1}{M} \sum_{m=0}^{M-1} u(t_m, x_n) \exp(-j2\pi f_i t_m) \quad (4-6)$$

where  $u$  is the velocity or acceleration measured by the receiver,  $U$  is the DFT of  $u$ ,  $j = \sqrt{-1}$ ,  $t_m = m\Delta t$ ,  $f_i = i\Delta f = i/[(M-1)\Delta t]$ , and  $x_n = n\Delta x$ . The  $i$ ,  $n$ , and  $m$  in (4-6) are integer indices to represent respectively discrete points in the frequency, space, and time domain.

In most literature, the frequency-offset data transformed from the time-offset wavefield is merely treated as a midway product during the dispersion analysis. However, by examining the oscillation of phase angle and the concentration of energy along the offset for each specific frequency, representation of the wavefield in the  $f$ - $x$  domain can be helpful to estimate the data uncertainty and to undertake some procedures for enhancing data quality.

### 4.1.2 Real part and energy spectrum of the $f$ - $x$ complex data

As discussed in Sec. 3.4, the real part (or the imaginary part) oscillation and the energy or amplitude spectrum of the  $f$ - $x$  complex data  $U(f_i, x_n)$  converted from the  $t$ - $x$  wavefield is applied not only for analyzing the frequency content of signals but also for understanding the influence caused by the near and far field effects.

As shown in Fig. 3-15, Fig. 3-16 and Fig. 3-17, the major energy distributions for different sources in both of the frequency and offset domains can be observed. The real-part oscillation of the  $f$ - $x$  complex data can also be plotted as a 2-D wiggle plot, which is useful for understanding the frequency content and signal quality of plane waves.

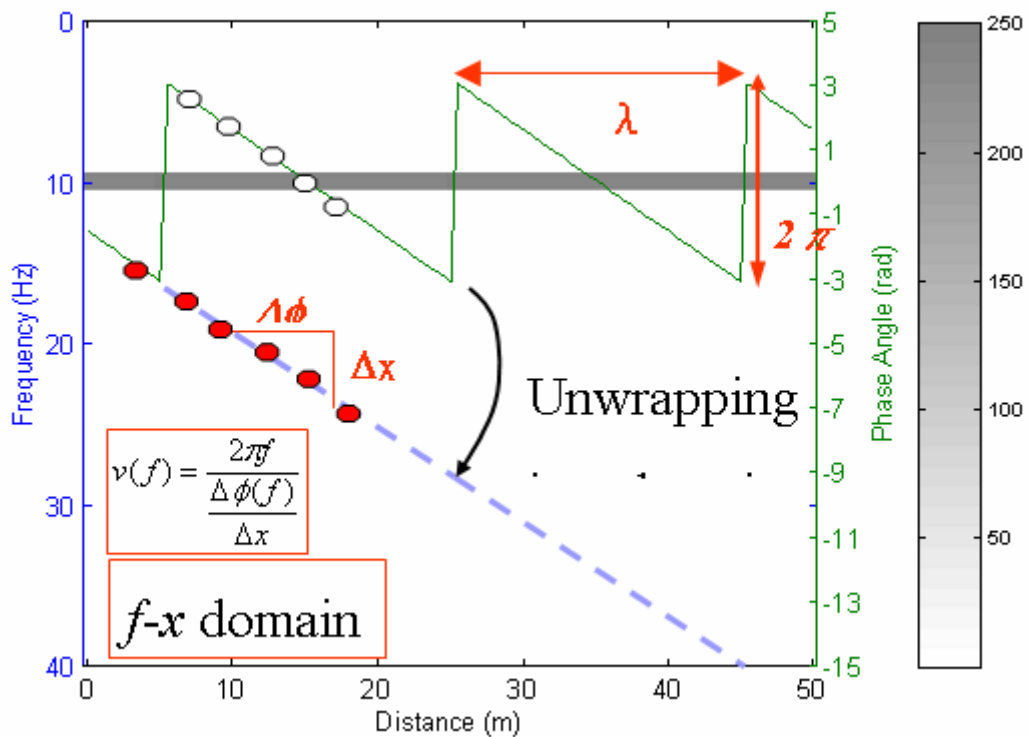


Fig. 4-1 The phase velocity and phase angle in  $f$ - $x$  domain

### 4.1.3 Phase Angles: Multi-station spectral analysis of surface wave (MSASW)

Similar to the SASW method, the frequency-offset data can provide the dispersion

relation from the difference of the phase angle. Due to the multi-channel records, the phase velocity can be directly estimated in  $\varphi$ - $x$  domain without making use of the cross-spectral density (CSD) of signals. The phase velocity in (2-55) can be rewritten in form of (4-7):

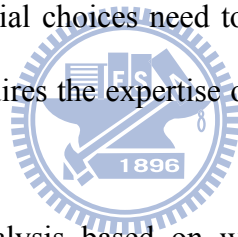
$$v(f_i) = \frac{2\pi f_i}{\frac{\Delta\phi(f_i)}{\Delta x}} \quad (4-7)$$

For any specific frequency  $f_i$ , the phase velocity depends on the increasing rate of phase angle with offset (i.e. the slope  $(\Delta\phi/\Delta x)$ ) in  $\varphi$ - $x$  domain by the definition of (4-7). As shown in Fig. 4-1, for a synthetic single frequency wave with  $f=10$  Hz and  $v=200$  m/sec, the phase angle in  $\varphi$ - $x$  domain oscillates only between  $\pi$  to  $-\pi$ . After unwrapping in  $\varphi$ - $x$  domain (not the phase angle of CSD in  $\varphi$ - $f$  domain in SASW), the slope can be estimated and the phase velocity of the specific frequency is obtained.

Estimations of the slopes  $(\Delta\phi/\Delta x)$  may also be affected by some inherent natural effects like near and far field effects, higher mode participation and ambient noises. The numerous samplings in space domain of the multi-channel record here provide some advantage. The slope  $(\Delta\phi/\Delta x)$  can be determined by the linear regression of the unwrapped  $\Delta\phi$ ; as shown in Fig. 4-1. The data quality at each sampling in space domain can be evaluated by the R-square statistic ( $R^2$ ) of the regression analysis. Using the image of real part and the energy spectrum of  $f$ - $x$  data, a technique, named “optimum offset range selection” (see detailed in Sec. 4.1.4), can be applied to screen out poor data before the regression of further dispersion analysis. The phase–offset regression is a multi-station extension of the SASW method, and is referred to as the multi-station spectral analysis of surface wave (MSASW) hereafter. The MSASW can provide a better credibility due to its numerous samplings in the space domain rather than two samplings of SASW.

It has been shown that errors may arise in experimental dispersion curves when usual SASW test and data analysis procedures are followed, in particular the phase unwrapping

procedure. Sources that contain significant energy in very low frequencies and receivers with very low natural frequency are necessary to avoid erroneous un-wrapping of phase angles at low frequencies. Hence, the data acquisition system of a SASW test is typically different from that of a refraction survey although they share many things in common. Unwrapping errors may occur for sites where, across the frequency range used, there is a shift from one dominant surface wave propagation mode to another, a phenomenon termed ‘mode jumping’. Furthermore, the use of only a pair of receivers leads to the necessity of performing the test using several testing configuration and the so-called common receiver midpoint geometry. For each receiver spacing, multiple measurements are necessary for evaluating the data coherence. This results in a quite time-consuming procedure on site for the collection of all the necessary data and on data reduction for combining the dispersion data points from records obtained at all spacings. Since many non-trivial choices need to be made based on the data quality and testing configuration, the test requires the expertise of an operator and automation of the data reduction is difficult.



Compared to dispersion analysis based on wavefield transformations, MSASW and SASW methods do not allow identification and separation of multiple modes. When tests are performed on complex strata with higher mode wave propagation, the effects of higher modes may result in non-linear  $\varphi(x)$  relation. The dispersion relation obtained from  $\varphi$ - $x$  regression is considered as an “effective” dispersion curve which means a combined result of dispersion curves of several different modes. Only in the case of applying the sufficiently long geophone spreading  $L$ , the phase velocity of the dominant mode can be found by the  $\varphi$ - $x$  relation. Thus, the MSASW is not to be used to replace 2-D wavefield transformation. It can be seen as a by-product and supplement of the unified dispersion analysis. The  $R^2$  of MSASW can be useful information for data quality and identification of existence of multiple modes.

A field case was demonstrated at a test site located at the court yard of Min Ann temple

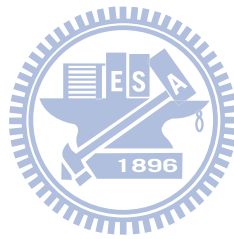
in Yuan Lin Township in middle Taiwan. Two spreads of 24 geophones were placed roughly perpendicular to each other, one array 23 m long ( $\Delta x = 1$  m) and the other 11.5 m long ( $\Delta x = 0.5$  m). A sledgehammer impacting on a steel plate was used as the seismic source, with a near offset 15 m.

Fig. 4-2 shows the results of the dispersion analysis for the short array. It is insightful to examine the surface wave data in various domains. In the time–space domain, the raw data of the shot gathers shows rich ground roll energy without much contamination of body wave or ambient noise (Fig. 4-2a). In the  $f$ - $x$  domain, the amplitude spectrum does not show much variation with offset because of the short array used (Fig. 4-2b). The linearity of the phase spectrum with respect to the offset is presented as the  $R^2$  of  $\varphi$ - $x$  regression analysis as shown in Fig. 4-2c. Low  $R^2$  values at low frequencies indicate the near field effect while low values at high frequencies reveal far field effect or mode jumping. In this case, the spectrum amplitude of high frequencies does not significantly decrease with increasing offsets. Hence, the low  $R^2$  values at high frequencies are signs of mode jumping or multiple dominant modes rather than far field effect. Fig. 4-2d shows the  $f$ - $\nu$  spectrum and the associated (maximum) peaks at each frequency. The results of the MSASW analysis are also shown in Fig. 4-2d. For short geophone arrays, separate peaks associated with adjacent modes may smear or even disappear because the spectrum main lobes associated with each mode interfere with each other due to leakage in the space domain. The frequencies at which the results of MSASW and  $f$ - $\nu$  spectrum are significantly different coincide with those frequencies with low  $R^2$  values. The differences are due to mode jumping (i.e. the phase–offset relation becomes nonlinear) and possibly further due to unwrapping errors resulting from noise or mode jumping. The experimental dispersion curve should approach the dominant mode for long geophone arrays. For short geophone array, as is in this case, the experimental dispersion curve may not represent the ‘true’ answer for any modes at frequencies where multiple modes dominate. In



this case, the inversion interpretation must be conducted considering the apparent phase velocity that is associated with mode superposition and the method of analysis.

The four-plot figure as shown in Fig. 4-2 can be obtained on site in a fraction of seconds automatically, making it a very powerful tool for data quality control in the field. Necessary adjustments to the testing program may be made immediately after the initial test. The results of the analysis of the adjusted geophone arrays (i.e. 23-m long array) are shown in Fig. 4-3. The experimental (apparent) dispersion curve becomes more representative of the dominant mode as the offset range increases. Furthermore, the  $f$ - $v$  spectrum clearly shows separate modes in this case.



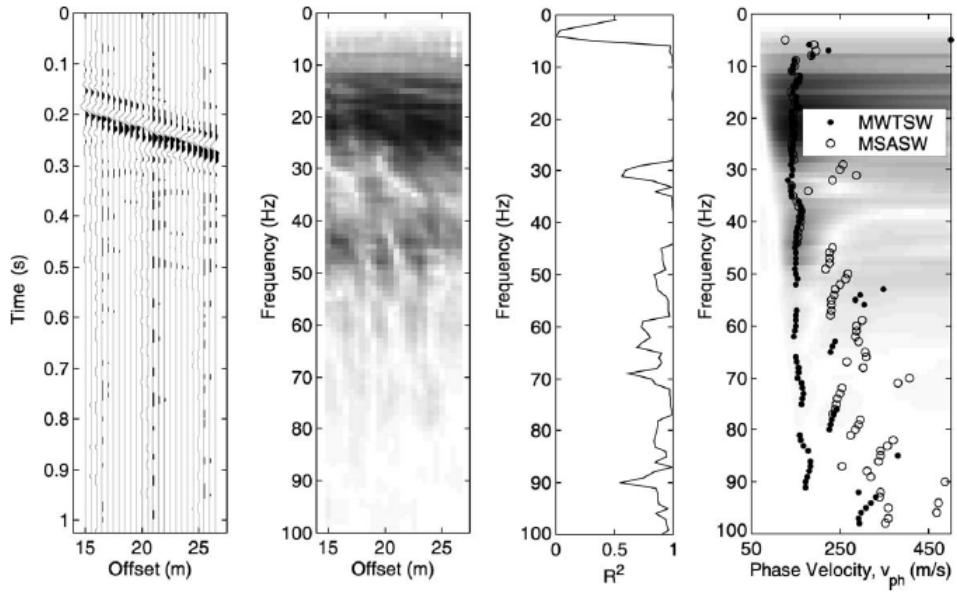


Fig. 4-2 Results of the dispersion analysis of the short array (11.5 m) at the verification test site  
 (a) raw data in the time–space domain, (b) amplitude spectrum in the frequency–space domain, (c)  $R^2$  statistics of the linear regression in the phase–space domain, and (d) amplitude spectrum in the  $f$ – $v$  domain.

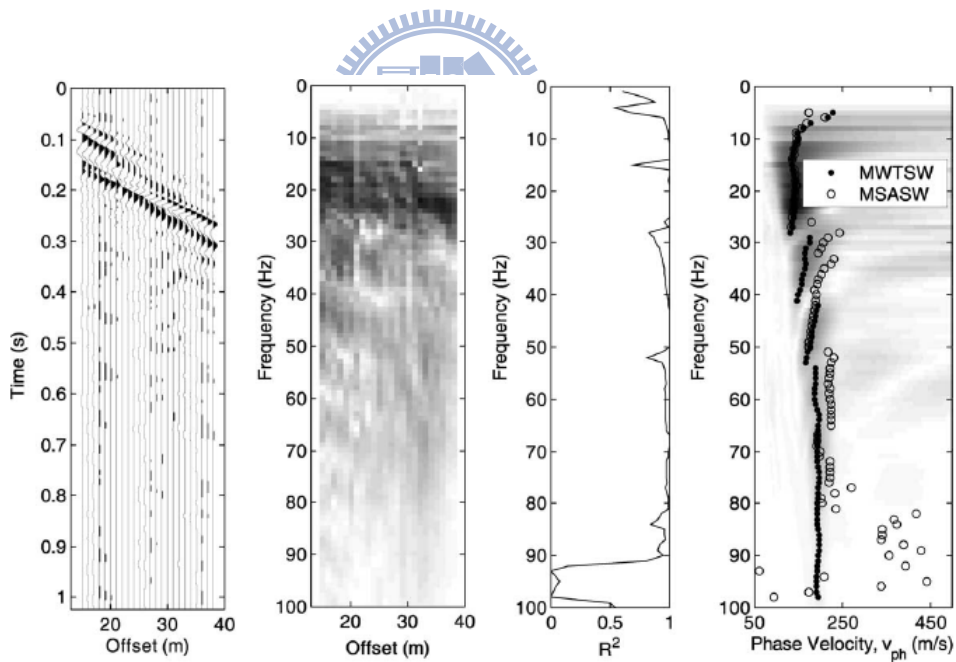


Fig. 4-3 Results of the dispersion analysis of the short array (23 m) at the verification test site  
 (a) raw data in the time–space domain, (b) amplitude spectrum in the frequency–space domain, (c)  $R^2$  statistics of the linear regression in the phase–space domain, and (d) amplitude spectrum in the  $f$ – $v$  domain.

#### 4.1.4 Amendment for near and far field effect: Optimum offset range selection

As mentioned in Sec.3.2.3 and Sec.3.3.3, the near and far field effects are inevitable for some frequency components no matter how the field configuration is adjusted. However it is still possible to identify the frequency and offset range that are contaminated by those effects and remove those contaminated data before dispersion analysis. The influence caused by near and far field effects can be traced in the different forms (the real or imaginary part, the phase angle and the energy spectrum) of  $f$ - $x$  complex data. The QC index,  $R^2$ , after a preliminary dispersion analysis by MSASW, can also reveal this information roughly too. This study proposes a technique named “optimum offset range selection” for reducing the near and far field effects and enhancing the signal quality. By inspecting the wave propagation pattern in the  $f$ - $x$  domain, areas with low S/N ratio or near and far field effects can be identified and an appropriate 2-D window of reduction coefficients in the  $f$ - $x$  domain can be applied to screen out poor data. The amendatory data with better signal quality can proceed for further dispersion analysis.

As shown in Fig. 3-12, the influences of the near and far field effects at a specific frequency can be clearly observed in the  $\varphi$ - $x$  domain in a pseudo-section record. Within a certain offset range, the unwrapped phase angle increases linearly. The non-linear part represents unexpected contamination caused by low S/N ratio, near, or far field effects. That is the major source of errors when estimating phase velocity by using MSASW method. The near and far field effects can be also observed via the real part of  $f$ - $x$  complex data. For the same pseudo-section record conducted at the Bao-Ai campus of NCTU, the components at  $f=31$  Hz and  $f=57$  Hz in the form of real part of  $f$ - $x$  complex data are shown in Fig. 4-4. For the frequency component  $f=31$  Hz, the aperiodic oscillation in the offset range  $x=0\sim 20$  m shows the influence of near field effect; for the frequency component  $f=57$  Hz, the aperiodic oscillation caused by the far field effect appears in the offset range  $x=25\sim 70$  m.

Fig. 4-5(a) shows the 2-D wiggle plot of the real part of the  $f$ - $x$  complex data converted from the pseudo-section record of tests conducted on the jobsite of Bao-Shan Second Reservoir as mentioned in Sec. 3.3.2. The plot clearly provides a guide to proceed with the optimum offset range selection. The optimum offset range is defined as the offset range where the sinusoidal wave pattern is clearly seen. For frequency <20 Hz, 20~40 Hz, 40~ 65 Hz and >65 Hz, the optimum offset ranges are 50~70 m, 25~70 m, 20~50 m and 1~20 m respectively. It can be predicted that the signals of 20~40 Hz possess best quality because the optimum offset range of this part takes a bigger portion of the total offset range.

When the optimum offset range is selected, only the signals within the range will be remained and others will be muted. To avoid the leakage problem arisen from the truncation, as mentioned in Sec. 3.1.2, some appropriate windowing need to be applied on the signals within the whole optimum offset range for further signal processing. There are plenty of such windowing functions, for example, Barlett, Blackman, Hamming, Hanning and Kaiser window. The following illustration uses the Hamming window. The amendatory  $f$ - $x$  complex data,  $\bar{U}(f_i, x_n)$ , can be written as

$$\bar{U}(f_i, x_n) = U(f_i, x_n)w(f_i, x_n) \quad (4-8)$$

in which,  $U(f_i, x_n)$  is the original  $f$ - $x$  complex data and the Hamming window function,  $w(f_i, x_n)$ , is,

$$w(f_i, x_n) = \begin{cases} 0.54 - 0.46 \cos[2\pi N_p / (L_p - 1)] & , 0 \leq N_p \leq (L_p - 1), \text{ within the optimum offset range} \\ 0 & , \text{ outside the optimum offset range} \end{cases} \quad (4-9)$$

in which,  $L_p$  is the total samples and  $N_p$  is the integer index to represent discrete points of the space domain within the optimum offset range. Based on (4-9), the amplitudes of the 2-D window in  $f$ - $x$  domain are as shown in Fig. 4-5(b). Fig. 4-5(b) is only a simple illustration. More smooth transitions in optimum offset selection at different frequencies can be done.

Fig. 4-6 show the two dispersion analyses performed on the Bao-Shan Second Reservoir data with and without optimum offset range selection. Both results show scattered energy in the  $f$ - $v$  domain. The clear and continuous pattern exists only for frequency between 20~40 Hz. It is consistent with the prediction on signal quality when selecting the optimum offset range. The dispersion curve after the optimum offset range selection (Fig. 4-6(a)) appears to be less scattered and provides more accurate results for MSASW and smoother results for MWTSW.

Another example is shown in Fig. 4-7 and Fig. 4-8 using the pseudo-section record of tests conducted on the jobsite of Tai-Bao City, Chia-Yi, Taiwan. The 2-D wiggle plot (in Fig. 4-7 (a)) of the real part of the  $f$ - $x$  complex data indicates that the optimum offset ranges are 22~90 m and 1~22 m for frequencies <35 Hz and >35 Hz respectively. The 2-D optimum offset range selection is shown in Fig. 4-7 (b). Fig. 4-8 shows the results of dispersion analyses with and without optimum offset range selection. It is obvious that the dispersion curve with the optimum offset range selection shows a more clear and continuous pattern than the one without the optimum offset range selection. Especially the case of MSASW method, the MSASW method is more sensitive to the optimum offset range selection because the estimation of the phase velocity in the MSASW method depends on the correctness of phase unwrapping and regression of the  $\varphi(x)$  relation.

The above two example demonstrate that presenting the test data in the  $f$ - $x$  domain provides powerful visual inspection for data quality. A suitable 2-D window can be applied in the  $f$ - $x$  domain to screen out unwanted data to enhance results of dispersion analysis. The 2-D windows used in this study are simple blocks in the  $f$ - $x$  domain. More smooth and sophisticated windows can be used.

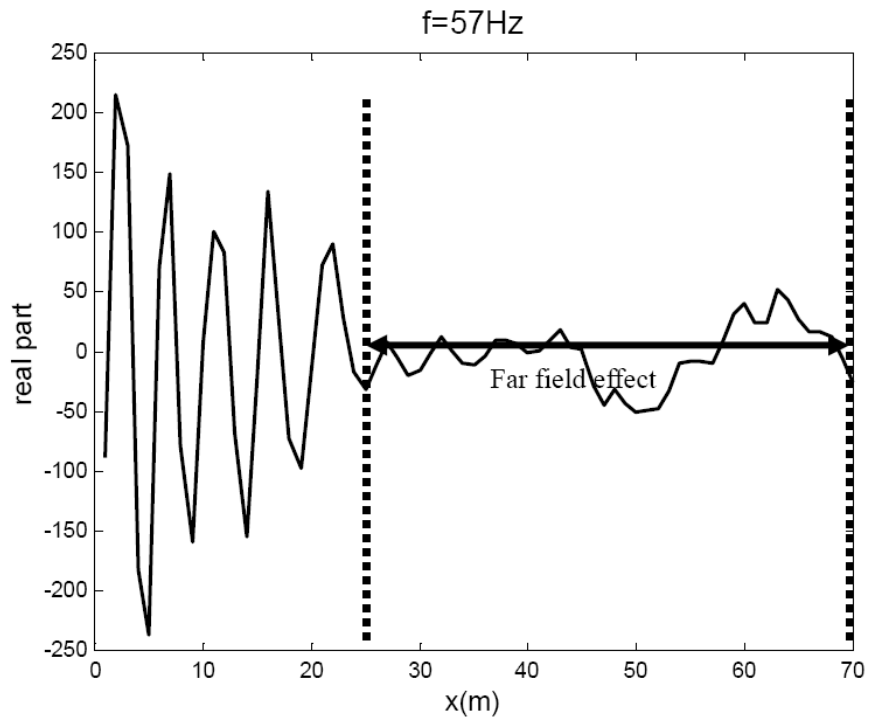
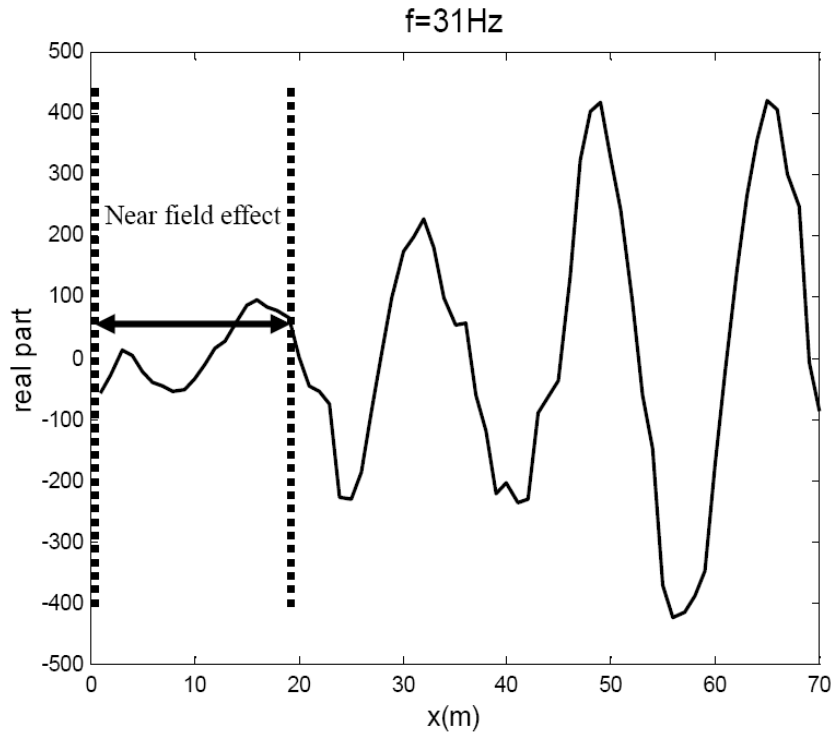
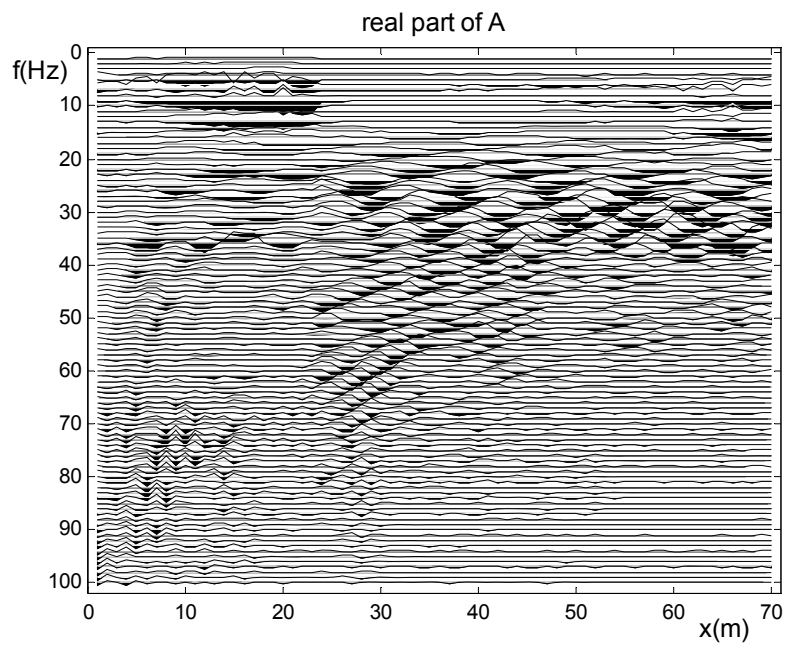
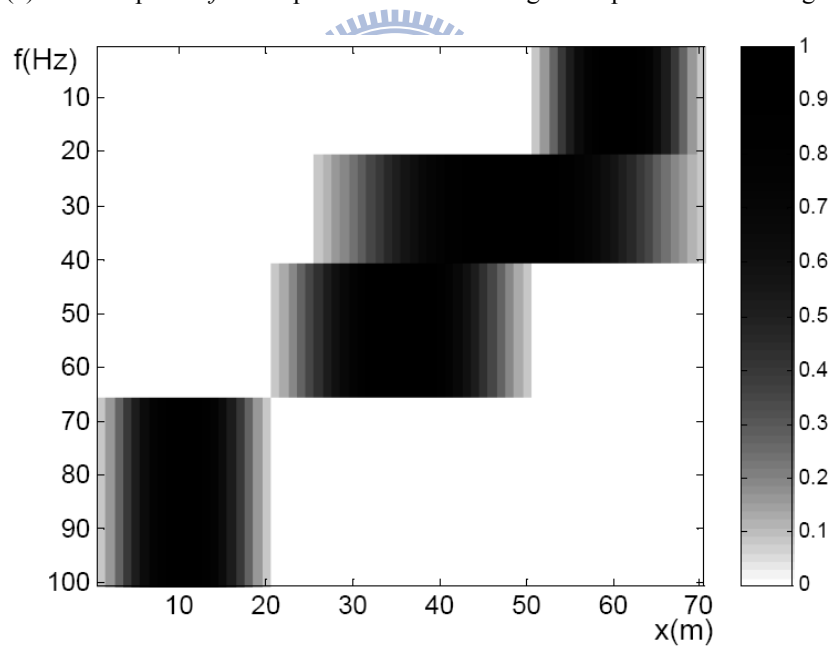


Fig. 4-4 Near and far field effects in the real part of  $f$ - $x$  complex data

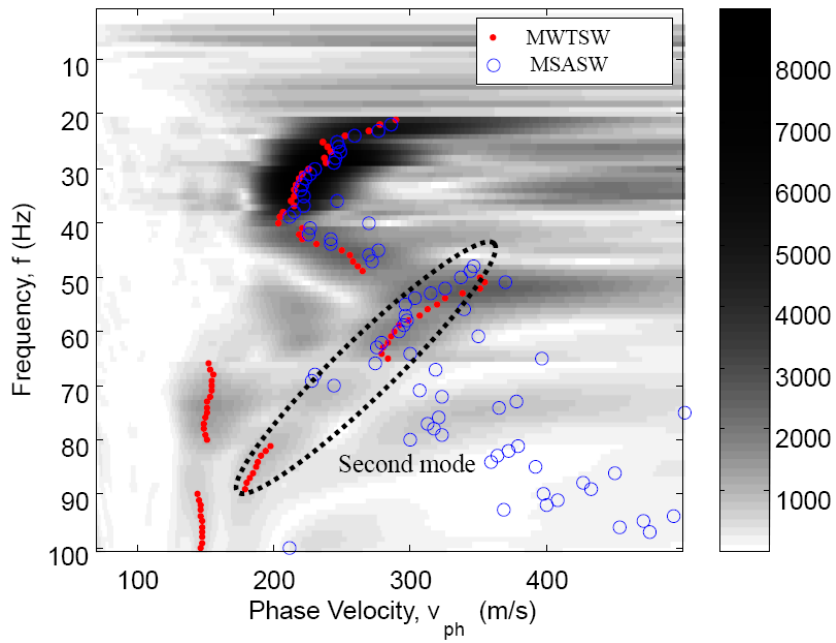


(a) The real part of  $f$ - $x$  complex data for observing the “optimum offset range”

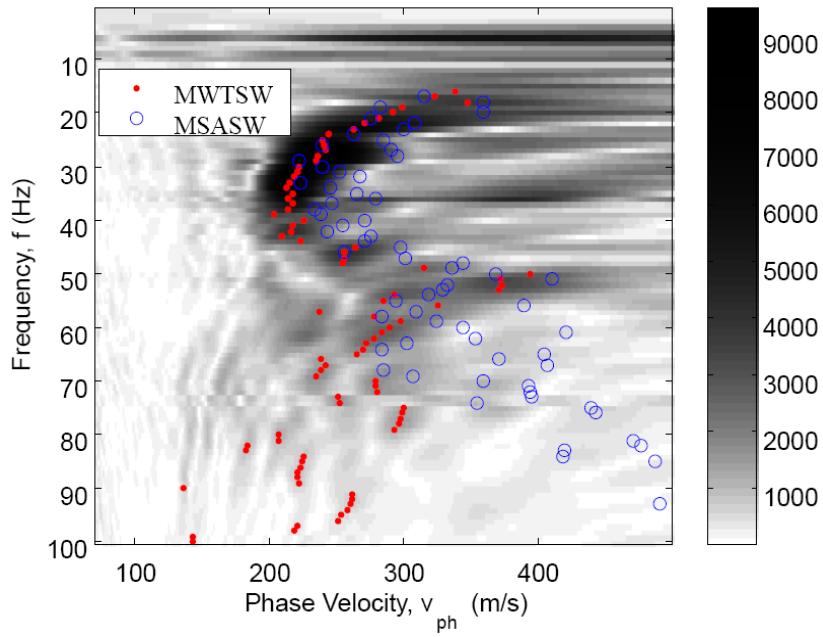


(b) The 2-D window of reduction coefficients produced by Hamming window after the “optimum offset range selection”

Fig. 4-5 Testing records in Bao-Shan second reservoir for “optimum offset range selection”



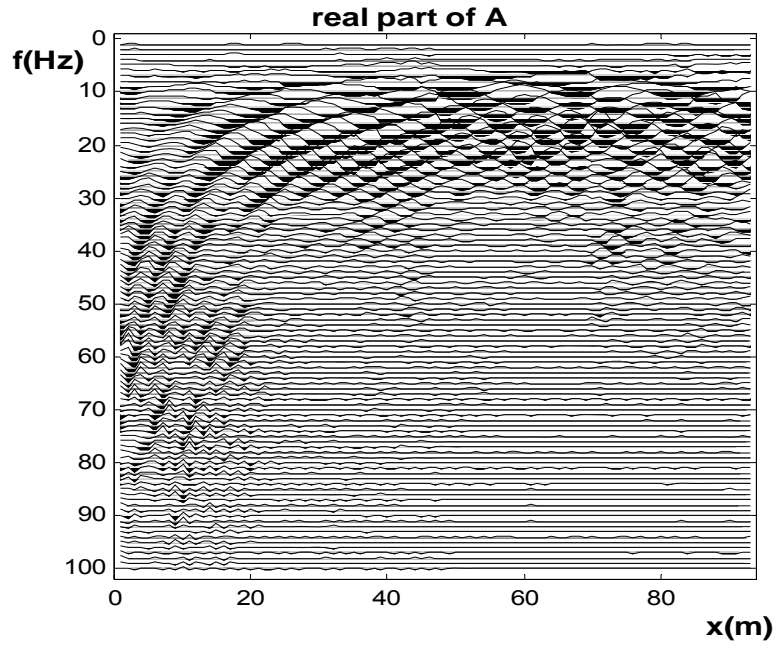
(a) Dispersion curves by MSASW and wavefield transformation after “optimum offset range selection”



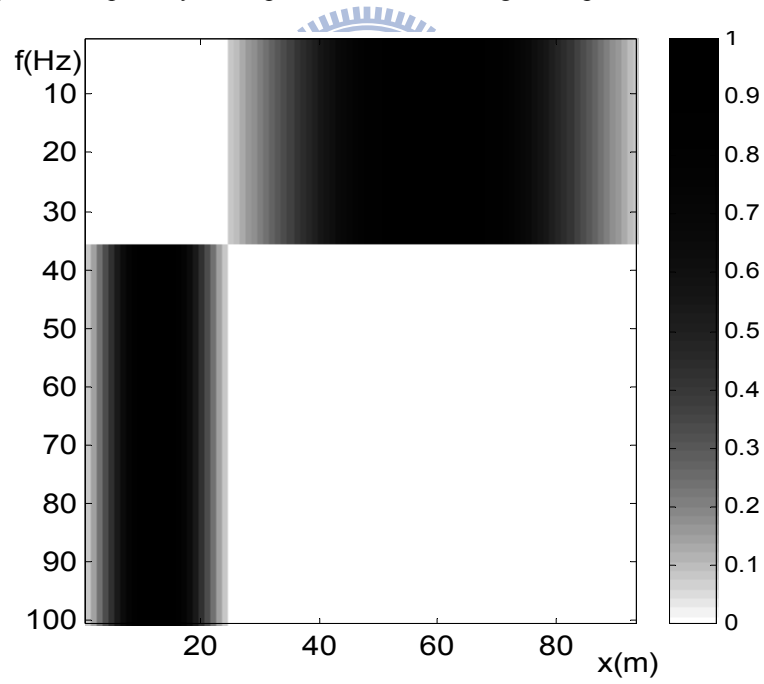
(b) Dispersion curves by MSASW and wavefield transformation before “optimum offset range selection”

Fig. 4-6 The dispersion curves and  $f$ - $v$  spectrum of tests in Bao-Shan second reservoir



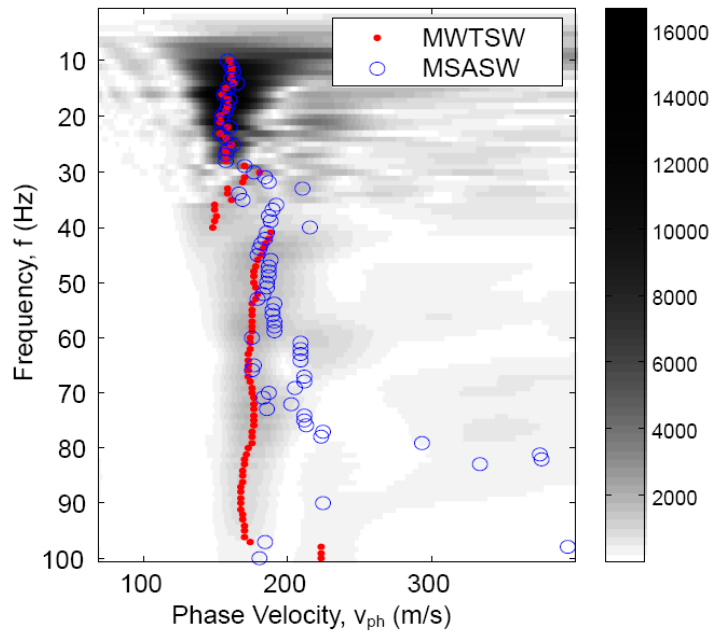


(1) The real part of  $f$ - $x$  complex data for observing the “optimum offset range”

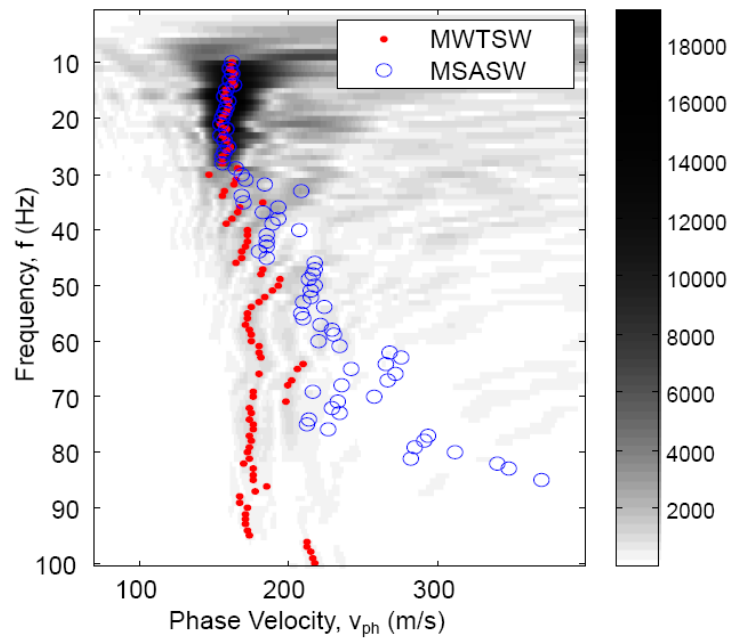


(2) The 2-D window of reduction coefficients produced by Hamming window after the “optimum offset range selection”

Fig. 4-7 Testing records in Tai-Bao City for “optimum offset range selection”



(1) Dispersion curves by MSASW and wavefield transformation after “optimum offset range selection”



(2) Dispersion curves by MSASW and wavefield transformation before “optimum offset range selection”

Fig. 4-8 The dispersion curves and  $f$ - $v$  spectrum of tests in Tai-Bao City

## 4.2 Unified Wavefield Transformation (UWFT)

### 4.2.1 Different transformations and presentations of space domain

Following the first DFT in the time domain, the unified procedure proceeds with another Fourier Transform with respect to the space on the complex  $f$ - $x$  data. For each frequency component, the wavefield is a harmonic function of space. The wavenumber  $k$  (i.e. spatial frequency) can be determined from the wavenumber analysis (spectral analysis in space) as mentioned in Chapter 2,. The wavenumber analysis in the space domain of the multi-station signals can be performed using the discrete-space Fourier Transform, which has already been seen as (2-57):

$$Y(f_i, k) = \sum_{n=0}^{N-1} U(f_i, x_n) \exp(-jkx_n) \quad (4-10)$$

where  $Y(f_i, k)$  represents the wavefield in the frequency-wavenumber ( $f$ - $k$ ) domain. The wavenumber ( $k$ ) of the surface wave can be identified at the peaks of the amplitude spectrum of  $Y(f_i, k)$ . The phase velocity is then determined by the definition  $v = 2\pi f/k$ .

Note again, the resolution in the  $k$  domain needs to be enhanced due to limited samples in space domain. On the aspect of signal processing, a common way for enhancing the spatial resolution is to add zero-value traces after the raw data. However the algorithm presented here applies the discrete-space Fourier Transform in space domain. The discrete-space Fourier Transform is different from the discrete Fourier Transform in that the wavenumber remains continuous but the fast algorithm (FFT) cannot be used.

Chapter 2 has also reviewed other different transformations ( $p$ - $f$  and  $f$ - $v$ ) to analysis the dispersion curves in different domains. An alternative method is proposed here to obtain the same results. The characteristics of wavefield in different domains will then be studied and a unified dispersion analysis is proposed.

Using change of variables, the wavefield in different domains can be obtained by

substituting the relations between other variables and the wavenumber in the  $f$ - $k$  transformation.

➤ The wavefield in the frequency- phase velocity ( $f$ - $v$ ) domain

The relation between phase velocity ( $v$ ) and wavenumber ( $k$ ) is:

$$v = \omega/k = 2\pi f/k \Rightarrow k = 2\pi f/v \quad (4-11)$$

Substituting (4-11) into (4-10), the  $f$ - $v$  analysis, wavefield in the  $f$ - $v$  domain, can be expressed as:

$$Y(f_i, v) = \sum_{n=0}^{N-1} U(f_i, x_n) \exp\left(-j 2\pi f_i / v x_n\right) \quad (4-12)$$

where  $Y(f_i, v)$  represents the wavefield in the frequency-velocity ( $f$ - $v$ ) domain

➤ The wavefield in the frequency- slowness ( $f$ - $p$ ) domain

The relation between slowness ( $p$ ) and wavenumber ( $k$ ) is:

$$p = 1/v = k/\omega = k/2\pi f \Rightarrow k = 2\pi f p \quad (4-13)$$

Substituting Eqs. (4-13) into Eqs. (4-10), the  $f$ - $p$  analysis, wavefield in the  $f$ - $p$  domain, is expressed as:

$$Y(f_i, p) = \sum_{n=0}^{N-1} U(f_i, x_n) \exp(-j 2\pi f_i p x_n) \quad (4-14)$$

where  $Y(f_i, p)$  represents the wavefield in the frequency-slowness ( $f$ - $p$ ) domain

➤ The wavefield in the frequency- wavelength ( $f$ - $\lambda$ ) domain

For the frequency-wavelength ( $f$ - $\lambda$ ) domain, the relation between slowness ( $\lambda$ ) and wavenumber ( $k$ ) is:

$$k\lambda = 2\pi \Rightarrow k = 2\pi/\lambda \quad (4-15)$$

Substituting Eqs. (4-15) into Eqs. (4-10), the  $f$ - $\lambda$  analysis, wavefield in the  $f$ - $\lambda$  domain, is expressed as:

$$Y(f_i, \lambda) = \sum_{n=0}^{N-1} U(f_i, x_n) \exp(-j 2\pi/\lambda x_n) \quad (4-16)$$

where  $Y(f_i, \lambda)$  represents the wavefield in the frequency-wavelength ( $f$ - $\lambda$ ) domain.

According to (4-10)~(4-16), the amplitude spectra of the 2-D wavefield in  $f$ - $k$ ,  $f$ - $\nu$ ,  $f$ - $p$  and  $f$ - $\lambda$  domains can be obtained simultaneously straight from the 2-D Fourier Transformation without any other signal processing algorithm. Due to its directness and commonality, this algorithm is called “Unified Wavefield Transformation (UWFT)”.

#### 4.2.2 Characteristics of wavefield transformation in different domains

To examine the validity of UWFT and have a comprehensive understanding on the patterns of the energy spectra in different domains, some synthetic wavefields were generated from superposition of multiple harmonic waves and surface wave simulations of selected velocity profiles (normally dispersive and irregularly dispersive).

The first case is a 2-D wavefield generated by superposing several different sinusoidal vibrations. It can be written as:

$$u(t, x) = \sum_{i=1}^n \sin(\omega_i t - k_i x) \quad (4-17)$$

where  $u(t, x)$  is the synthetic wavefield,  $\omega_i$  and  $k_i$  are the angular frequency and wavenumber of the  $i^{th}$  mode of vibrations respectively.

The simplest normally dispersive case consists of two layers of horizontal strata. The phase velocity (or mechanical constants) of the layered strata increases with depth. Under this situation, the fundamental mode is dominant throughout the entire frequency range. Normally dispersive cases are typically seen normally sedimentary geological environment in which softer sedimentary materials overlay harder materials or bed rocks. The irregularly dispersive

case simulated in this study is a softer sandwich layer existing in the middle of a homogeneous half space. Under such a condition, the higher modes may dominate in some frequencies. The synthetic wavefields and modal dispersion curves of strata used in this study are generated by a set of computer programs released by Professor R.B. Herrmann at Saint Louis University (USA).

For the parametric study of field parameters, the synthetic wavefields are generated with different sampling interval ( $\Delta x$ ) and geophone spread ( $L$ ). The characteristics of energy spectra in different domains are discussed. Furthermore the derived dispersion curves in their original domains are converted into the common wavelength-velocity ( $\lambda$ - $v$ ) domain. In the  $\lambda$ - $v$  domain, it is clear to see the differences between results from different transformations. The dispersion curve in the  $\lambda$ - $v$  domain is analogous to the depth-velocity profile and provides easier interpretation for the dispersion relation.

➤ Superposition of multiple harmonic waves

The different modes of vibrations contributing a synthetic 2-D wavefield are listed in Table 3.1 . The sampling interval and numbers in time domain are  $\Delta t=0.005$  sec and  $M=2048$  respectively and the minimum offset  $X_0$  is 1m. In Sec. 3.2, the  $f$ - $k$  spectrum of the wavefiled is used as an example to illustrating the aliasing and leakage problem as shown as Fig. 3-3 and Fig. 3-4.

Fig. 4-9 shows the 2-D spectra extracted from the wavefield with sampling interval  $\Delta x=1$  m and geophone spread  $L=1024$  m. the results demonstrate the effectiveness of the UWFT algorithm. It should be noted that the  $k$ ,  $\lambda$ ,  $v$  or  $p$  domain are uniformly discretized. While the two modes at  $f=20$  Hz can be clearly seen in  $f$ - $k$ ,  $f$ - $p$  and  $f$ - $v$  domains, they do not differ much in wavelength and may not be clearly seen if wavelength resolution is not high enough.

Fig. 4-10 shows the 2-D spectra with the same geophone spread  $L=1024$  m but increased

sampling interval  $\Delta x=16$  m to illustrate the effect of aliasing. The aliasing is periodic in  $k$  domain but the repetition interval is not a constant in other domain ( $\lambda$ ,  $v$  and  $p$ ).

Fig. 4-11 shows the 2-D spectra with the sampling interval  $\Delta x=1$  m but decreased geophone spread  $L=256$  m to illustrate the effect of truncation. As expected, shorter truncation makes the lobes of energy spectra wider in all domains. The aliasing and leakage in different domains will be further examined in the case of surface wavefields from velocity profiles.

➤ The normally dispersive case

Table 4.1 Constants of the normally dispersive cases

| Layer | Depth (m) | $\rho$ (g/cm <sup>3</sup> ) | $V_S$ (cm/sec) | $V_P$ (cm/sec) |
|-------|-----------|-----------------------------|----------------|----------------|
| 1     | 0~-10     | 1.80                        | 300            | 600            |
| 2     | -10~-∞    | 1.80                        | 400            | 800            |

The 2-layer velocity profiles of normally dispersive cases are listed in Table 4.1. The sampling interval and numbers in time domain are  $\Delta t=0.002$  sec and  $M=1024$  respectively and the minimum offset  $X_0$  is 1m. The depths of the interface of discontinuity are GL-10m

The three different synthetic wavefields are generated based on different geophone spacing ( $\Delta x=1$ m and 4m) and geophone spread ( $L=128$ m and 48m) to illustrate the effects of aliasing and leakage in different domains. The theoretical and experimental dispersion curves in four different domains ( $f-k$ ,  $f-\lambda$ ,  $f-v$  and  $f-p$  domains) and those converted into the  $\lambda-v$  domain are shown in Fig. 4-12, Fig. 4-13 and Fig. 4-14.

In the case with field parameters of the geophone spacing  $\Delta x=1$ m and spread  $L=128$ m (Fig. 4-12), the experimental dispersion curves from all transformations agree well with the fundamental mode of the theoretical dispersion curve except few samplings in the very low or

high frequency part.

In the cases which the geophone spacing  $\Delta x$  increases up to 4m (Fig. 4-13), as expected, there are additional energy concentrations (aliasing patterns) due to aliasing. As discussed earlier, at a certain frequency, the aliasing is periodic in the  $k$  domain. So in the  $f-k$  domain the fundamental dispersion curve has a similar pattern as its aliases. In other domain ( $f-\lambda$ ,  $f-\nu$  and  $f-p$ ), the aliasing pattern is quite different from the dispersion curve. So with some background information, it is easier to identify the real dispersion curve in  $f-\lambda$ ,  $f-\nu$  and  $f-p$  domains when there are some aliasing. In the case when the geophone spread  $L$  decreases down to 24m (Fig. 4-14), the spectral energy is less concentrated in all four domains. The experimental dispersion curves are still distinguishable. But estimated velocity is less accurate for larger wavelengths.

➤ The irregularly dispersive case

Table 4.2 Constants of the irregularly dispersive cases

| Layer | Depth (m)   | $\rho$ (g/cm <sup>3</sup> ) | $V_S$ (cm/sec) | $V_P$ (cm/sec) |
|-------|-------------|-----------------------------|----------------|----------------|
| 1     | 0~4         | 1.80                        | 300            | 600            |
| 2     | 4~8         | 1.80                        | 250            | 500            |
| 3     | 8~ $\infty$ | 1.80                        | 400            | 800            |

The 3-layer velocity profiles of the irregularly dispersive case are listed in Table 4.2. The synthetic seismic data are also generated with the same geophone spacings and spreads for the effects of aliasing and leakage in the irregularly dispersive case. The simulated results are shown in Fig. 4-15, Fig. 4-16 and Fig. 4-17.

In the case with  $\Delta x=1\text{m}$  and  $L=128\text{m}$  (Fig. 4-15), the experimental dispersion curves from all four transformations agree with the theoretical values. Except the fundamental mode,



the higher modes are clearly distinguished for components with frequency  $> 40$  Hz. In the case with a longer geophone spacing  $\Delta x=4\text{m}$  (Fig. 4-16), the dispersion curve is hard to be identified due to the seriously effects by aliasing. In the case with the short geophone spread ( $L=24\text{m}$ , Fig. 4-17), the energy is less concentrated but the experimental dispersion curve is still able to be identified. However the higher modes are not separated and it may causes serious errors in the inversion. Except the influence in the investigated depth, as mentioned in Chapter 3, the geophone spread  $L$  also decides the ability of mode separation.



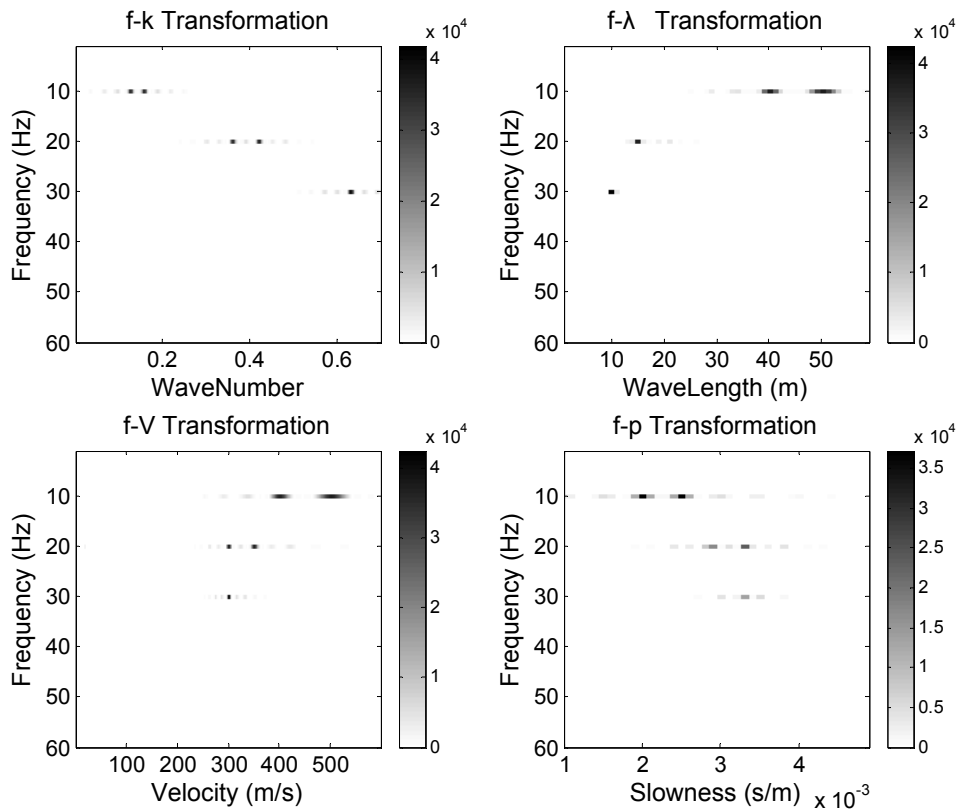


Fig. 4-9 The energy spectra of the wavefield of simple mode superposition ( $\Delta x = 1\text{m}$ ,  $L = 1024\text{m}$ )

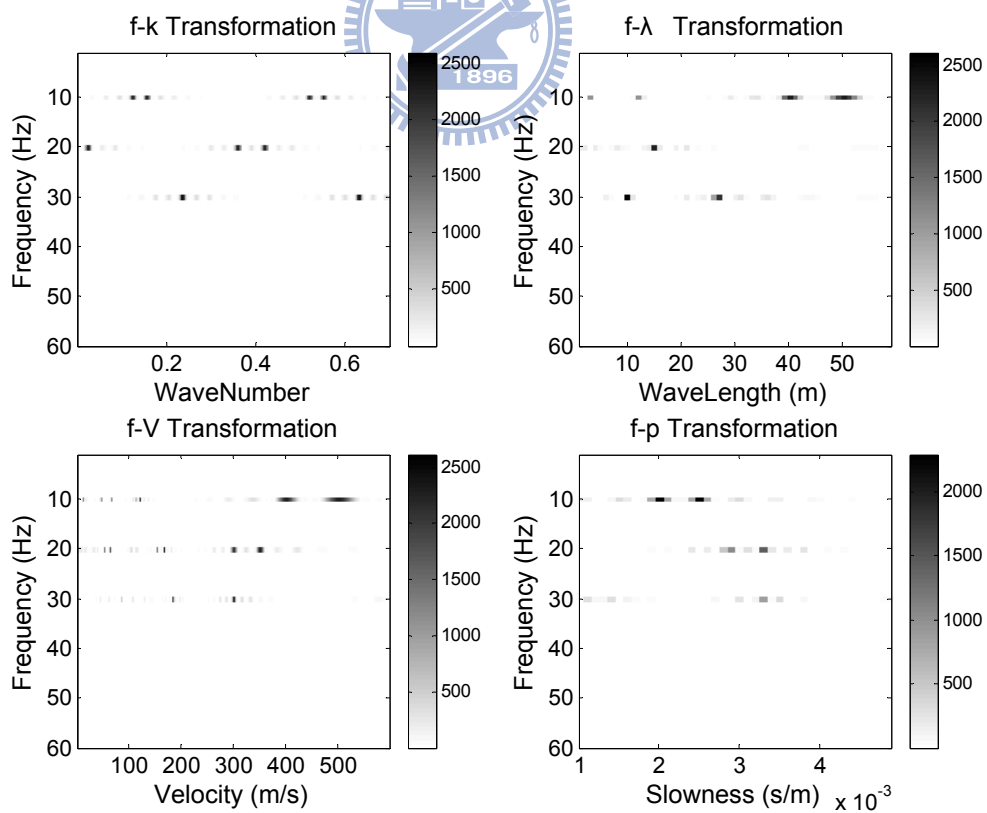


Fig. 4-10 The energy spectra of the wavefield of simple mode superposition ( $\Delta x = 16\text{m}$ ,  $L = 1024\text{m}$ )

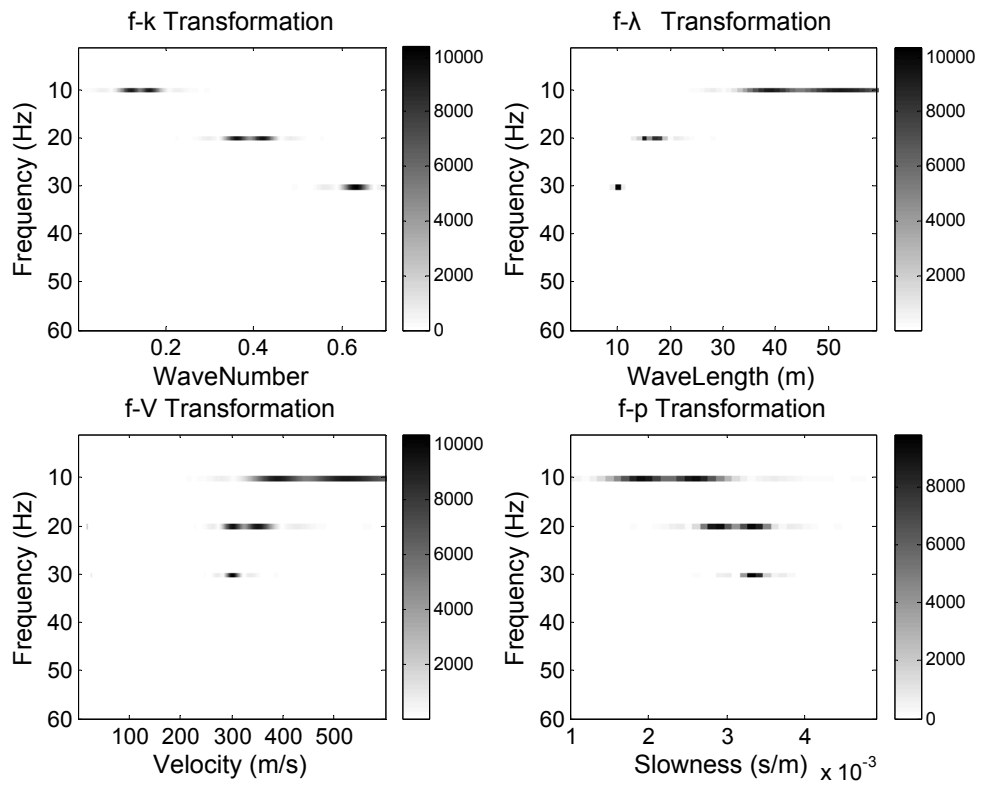
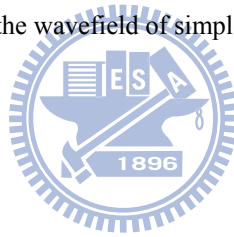
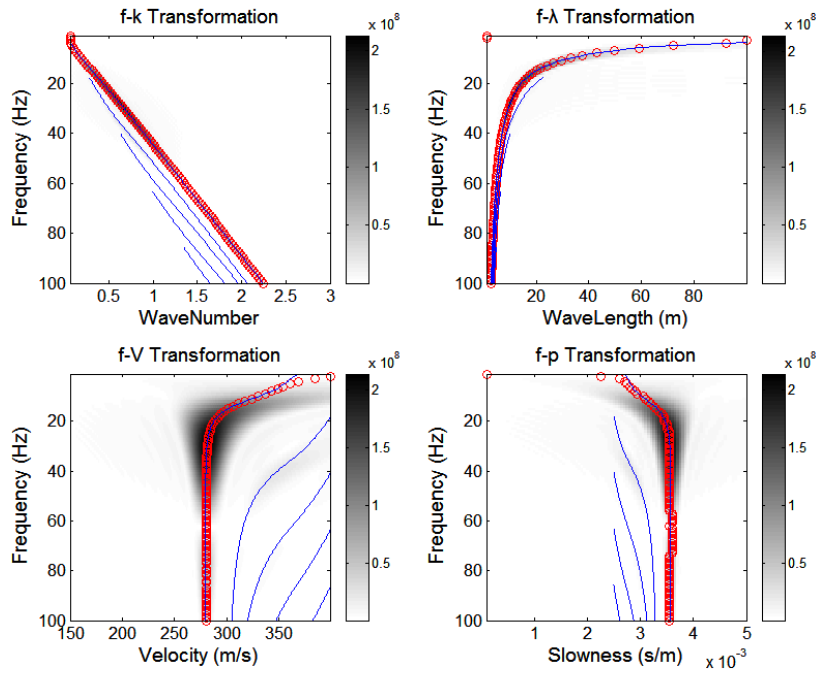
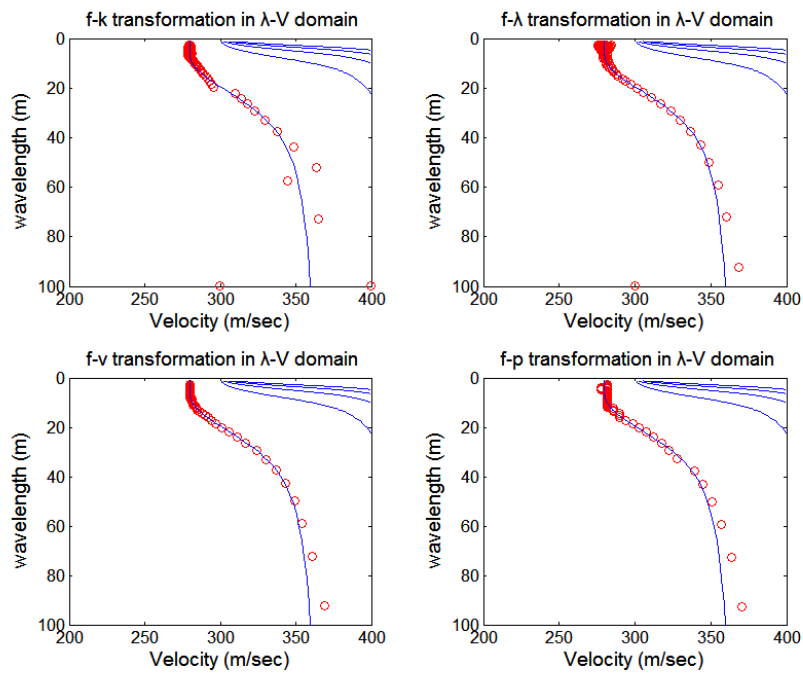


Fig. 4-11 The energy spectra of the wavefield of simple mode superposition ( $\Delta x = 1\text{m}, L = 256\text{m}$ )





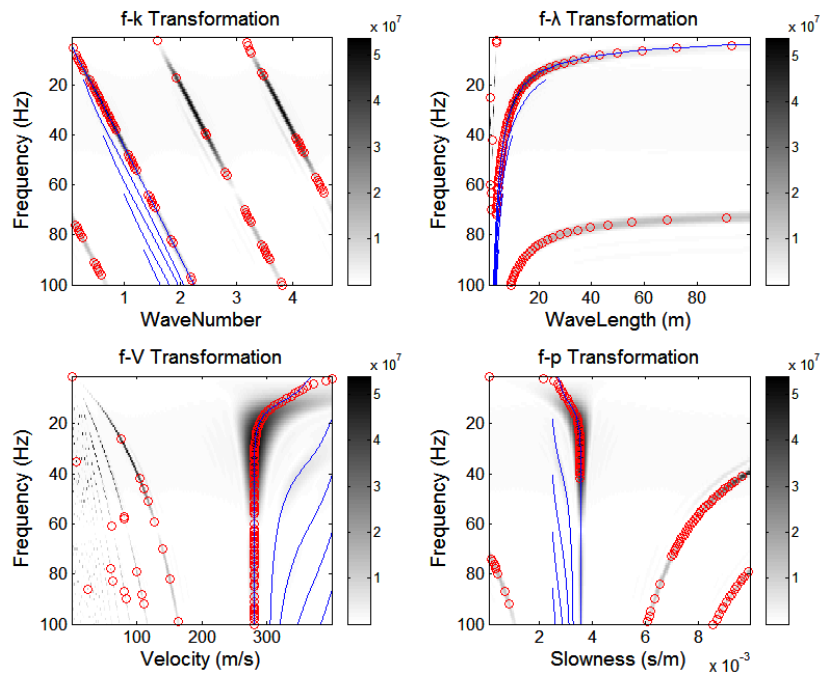
(a) The f-k, f- $\lambda$ , f-v and f-p domains



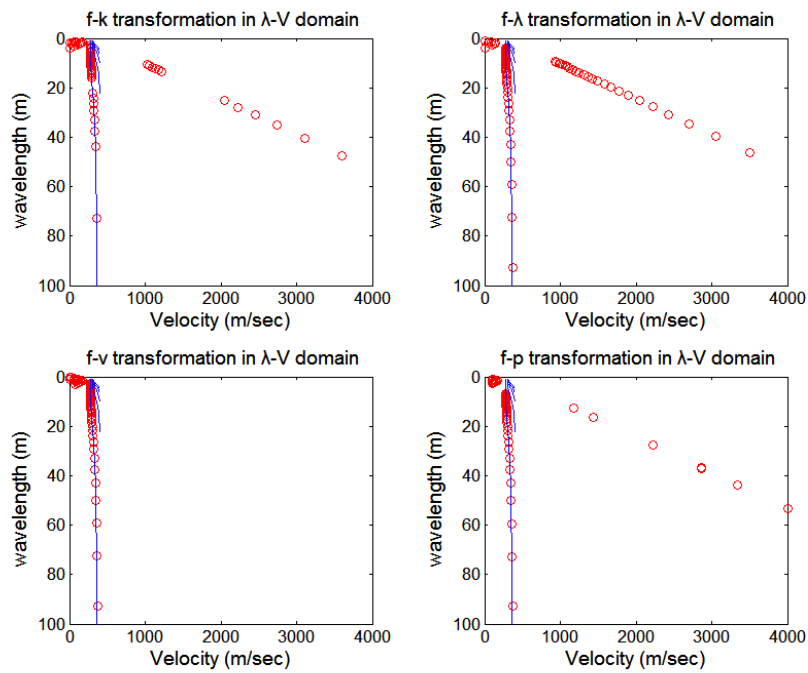
(b) The  $\lambda$ -v domain

Fig. 4-12 The energy spectra and dispersion curves (Normally dispersive case,  $\Delta x = 1\text{m}, L = 128\text{m}$ )

(Line: theoretical curves; Circle: experimental curves)



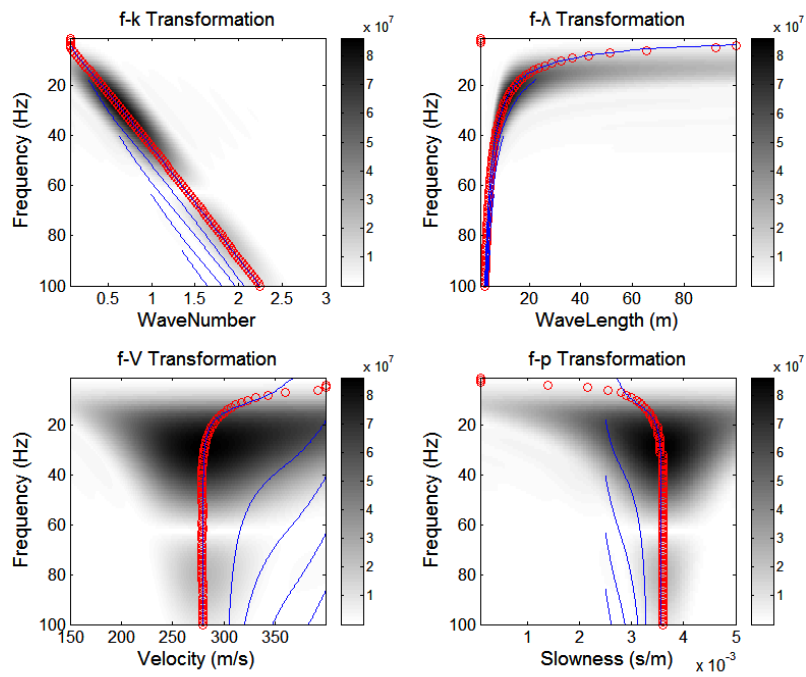
(a) The f-k, f-λ, f-v and f-p domains



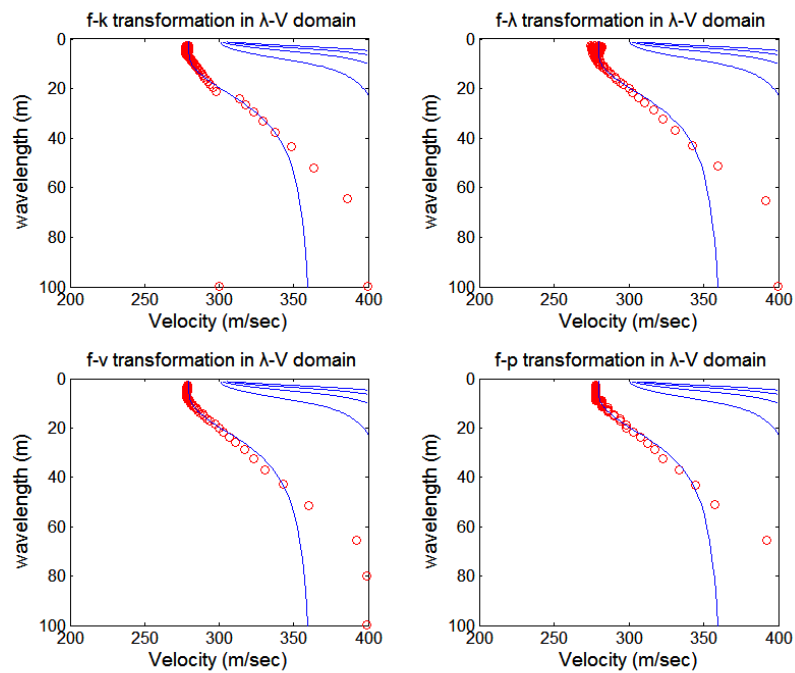
(b) The  $\lambda$ -v domain

Fig. 4-13 The energy spectra and dispersion curves (Normally dispersive case,  $\Delta x = 4m, L = 128m$ )

(Line: theoretical curves; Circle: experimental curves)



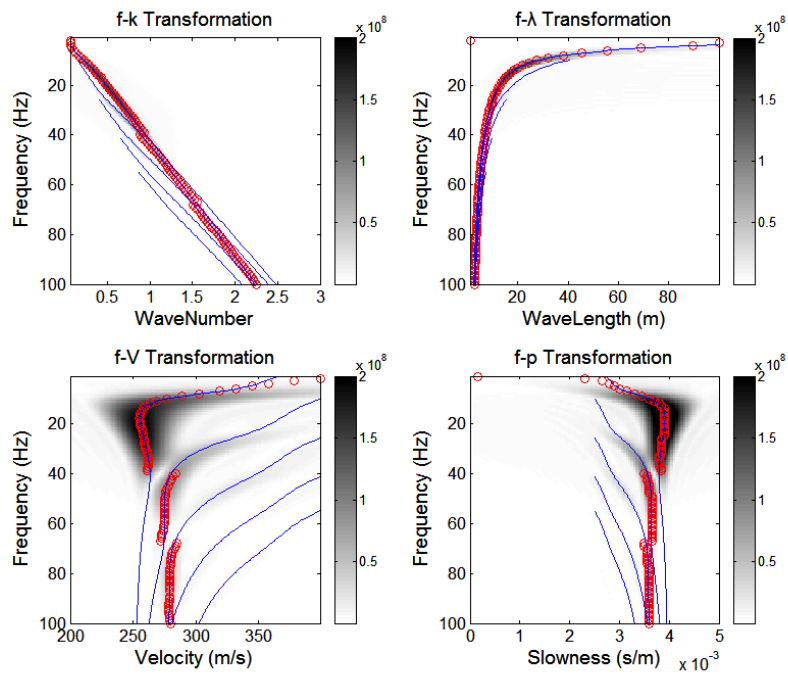
(a) The f-k, f-λ, f-v and f-p domains



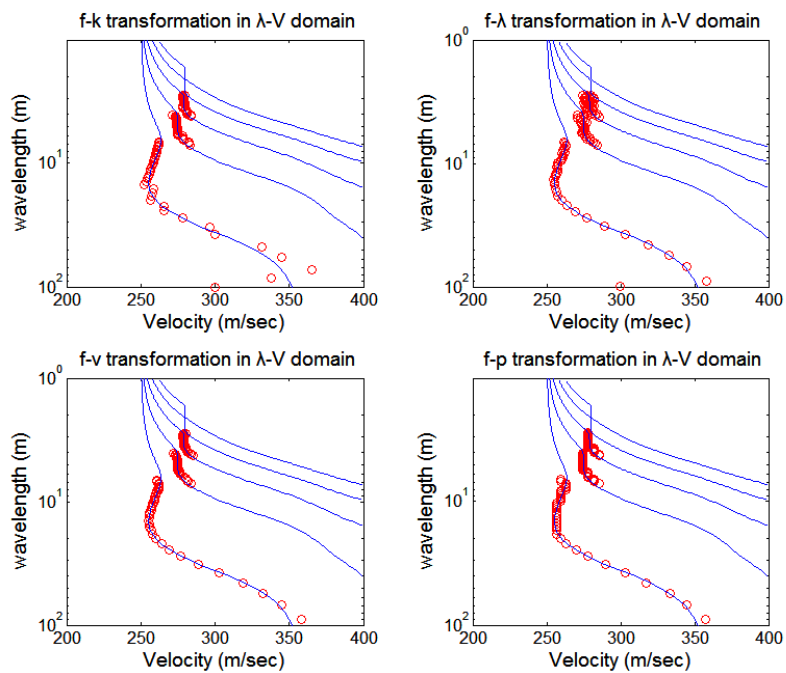
(b) The λ -v domain

Fig. 4-14 The energy spectra and dispersion curves (Normally dispersive case,  $\Delta x = 1m, L = 24m$ )

(Line: theoretical curves; Circle: experimental curves)



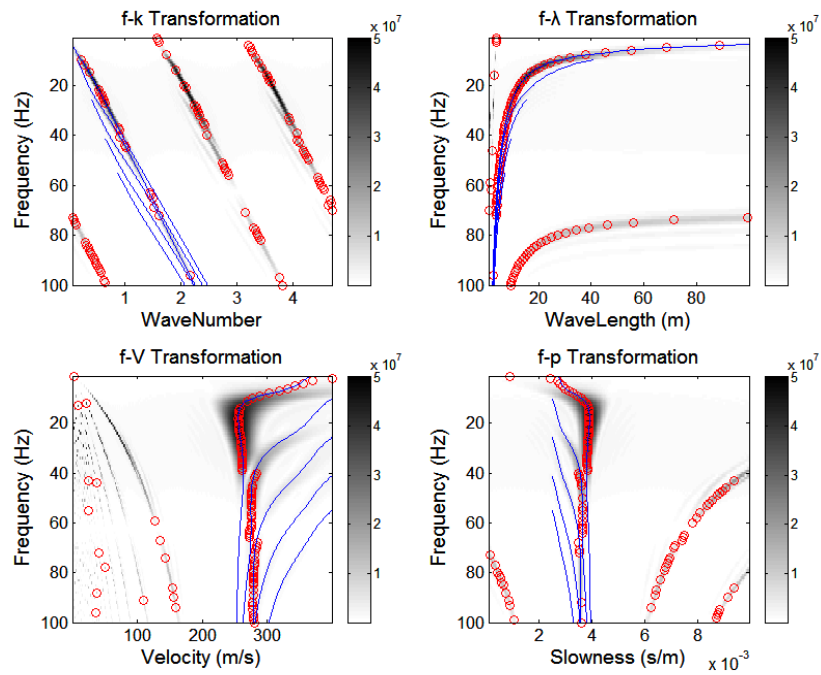
(a) The f-k, f- $\lambda$ , f-v and f-p domains



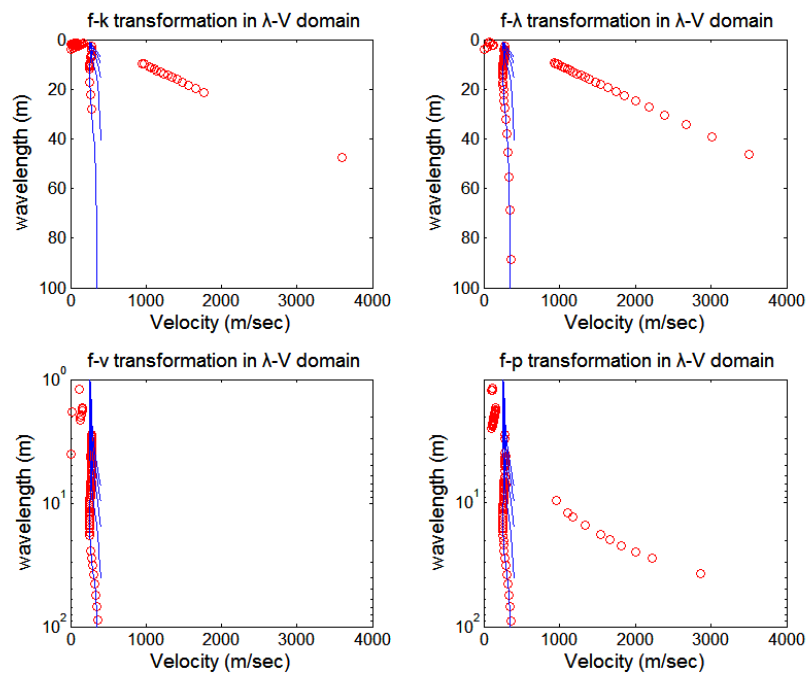
(b) The  $\lambda$ -v domain (log scale in  $\lambda$  domain)

Fig. 4-15 The energy spectra and dispersion curves (Irregularly dispersive case (A),  $\Delta x = 1\text{m}, L=128\text{m}$ )

(Line: theoretical curves; Circle: experimental curves)



(a) The f-k, f- $\lambda$ , f-v and f-p domains

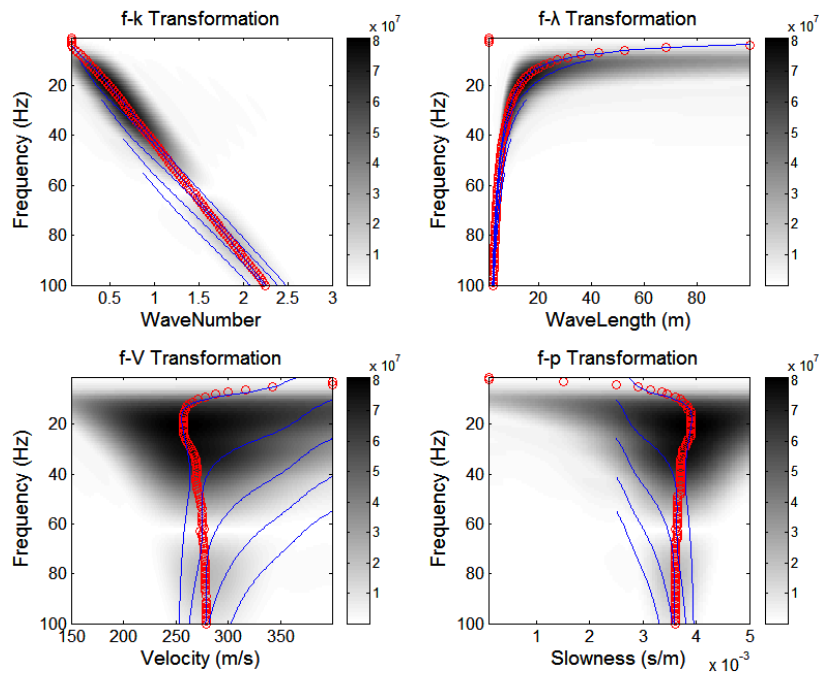


(b) The  $\lambda$ -v domain (log scale in  $\lambda$  domain)

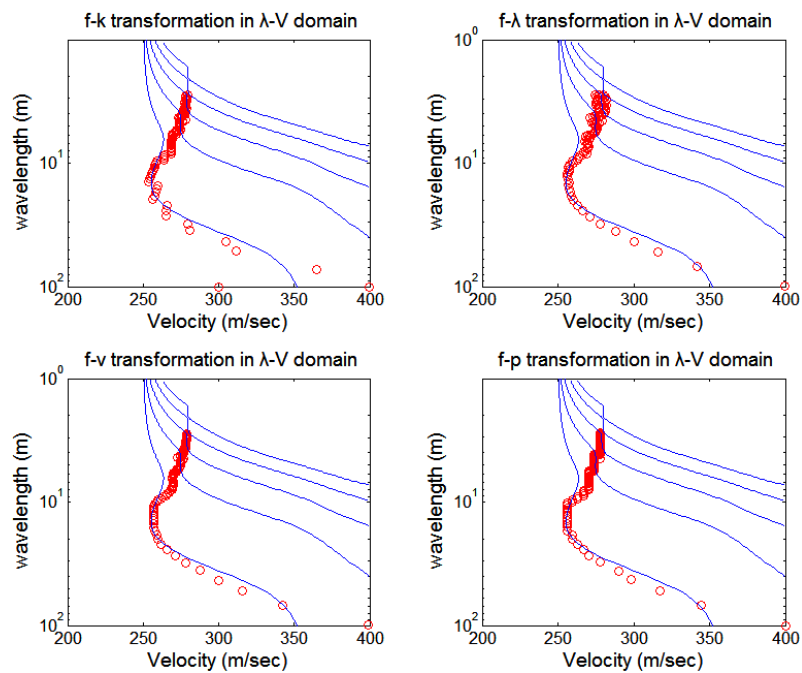
Fig. 4-16 The energy spectra and dispersion curves (Irregularly dispersive case,  $\Delta x = 4\text{m}, L = 128\text{m}$ )

(Line: theoretical curves; Circle: experimental curves)





(a) The  $f-k$ ,  $f-\lambda$ ,  $f-v$  and  $f-p$  domains



(b) The  $\lambda-v$  domain (log scale in  $\lambda$  domain)

Fig. 4-17 The energy spectra and dispersion curves (Irregularly dispersive case,  $\Delta x = 1\text{m}$ ,  $L = 24\text{m}$ )

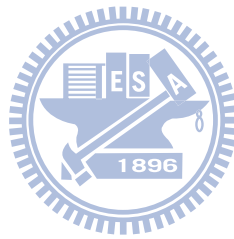
(Line: theoretical curves; Circle: experimental curves)

### 4.2.3 Optimization of dispersion analysis

Although UWFT provides a unified algorithm to obtain energy spectra in different domains, differences may still appear among the dispersion curves derived from transformations in different domains. To visual inspect the difference and investigate the causes, a dispersion analysis shown in Fig. 4-13 was repeated with coarser resolution on  $k$ ,  $\lambda$ ,  $\nu$  and  $p$  domain. The synthetic wavefield is based the strata profile as shown in Table 4.1. The field parameters  $\Delta x$  and  $L$  are 1m and 24m respectively. The discretization interval in  $f$ ,  $k$ ,  $\lambda$ ,  $\nu$  and  $p$  domain are  $\Delta f=1$  Hz,  $\Delta k=0.1$ ,  $\Delta \nu=40$  m/sec,  $\Delta \lambda=4$ m and  $\Delta p=0.0005$  sec/m. The results of dispersion analysis by UWFT are shown in Fig. 4-18. It can be seen that the dispersion curves from different transformations are all discontinuous and fractionalized into several fragments due to discretization in the  $f$ - $k$ ,  $f$ - $\lambda$ ,  $f$ - $\nu$  and  $f$ - $p$  transformation. Transforming the four dispersion curves into the  $\lambda$ - $\nu$  domain, the results in Fig. 4-19 clearly demonstrates how discretization in different domains can affect the resolution of dispersion analysis. In reality,  $k$ ,  $\lambda$ ,  $\nu$  and  $p$  are continuous quantities. They are discretized to make computation and perform efficient signal processing. But the discretization is not necessary if the discrete space Fourier Transform is used. Such that,  $k$ ,  $\lambda$ ,  $\nu$  and  $p$  can remain continuous. The peak of the amplitude spectrum can be located by an optimization algorithm. At any specific frequency, the dispersion curve is located at where the amplitude is the highest in the 2-D wavefield transformation spectra. The amplitude peaks can be searched by and optimization algorithm. The optimal point (peak) is not limited to one of the discrete point in conventional 2-D wavefield transformations.

As shown in Fig. 4-20, after optimal picking, the dispersion curves from different transformations become smooth and match well with the theoretical dispersion curve. The optimization algorithm used here is the Nelder-Mead method applied by the built-in function of Matlab software. Transforming the dispersion curves into the  $\lambda$ - $\nu$  domain, the result in Fig.

4-21 demonstrates that all dispersion curves from different transformations are identical. This optimal picking of dispersion curve completes the unified procedure of the UWFT. It should be noted that the deviation from the theoretical dispersion curve at larger wavelength in Fig. 4-21 is due to the geophone spread. Correct estimation of dispersion curve can be extended to larger wavelength by increasing the geophone spread ( $L$ ) as shown in Fig. 4-22.



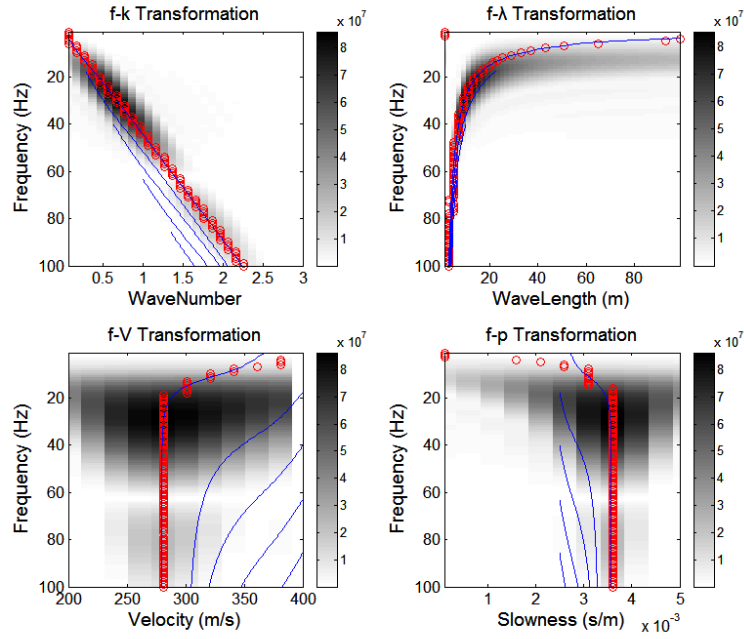


Fig. 4-18 The f-k, f- $\lambda$ , f-v , f-p spectrum and dispersion curves before Optima Picking

( $\Delta f=1$  Hz,  $\Delta k=0.1$ ,  $\Delta v=20$  m/sec,  $\Delta \lambda=2$ m,  $\Delta p=0.0005$  sec/m)

(Line: theoretical curves; Circle: experimental curves)

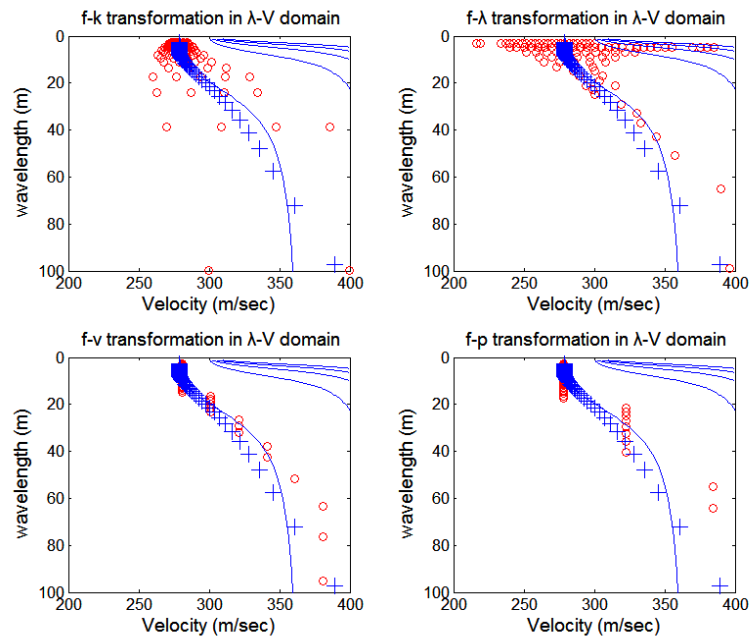


Fig. 4-19 The dispersion curves in  $\lambda$ -v domain before and after Optima Picking

(Line: theoretical curves; Circle: experimental curves before Optima Picking; Plus sign: experimental curves after Optima Picking)

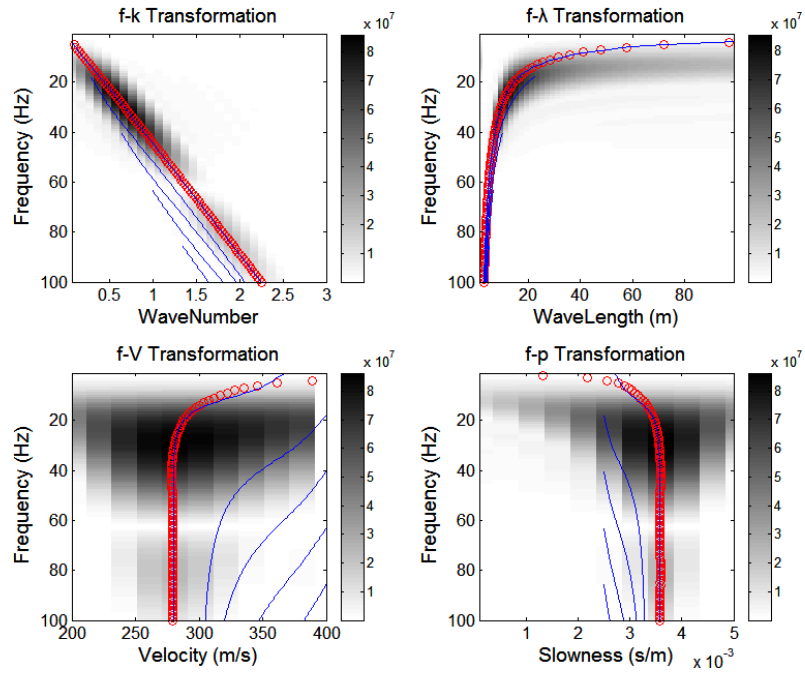


Fig. 4-20 The f-k, f-λ, f-v, f-p spectrum and dispersion curves after Optima Picking

(Line: theoretical curves; Circle: experimental curves)

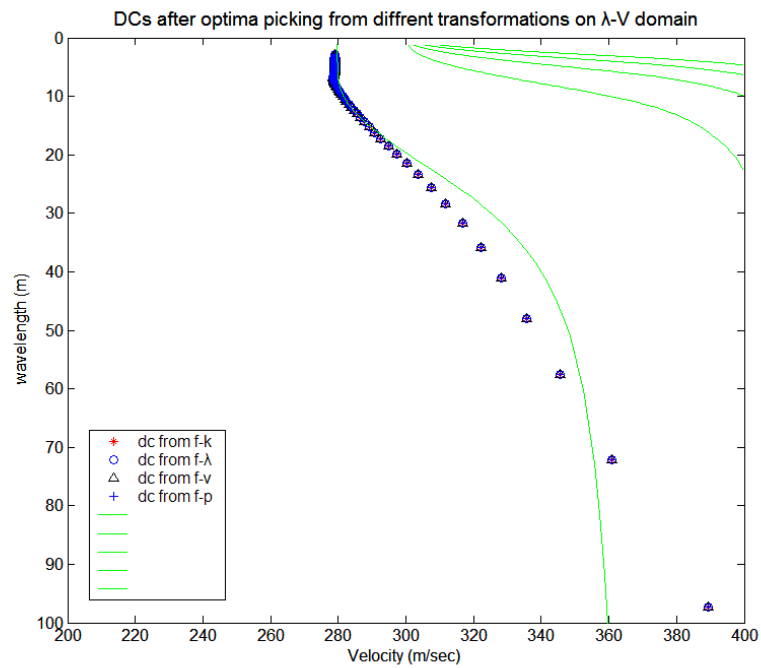


Fig. 4-21 Identical results form different transformations after optima picking in  $\lambda$ -v domain

(Line: theoretical curves; other symbols: experimental curves)

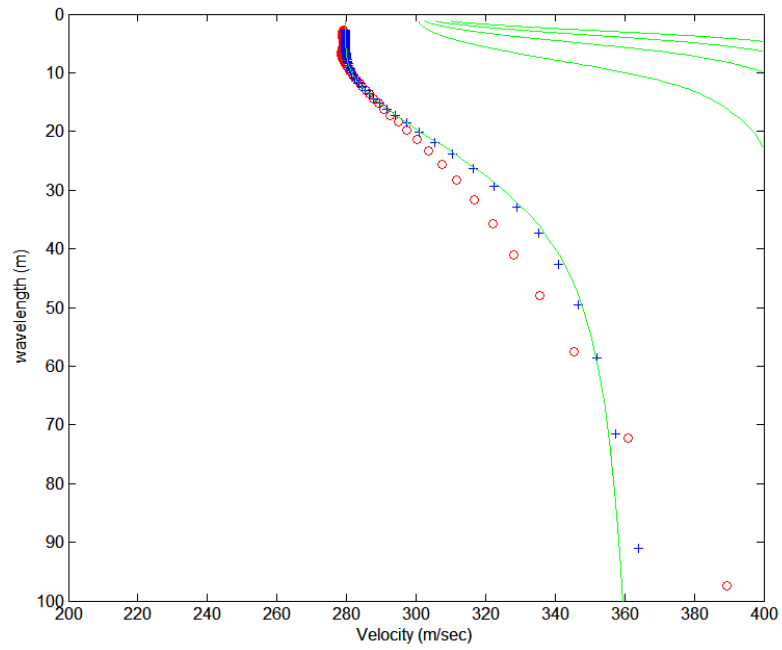
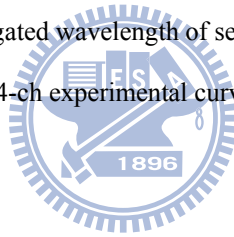


Fig. 4-22 Inherent limit on investigated wavelength of seismograms due to the length of survey line  
 (Line: theoretical curves; Circle: 24-ch experimental curves; Plus sign: 128-ch experimental curves)



### 4.3 Data sampling of dispersion curve

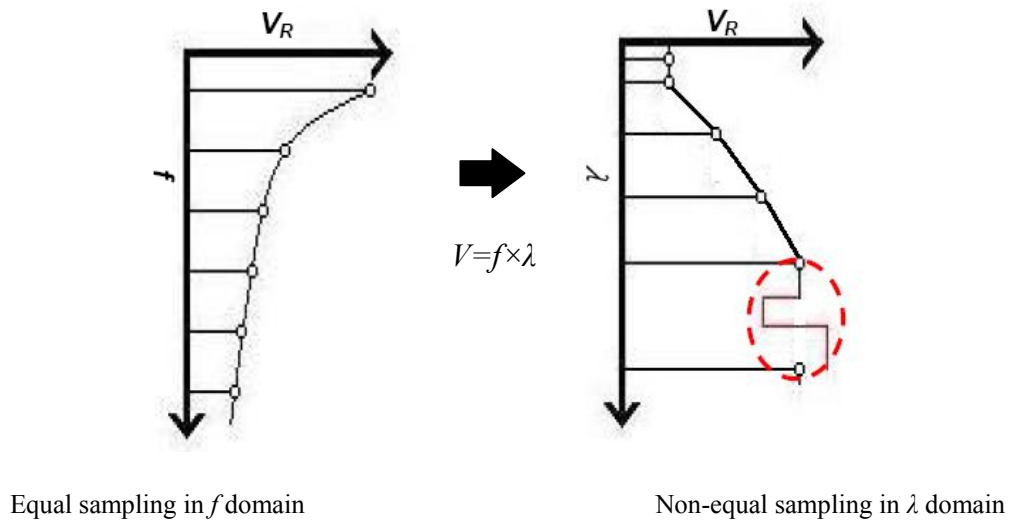


Fig. 4-23 Dispersion curve by equal sampling in  $f$  domain

For the dispersion analysis of MASW, the last step is always to pick the dispersive curve in the amplitude spectrum of 2-D wavefield transformation by searching the peak location of the transformed domain of the space for each frequency. Since the Fourier Transform with respect to time is usually performed by the FFT algorithm, the sampling points of frequency is uniform. When converting the equal-frequency sampling point of the dispersion curve into the  $\lambda$ - $v$  domain. It is obvious that most sampling points of dispersion curves are concentrated in the shorter wavelengths (<20m). The equal-frequency sampling causes the information of larger wavelengths (which implies larger depth) possibly neglected as shown in Fig. 4-23. Analogous to the resolution of the transformed domain of the space (i.e.  $k$ ,  $\lambda$ ,  $v$ , and  $p$ ), the equal-frequency sampling may not provide sufficient resolution in the low frequency part of the frequency domain.

A wavelength-controlled sampling is proposed here to improve the resolution in the sampled wavelength. A dispersion curve is first estimated at equally-spaced frequencies. The desired wavelengths (e.g. equal wavelength spacing) are decided and the corresponding

frequencies in the dispersion curve can be estimated by interpolation. These frequencies may not be found in the FFT discrete frequencies. As discussed in the previous section, although the recorded time-space wavefield is discrete, the 2D wavefield transformation remain continuous in theory (i.e.  $f$ ,  $k$ ,  $p$ ,  $v$ , and  $\lambda$  are continuous quantities). Therefore, the wavefield data of these wavelength-controlled frequencies may be obtained by the discrete-time Fourier transform (DTFT). Although it is much less efficient than FFT, the use of DTFT is justified by the fact that an experimental dispersion curve typically requires only limited number of frequencies. The dispersion analyses are performed again following the same UWFT procedure and optimal picking of the spectral peaks.

To demonstrate the above approach, the dispersion analyses are repeated for the normally dispersive case presented in Sec.4.2.2. The results are shown in Fig. 4-24. In this case, approximate equal wavelength samplings of the dispersion curve are achieved. It is out of the scope of the current study to investigate the sensitivity of surface waves to variation of velocity profile. The advantage of wavelength-controlled dispersion analysis should be further investigated. For example, future studied may be carried out to see whether a thin layer at deeper depth can be detected with higher resolution in long wavelengths.



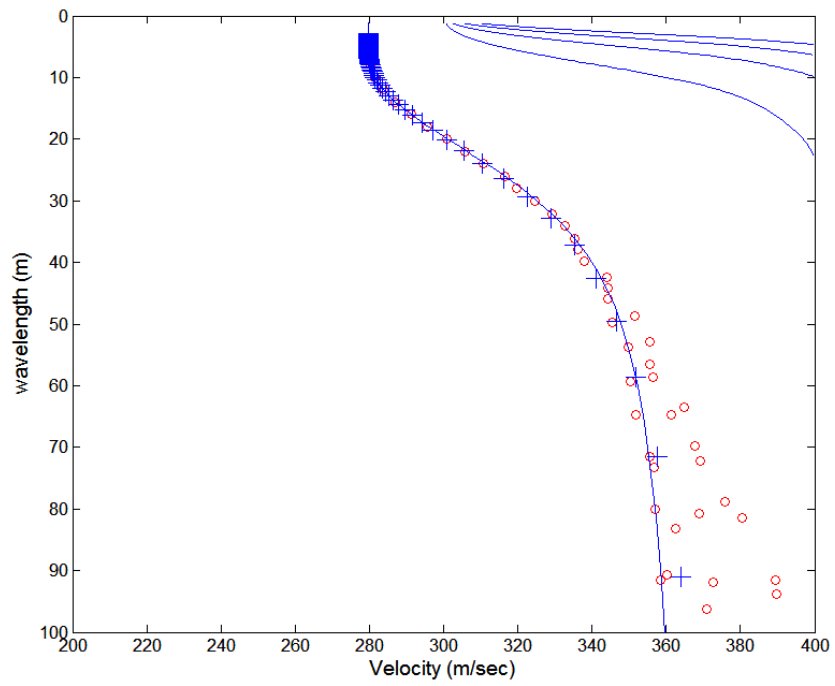
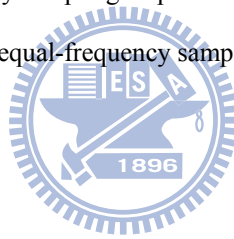


Fig. 4-24 Non equal-frequency sampling dispersion curves (2-layer model with  $L=128\text{m}$ )

(1) Line: theoretical (2) Circle: non equal-frequency sampling (3) Plus sign: equal-frequency sampling



## 4.4 The proposed standard dispersion analysis

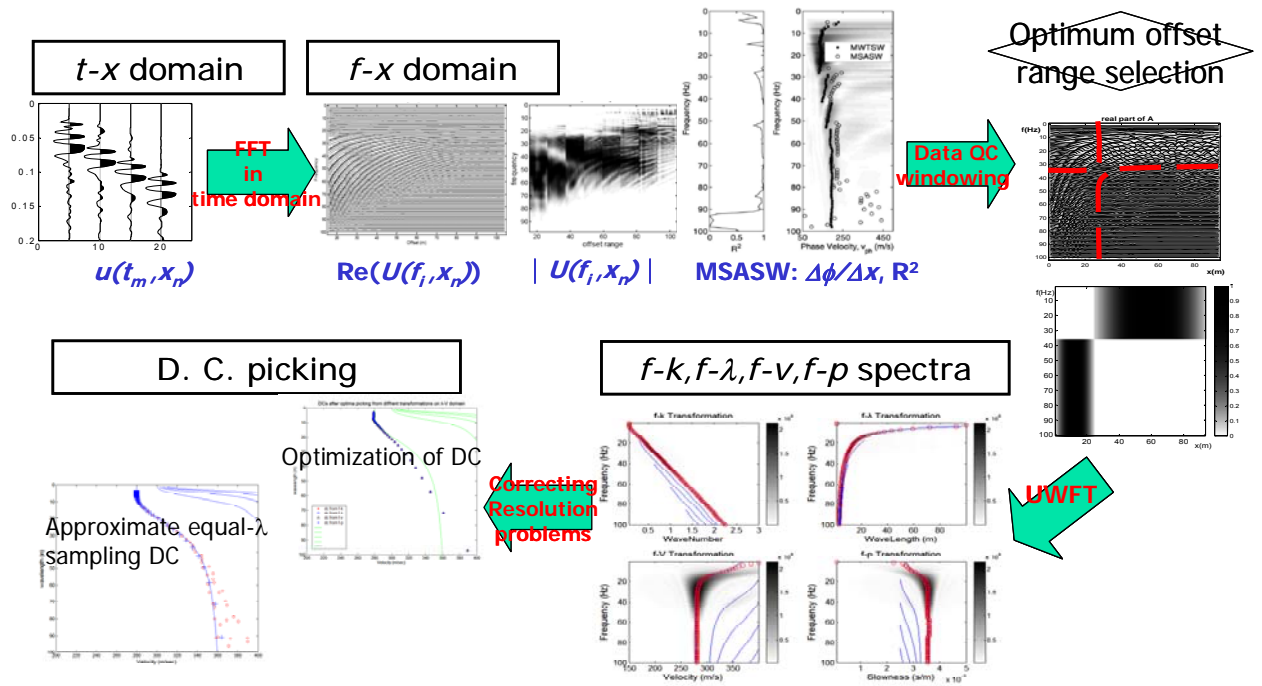


Fig. 4-25 The flow chart of the proposed standard dispersion analysis

After several practical tests and numerical simulations, a series of procedures for signal processing, as shown in Fig. 4-25, are proposed and summarized as follows:

1. The original  $t-x$  raw data (conventional MASW or pseudo-section records) is converted to the  $f-x$  complex data by the discrete Fourier Transform with respect to time.
2. The  $f-x$  complex data can reveal the signal quality from several aspects:
  - ✧ The signal quality in frequency domain can be first assessed by the estimation of  $\Delta\phi/\Delta x$  (MSASW). The data quality at each sampling in space domain can be evaluated by the R-square statistic ( $R^2$ ) of the regression analysis.
  - ✧ The signal quality in both frequency and offset domains can be observed in the real part and energy spectrum of the  $f-x$  complex data. For each frequency component, the offset range with the more periodic oscillation of the real part and the more intensive energy distribution of the amplitude spectrum

represents the better signal quality within the range.

3. Optimum offset range selection: By inspecting the wave propagation pattern in the  $f$ - $x$  domain, areas with low S/N ratio or near and far field effects can be identified and an appropriate 2-D window of reduction coefficients in the  $f$ - $x$  domain can be applied to screen out poor data. The amendatory data with better signal quality can proceed for further dispersion analysis.
4. Unified Wavefield Transformation (UWFT): Following the first DFT in the time domain, the unified procedure proceeds with another Fourier Transform with respect to the space on the complex  $f$ - $x$  data. By using change of variables, the UWFT algorithm can transform the wavefield into  $f$ - $k$ ,  $f$ - $p$ ,  $f$ - $v$  or  $f$ - $\lambda$  representations simultaneously.
5. Dispersion curve picking: By an optimization procedure, the dispersion curve for the inversion can be uniquely determined without the difference caused by discretization during wavefield transformation. Also the dispersion curve should be examined for deficient data sampling in  $\lambda$ - $v$  domain and then compensated by equal- $\lambda$  sampling.

## 5 Conclusion and suggestion

### 5.1 Conclusion

Despite its apparent advantage over the two-channel SASW (spectral analysis of surface wave) method, the testing configuration of the MASW (multi-station analysis of surface wave) method remains a crucial factor that may affect the test results. Tradeoffs are involved when selecting the testing parameters, In addition, several algorithms with different preference in the literature exist for the dispersion analysis. The objectives of this study are to establish a standard procedure for field testing and dispersion analysis of MASW.

In the part related to field testing, the influences of temporal and spatial parameters are investigated, which includes aliasing and leakage in both time and space domain, far and near field effects, higher mode domination, and horizontal resolution. The investigation leads to several rules for choosing testing parameters. An innovative testing procedure, called the pseudo-section method, and the associated signal processing is proposed to resolve the dilemma of choosing testing parameters and standardize the testing procedure. In addition, a complementary seismic source with greater energy and lower frequency contents and a non-invasive receiver stream are developed and evaluated in this study. Major conclusions drawn from this part of study include:

1. The field testing basically involves generating a surface wavefield and recording discretized wavefield. The discretization and truncation in the time and space domain result in aliasing and leakage in the spectral analysis. While modern seismograph possesses sufficient sampling rate and recording time, the sampling of the space data by geophones is relatively limited. The geophone interval and spread length respectively determines the shortest and longest wavelengths that can be analyzed.

2. The effects of multiple modes on multi-station measurements are investigated and the criterion of mode separability is discovered. The offset range (conventional geophone spread length) required to separate two modes is inversely proportional to the difference in wave number. A long geophone spread is required to have great depth coverage and separate potential higher modes, but is unfavorable for lateral resolution.
3. The near offset (nearest source-to-receiver distance) determines the offset range affected by near and far field effects. Mitigations of the near field and far field effects by choosing appropriate near offset are in conflict.
4. The dilemma in deciding the geophone spread and near offset can be resolved by the proposed pseudo-section method. It consists of a walk-away survey and a phase-seaming procedure when synthesizing seismograms with different nearest source-to-receiver offset, allowing wide-wavelength dispersion analysis within a small spatial range.
5. The standard field configuration is proposed. The geophone interval and near offset is determined by the shortest wavelength of interest and the actual geophone spread depends on interested spatial resolution. The number of walk-away shots should be enough for the longest wavelength of interest and separating possible higher modes. To improve testing efficiency, the source and receiver may be exchanged and a non-invasive receiver stream can be used. For long offset, a heavy weight-drop source can be used to enhance low frequency measurements.

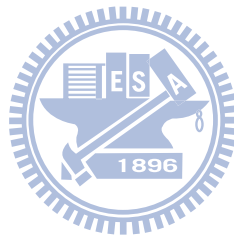
In the part of dispersion analysis, the procedures for signal quality assessment and a unified approach for wavefield transformation are proposed. Furthermore, the differences between conventional wavefield transformations and data sampling of dispersion curve are

discussed. The major conclusions are illustrated as follows:

1. The discrete wavefield in time-space ( $t-x$ ) domain is transformed to frequency-space ( $f-x$ ) domain first. The information revealed from the complex data in the  $f-x$  domain can be helpful on signal quality controls and preliminary understanding of results, which includes:
  - ✧ The energy spectrum provides indication of effective frequency range and the variation of phase angle with distance allows preliminary dispersion analysis (a new method called multi-channel spectral analysis of surface wave, MSASW).
  - ✧ In addition to the preliminary dispersion curve, MSASW can also evaluate the data quality because it is based on the linear regression of phase angles measured at multiple stations. The proper range of offset for constructing the dispersion curve can be selected, and existence of multiple modes may be identified.
  - ✧ The real part of  $f-x$  complex data is shown to be useful for optimum offset selection to reduce the effect of near and far field effects.
2. The  $f-x$  domain is further transformed to  $f-k$  (wavenumber),  $f-p$  (slowness),  $f-v$  (velocity), or  $f-\lambda$  (wavelength). The  $f-k$  transformation,  $f-p$  transformation, and phase shift methods were done with different algorithms and conclusion of their performance comparison varies in previous studies. In this study, a new unified algorithm is proposed that transforms the time-space wavefield into  $f-k$ ,  $f-p$ ,  $f-v$  and  $f-\lambda$  domains simultaneously.
3. The dispersion curves extracted from different domains may be different because the discretization in different domain implies different resolution in the dispersion analysis. Although the recorded time-space wavefield is discrete, the 2D wavefield transformation remain continuous in theory (i.e.  $f$ ,  $k$ ,  $p$ ,  $v$ , and  $\lambda$  are continuous

quantities). The dispersion curves obtained by different transformation are shown to be identical by a newly-proposed optimization method based on the discrete-space Fourier Transform, which allows the transformed domain remain continuous for best resolution of dispersion analysis.

4. This study further investigates the data sampling of the dispersion curve. The wave propagation theory shows the wavelength ( $\lambda$ ) has a close relation to the influence depth, nevertheless conventional wavefield transformations never directly deal with it. The conventional dispersion analysis samples equally in  $f$  domain and causes over sampling in short wavelengths (shallow depths). A wavelength-controlled sampling approach is proposed for the dispersion curve to avoid bias in depth sampling.



## 5.2 Suggestion

Although this study has already explicitly proposed criteria, procedures and algorithms for field testing and dispersion analysis, the standardization of MASW is yet to be well established. Several future studies remained to be carried out.

1. In the present study, the signal quality of raw data and uncertainty of the dispersion analysis is only qualitatively evaluated. A more precise quantitative analysis can be further conducted.
2. The optimal offset range selection is still a manual procedure that may lead to different results by different users. An automatic procedure will be helpful to improve efficiency and objectivity in the dispersion analysis.
3. The effective offset range is inherently restricted by the near and far field effect. The offset range may not always be long enough to separate different modes when multiple modes dominate. How to deal with multiple modes or effective mode in the inversion is another subject for further investigation.
4. It is well known that the surface wave is more sensitive to velocity profile at shallow depth. The advantage of wavelength-controlled dispersion analysis should be further investigated. For example, future studied may be carried out to see whether a thin layer at deeper depth can be detected.
5. This study assumes that the medium is horizontally layered. Investigations on the effects of lateral heterogeneity are also suggested for future studies.



## 6 Reference

Aki, K. and Richards, P. G., (2002), “Quantitative seismology, theory and method”, Vol. 2, San Francisco: Freeman

Achenbach, J. D., (1973), “Wave propagation in elastic solids”, North-Holland publishing company

Alleyne, D., and Cawley, P. (1990), “A two-dimensional Fourier Transform method for the propagating multimode signals”, Journal of the Acoustical Society of America, 89(3): 1159–1168.

Beaty, K., (2000), “Determination of near-surface variability using Rayleigh waves”, Master thesis, University of Alberta

Beaty, K., D. R. Schmitt and M. Sacchi, (2002), “Simulated annealing inversion of multimode Rayleigh waves dispersion curves for geological structure”, Geophys. J. Internat. 151, pp 622-631

Boore, D. M., (1972), “Finite difference methods for seismic wave propagation in heterogeneous materials”, Methods in computational physics, Ed. B. A. Bolt, pp. 1-37, Academic Press

Bellotti, R., Ghionna, V.N., Jamiolkowski, M., and Robertson, P.K., (1989), “Design Parameters of Cohesionless Soils from In-Situ Tests.”, Specialty Session on In-Situ Testing of Soil Properties for Transportation Facilities, Sponsored by Committee A2L02-Soil and Rock Properties, National Research Council, Transportation Research Board, Washington, January

Cuellar, V., (1997), “Geotechnical application of the spectral analysis of surface waves”, in Modern geophysics in engineering geology, Eds. D. M. McCann, M. Eddleston, P. J. Fenning, and G. M. Reeves, pp. 53-52, Geological Society Engineering Geology Special Publication no.12

Das, B. M., (1993), “Principles of soil dynamics”, PWS-KENT Publishing Company

Dobry, R., Borcherdt, R.D., Crouse, C.B., Idriss, I.M., Joyner, W.B., Martin, G.R., Power, M.S., Rinne, E.E., and Seed, R.B. (2000), “New site coefficients and site classification system used in recent building seismic code provisions”, *Earthquake Spectra* 16(1), 41–67.

Doyle H., (1995) “Seismology”, J. Wiley & sons, Chichester

Electric Power Research Institute. (1991), Proceedings: “NSF/EPRI Workshop on Dynamic Soil Properties and Site Characterization”, Report NP-7337, Vol. 1, Research Project 810-14.

Electric Power Research Institute. (1993). “Guidelines for Determining Design Basis Ground Motions” Vol. I: Methods and Guidelines for Estimating Earthquake Ground Motion in Eastern North America. EPRI TR-102293 Project 3302

Ewing, W. M., Jardetzky, W. S., and Press, F., (1957), “Elastic waves in layered media”, McGraw-Hill book company, Inc..

Forbriger, T., (2003), “Inversion of shallow-seismic wavefields: I. Wavefield transformation”, *Geophys. J. int.* (2003) 153, pp 719-734

Forbriger, T., (2003), “Inversion of shallow-seismic wavefields: II. Inferring subsurface properties from wavefield transforms”, *Geophys. J. int.* (2003) 153, pp 735-752

Forchap, E.A., and Schmid, G., (1998), “Experimental determination of Rayleigh-wave mode velocities using the method of wave number analysis”, *Soil Dynamics and Earthquake Engineering*, 17: 177–183.

Foti, S. and Fahey, M., (2003), “Applications of multistation surface wave testing”, *Proceedings of the 3rd International Symposium on Deformation Characteristics of Geomaterials*, Lyon, France; 2003. p. 13-19.

Foti, S., (2000), “Multistation method for geotechnical characterization using surface waves”, Ph. D. thesis, Politecnico di Torino

Futterman, W. I., (1962), “Dispersive body waves”, *J. Geophys. Res.* 67(1962), no. 13,

pp. 893-912

Ganji, V., Gucunski, N. and Nazarian, S., (1998) , “Automated inversion procedure for spectral analysis of surface waves”, J. Geotech. And Geoenv. Eng. 124(1998), no.8, pp757-769

Haskell, N. A., (1953), “the dispersion of surface waves on multilayered media”, Bull. Seism. Soc. Am. 43(1953), no. 1, pp 17-34

Hunaidi, O., (1998), “Evolution-based genetic algorithms for analysis of non-destructive surface wave tests on pavement”, NDTGE Int. 31(1998), no 4, pp. 273-280

Ishibashi, I. (1992). Discussion to “Effect of Soil Plasticity on Cyclic Response.”, by M. Vucetic and R. Dobry, Journal of Geotechnical Engineering, ASCE, Vol.118, No.5, pp.830-832.

Ishihara, K., (1996), “Soil Behaviour in Earthquake Geotechnics.”, Oxford Science Publications, Oxford, UK

Kausel, E. and Roesset, J. M., (1981), “Stiffness matrices for layered soils”, Bull. Seism. Soc. Am. 71(1981), no. 6, pp 1743-1761

Kennett, B. L. N., (1974), “Reflections, rays and reverberations”, Bull. Seism. Soc. Am. 64(1974), no. 6, pp 1685-1696

Kennett, B. L. N., (1983), “Seismic wave propagation in stratified media”, Cambridge university press

Kramer, S. L., (1996), “Geotechnical earthquake engineering”, Prentice Hall

Lai, C. G. and Rix, G. J., (1998), “Simultaneous inversion of Rayleigh phase velocity and attenuation for near-surface site characterization”, Report No. CIT-CEE/GEO-98-2, Georgia Institute of Technology

Lay, T., Wallace, T. C., (1995), “Modern global seismology”, Academic press

Lin, C. P., Chang, C. C., Chang, T. S., (2004), “The use of MASW method in the

assessment of soil liquefaction potential”, J. Soil Dynamics and Earthquake Engineering, Vol 24/9-10, pp 689-698.

Lin, C. P., Chang, T. S., (2004), “Multi-station Analysis of Surface Wave Dispersion”, J. Soil Dynamics and Earthquake Engineering, Vol 24/11, pp. 877-886.

Lin, C. P., Chang, T. S. and Cheng, M. H., (2003), “Shear-wave velocities from multi-station analysis of surface wave”, Proceedings of the 3rd International Symposium on Deformation Characteristics of Geomaterials, Lyon, France; 2003. p. 1335-1343.

Lin, C. P., Lin, C. H., (2007), “Effect of lateral heterogeneity on surface wave testing: Numerical simulations and a countermeasure”, J. Soil Dynamics and Earthquake Engineering, 27 (2007), pp. 541–552.

Lo Presti, D.C.F., (1987), “Behavior of Ticino Sand During Resonant Column Tests.”, Ph.D. Thesis, Politecnico di Torino, Torino, Italy

Lu, L. Y., and Zhang, B. X., (2004), “Analysis of dispersion curves of Rayleigh waves in the frequency–wavenumber domain”, Can. Geotech. J. 41: 583–598

Lysmer, J. and Drake, L. A., (1972), “A finite element method for seismology”, Methods in computational physics, Ed. B. A. Bolt, pp. 181-216, Academic Press

Mackenzie, G. D., Maguire, P. K. H., Denton, P., Morgan, J. and Warner, M., (2001), “Shallow seismic velocity structure of the Chicxulub impact crater from modeling of Rg dispersion using a genetic algorithm”, Tectonogeophysics, 338(2001), pp. 97-112

Malischewsky, P., (1987), “Surface waves and discontinuities”, Elsevier scientific publishing company

McMechan G.A., Yedlin M.J., (1981), “Analysis of dispersive waves by wave field transformation”, Geophysics, vol. 46, pp. 869-874

Meier, R. W. and Rix, G. J., (1993), “An initial study of surface wave inversion using artificial neural networks”, Geotechnical testing journal, 16(1993), no 4, pp. 425-431

O'Neill, A., "Full waveform reflectivity for inversion of surface wave dispersion in shallow site investigations", Proc. 2nd Int. Conf. on Site Char. (ISC-2), Portugal, Sep 2004

O'Neill, A., "Shear velocity model appraisal in shallow surface wave inversion", Proc. 2nd Int. Conf. on Site Char. (ISC-2), Portugal, Sep 2004

O'Neill, A., (2003), "Full-waveform reflectivity for modeling inversion and appraisal of seismic surface wave dispersion in shallow site investigation", Ph. D. thesis, University of Western Australia

Robinson, E. A., (1982), "Spectral approach to geophysical inversion by Lorentz, Fourier and Radon transforms", Processing IEEE (1982), vol. 70, pp. 1039-1054.

Park, C. B., Xia, J., and Miller, R. D., (1998a), Ground roll as a tool to image near-surface anomaly: 68th Ann. Internat. Mtg., Soc. Expl. Geophys., Expanded Abstracts, 874–877.

Park, C. B., Xia, J., and Miller, R. D., (1998b), Imaging dispersion curves of surface waves on multichannel record: 68th Ann. Internat. Mtg., Soc. Expl. Geophys., Expanded Abstracts, 1377–1380.

Park, C. B., Miller, R. D. and Xia, J., (1999), "Multichannel analysis of surface waves", Geophysics, vol. 64, no3 (1999), pp. 800-808

Park, C.B., Miller, R.D., and Miura, H., (2002), "Optimum field parameters of an MASW survey", [Exp.Abs.]: SEG-J, Tokyo, May 22-23, 2002.

Prokis J. G., Manolakies D. G., (1992), "Digital signal processing-principles, algorithms, and applications", 3<sup>rd</sup> ed. New Jersey, Prentice Hall

Richart, F. E. Jr., Woods, R. D. and Hall, J. R. Jr., (1970), "Vibration of soils and foundation", Prentice-Hall publishing company

Rix, G. J., (1988), "Experimental study of factors affecting the Spectral- Analysis- of- Surface- Waves method", Ph. D. thesis, University of Texas at Austin

Rix, G. J., Stokoe, K. H. II and Roesset, J. M., (1990), "Experimental determination of surface wave mode contribution", Soc., Expl. Geophys. 60th Ann. Internat. Mtg. (Soc., Expl. Geophys., 1990), pp 447-450

Sabetta, F. and Bommer, J. (2002), "Modification of the spectral shapes and subsoil conditions in Eurocode 8", 12th Europ. Conf. Earthq. Engin, paper ref. 518.

Sheriff, Gelfart, (1982), "Exploration seismology, Vol. 1, history, theory and acquisition", Cambridge university press

Stokoe, K. H. II, Wright, G. W., James, A. B. and Jose, M. R., (1994), "Characterization of geotechnical sites by SASW method", in Woods, R. D., Ed., Geophysical characterization of sites: Oxford Publ.

Strobbia, C., Foti, S., (2006), "Multi-offset phase analysis of surface wave data (MOPA)", J. of Applied Geophysics 59 (2006) 300–313

Takeuchi, H. and Saito, M., (1972), "Seismic surface waves", Methods in computational physics, Ed. B. A. Bolt, pp. 217-294, Academic Press

Thomson, W. T., (1950), "Transmission of elastic waves through a stratified solid medium", J. Appl. Phys. 21(1950), no. 2, 89-93

Tolstoy, I., (1978), "Wave propagation", McGraw-Hill book company, Inc.

Vucetic, M., and Dobry, R. (1991). "Effect of Soil Plasticity on Cyclic Response." J. Geotechnical Engineering, ASCE, 117(1), 89-107.

Vucetic, M. (1994). "Cyclic Threshold Shear Strains in Soils.", J. of Geotechnical Engineering, ASCE, Vol.120, No.12, pp.2208-2228.

Wang, C. Y., Herrmann, R. B., (1980), "A numerical study of P-, SV- and SH-wave generation in a plane layered medium", Bulletin of the seismologica society of America, vol. 70, 1980. p. 1015-36.

Wang, C.Y., (1981), "Wave theory for seismogram synthesis", Ph.D. Dissertation, Saint

Louis University

Watkins, D. J., Lysmer, J. and Monismith, C. L., (1974), "Nondestructive pavement evaluation by the wave propagation method", Report no. TE-74-2, University of Berkeley

Williams, T. P. and Gucunski, N., (1995), "Neural networks for backcalculation of moduli from SASW test", 9(1995), no. 1, pp 1-8.

Xia, J., Miller, R. D. and Park, C. B., (2003), "Inversion of higher mode frequency surface wave with fundamental and higher modes", J. Appl. Geophys. 52(2003), pp 45-57

Xia, J., Miller, R. D., Park, C. B., Hunter, J. A., Harris, J. B. and Ivanov, J., (2002), "Comparing shear-wave velocity profiles inverted from multichannel surface wave with borehole measurements". Soil Dynamics and Earthquake Engineering; 2002(22):181-190.

Xia, J., Miller, R. D. and Park, C. B., (2000), "Advantages of calculating shear wave velocity from surface wave with higher modes", Soc. Expl. Geophys. 69th Ann. Internat. Mtg. (Soc. Expl. Geophys, 2000), pp. 1295-1298

Xia, J., Miller, R. D. and Park, C. B., (1999), "Estimation of near surface shear wave velocity by inversion of Rayleigh wave", Geophysics, vol. 64, no3 (1999), pp. 691-700

Yamanaka, H. and Ishida, H., (1996), "Application of genetic algorithm to an inversion of surface wave dispersion data", Bull. Seism. Soc. Am., 86(1996), no. 2, pp. 436-444